Fall 2005

The effects of aging on cardiac mechanics

Samuel C. Lieber
New Jersey Institute of Technology

Recommended Citation

Lieber, Samuel C., "The effects of aging on cardiac mechanics" (2005). *Dissertations*. 750.
https://digitalcommons.njit.edu/dissertations/750

ABSTRACT

THE EFFECTS OF AGING ON CARDIAC MECHANICS

by
Samuel C. Lieber

It is well established that the aging heart exhibits left ventricular (LV) diastolic dysfunction and changes in mechanical properties, which have been attributed to alterations in the extracellular matrix (ECM). The investigators tested the hypothesis that the mechanical properties of cardiac myocytes significantly change with aging thereby contributing to the LV diastolic dysfunction. Cellular mechanical properties were determined by indenting cells with an atomic force microscope (AFM). The indentation results were interpreted by modeling the AFM probe as a blunted cone and determining an apparent elastic modulus (E) with classical infinitesimal strain theory (CIST). A commercially available finite element software package (ABAQUS) was used to further explore nano-indentation and the use of CIST to determine material properties. The cellular mechanical property changes, measured in young and old cardiac cells isolated from rats, showed a significant increase ($p<0.05$) in E with aging. Cellular protein changes were assessed by immunoblot (western) analyses in order to establish if material property changes also occurred with aging. The western results indicate significant ($p<0.05$) changes in cytoskeletal and mechanotransduction proteins with aging. These data support the concept that the mechanism mediating LV diastolic dysfunction in the aging hearts resides, in part, at the level of the myocyte. The effect of these aging induced cellular changes on global cardiac function will be further explored with instrumentation developed for implantation in an in vivo animal model.

THE EFFECTS OF AGING ON CARDIAC MECHANICS

by
Samuel C. Lieber

A Dissertation
Submitted to the Faculty of
New Jersey Institute of Technology
in Partial Fulfillment of the Requirements for the Degree of
Doctor of Philosophy in Mechanical Engineering

Department of Mechanical Engineering

January 2006

APPROVAL PAGE

THE EFFECTS OF AGING ON CARDIAC MECHANICS

Samuel C. Lieber

Dr. Nadine Aubry, Dissertation Advisor — Date
Distinguished Professor of Mechanical Engineering, NJIT

Dr. Stephen F. Vatner, Dissertation Advisor — Date
Professor and Chair of Cell Biology & Molecular Medicine, UMDNJ

Dr. Ernest S. Geskin, Committee Member — Date
Professor of Mechanical Engineering, NJIT

Dr. William C. Hunter, Committee Member — Date
Professor and Chair of Biomedical Engineering, NJIT

Dr. I. Joga Rao, Committee Member — Date
Associate Professor of Mechanical Engineering, NJIT

Dr. Pushpendra Singh, Committee Member — Date
Professor of Mechanical Engineering, NJIT

BIOGRAPHICAL SKETCH

Author: Samuel C. Lieber

Degree: Doctor of Philosophy

Date: January 2006

Undergraduate and Graduate Education:

- Doctor of Philosophy in Mechanical Engineering,
  New Jersey Institute of Technology, Newark, NJ, 2006

- Master of Science in Mechanical Engineering,
  New Jersey Institute of Technology, Newark, NJ, 2002

- Bachelor of Science in Mechanical Engineering,
  New Jersey Institute of Technology, Newark, NJ, 2001

Major: Mechanical Engineering

Selected Presentations:

S.C. Lieber,
"Validation of A Bench Durability Test for Bioprosthetic Heart Valves." 2001. Heart and Valve Mechanics Division of the ASME International Mechanical Engineering Congress and R&D Expo. New York, NY.

S.C. Lieber, N. Aubry, J. Pain, G. Diaz, S.J. Kim, & S.F. Vatner,
" Measurement Of The Transverse Apparent Elastic Modulus In Mammalian Cardiac Myocytes." 2003. Cellular Engineering and Mechanics Division of the ASME International Mechanical Engineering Congress and R&D Expo. Washington, D.C.

S.C. Lieber, , J. Pain, G. Diaz, S.J. Kim, & N. Aubry,
" Aging Increases Stiffness of Cardiac Myocytes Measured by Atomic Force Microscopy." 2003. American Heart Association International Conference.

S.C. Lieber,
" Cardiovascular Cell Morphology and Material Properties Measured by Atomic Force Microscopy." 2003. Seminar, Biomedical Engineering Department, New Jersey Institute of Technology.

I. Glasgow, S.C. Lieber, N. Aubry,

" Microfluidic Mixing Using Pulsing in Simple Geometry Channels." 2003. The American Physical Society 56th Annual Meeting of the Division of Fluid Dynamics.

Publications:

Lieber, S.C., N. Aubry, J. Pain, G. Diaz, S.J. Kim, and S.F. Vatner,

"Aging increases stiffness of cardiac myocytes measured by atomic force microscopy nanoindentation." Am J Physiol Heart Circ Physiol, 2004. 287(2): p. H645-51.

Glasgow, I., S. Lieber, and N. Aubry,

"Parameters influencing pulsed flow mixing in microchannels."
Anal Chem, 2004. 76(16): p. 4825-32.

Yan, L., H. Ge, H. Li, S.C. Lieber, F. Natividad, R.R. Resuello, S.J. Kim, S. Akeju, A. Sun, K. Loo, A.P. Peppas, F. Rossi, E.D. Lewandowski, A.P. Thomas, S.F. Vatner, and D.E. Vatner,

"Gender-specific proteomic alterations in glycolytic and mitochondrial pathways in aging monkey hearts." J Mol Cell Cardiol, 2004. 37(5): p. 921-9.

To the New Jersey Institute of Technology for giving me the opportunity to learn.

This thesis is dedicated to the memory of Isaac and Lea Lieber,
Samuele and Rosa Leo, and Niny Filomena.

ACKNOWLEDGMENT

I would like to thank my thesis advisor Dr. Nadine Aubry for her valuable input and support throughout this project. I would also like to express my gratitude to Dr. Stephen Vatner for his support and guidance during this collaboration between the New Jersey Institute of Technology (NJIT) and the University of Medicine and Dentistry of New Jersey (UMDNJ). I would like to thank Dr. Ernest Geskin, Dr. William C. Hunter, Dr. I. Joga Rao, and Dr. Pushpendra Singh for participating in my thesis committee and providing advisement throughout my thesis work. I would like to express my deepest appreciation to Gissela Diaz, Chull Hong, Brian Griffin, and Malthi Masurekar who made this project a success with their tireless efforts.

I would also like to acknowledge Dorothy Vatner, Jing Liu, Song-Jung Kim, Dr. Pi, Gui-Ping Yang, Lin Yan, Gautum Barot, Ian Glasgow, John Batton, George Barnes, Sharyn Serafin, Sue Klechinski, Diane Moore, Danil Grishchenko, and members of Dr. Vatner's and Dr. Aubry's labs. I would also like to thank the technical support provided by Veeco Metrology and Konigsberg Instruments.

I would like to thank my family for their patience, understanding, and support.

TABLE OF CONTENTS

TABLE OF CONTENTS
(Continued)

TABLE OF CONTENTS
(Continued)

TABLE OF CONTENTS
(Continued)

TABLE OF CONTENTS
(Continued)

LIST OF TABLES

LIST OF FIGURES

LIST OF FIGURES
(Continued)

LIST OF FIGURES
(Continued)

LIST OF FIGURES
(Continued)

CHAPTER 1

INTRODUCTION

1.1 Objective

The objective of this work is to analyze the effect of aging on single cardiac cell (myocyte) material properties and its relation to global cardiac function. The mechanical properties will be determined by indenting cells with an atomic force microscope (AFM) allowing force and indentation depth to be measured. The indentation results will be interpreted by modeling the AFM probe as a blunted cone and determining an apparent elastic modulus with classical infinitesimal strain theory (CIST). A commercially available finite element software package (ABAQUS) will be used to further explore nano-indentation and the use of CIST to determine material properties. The selected method will then be used to compare the Moduli of young and old cells isolated from rats. Cellular protein changes will be assessed by immunoblot (western) techniques in order to establish if a physical material property change has occurred with age. Instrumentation for implantation will be developed for an in vivo animal model in order to explore the effect of aging induced cellular changes on global cardiac function.

1.2 Anatomy of the Heart

The heart is divided into four muscular chambers, the left and right atria and left and right ventricles, which are arranged to form the left and right heart pump systems (Figure 1.1). The right heart pump system (right atria and ventricle) is part of the pulmonary vascular system which sends deoxygenated blood to the lungs to be oxygenated.

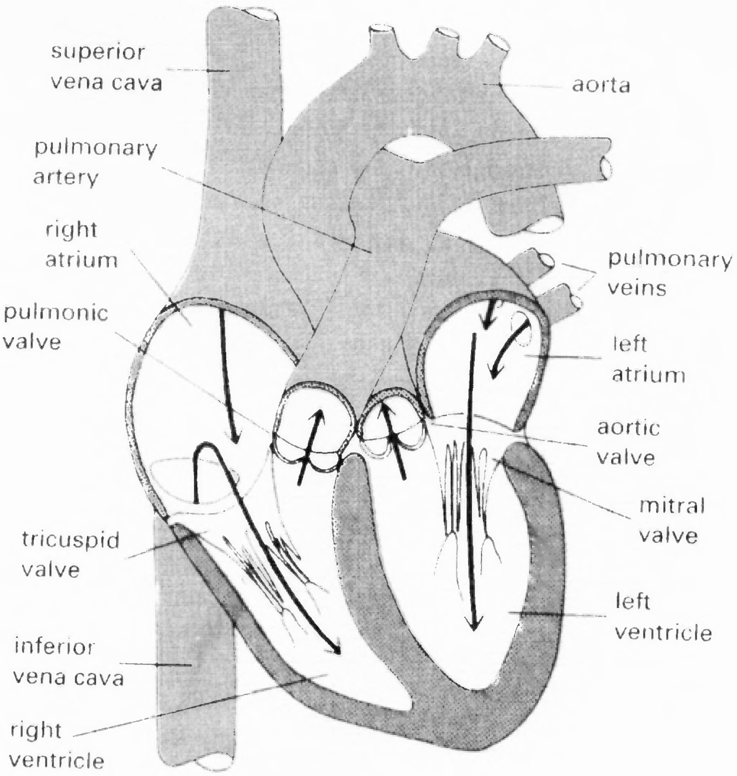

Figure 1.1 Diagram of the heart. Image modified from [1].

The left heart pumping system (left atria and ventricle) is part of the systemic vascular system which pumps blood throughout the rest of the body [1]. The flow of blood through the chambers of the heart is shown in Figure 1.1. Blood returns from the systemic system (organs, muscles, tissues, etc.) to the right atrium by the superior and inferior venae cavae (veins). Blood then passes the tricuspid valve into the right ventricle where it is pumped through the pulmonic valve into the pulmonary (associated with the lungs) circulation system through the pulmonary arteries. Blood is oxygenated at the lungs and flows to the left atrium through the pulmonary veins. Blood then passes through the mitral valve into the left ventricle where it is pumped through the aortic valve into the aorta (artery) to be sent throughout the rest of the body [1]. The right and left heart pumps are different physically but operate in the same fashion. The right ventricle pumps at a lower pressure then the left ventricle, which has roughly three times the mass and twice the thickness of the right ventricle [2]. The focus of this research is on the left heart pump, and its "pressure pump" the left ventricle.

1.3 Cardiac Muscle Anatomy and Function

The left ventricle is an axisymmetric ellipsoid constructed from billions of cardiac muscle cells (myocytes) connected end-to-end to form a network of muscle fibers (Figure 1.2) [2]. Cardiac myocytes occupy approximately 75% of normal myocardial tissue volume[3].

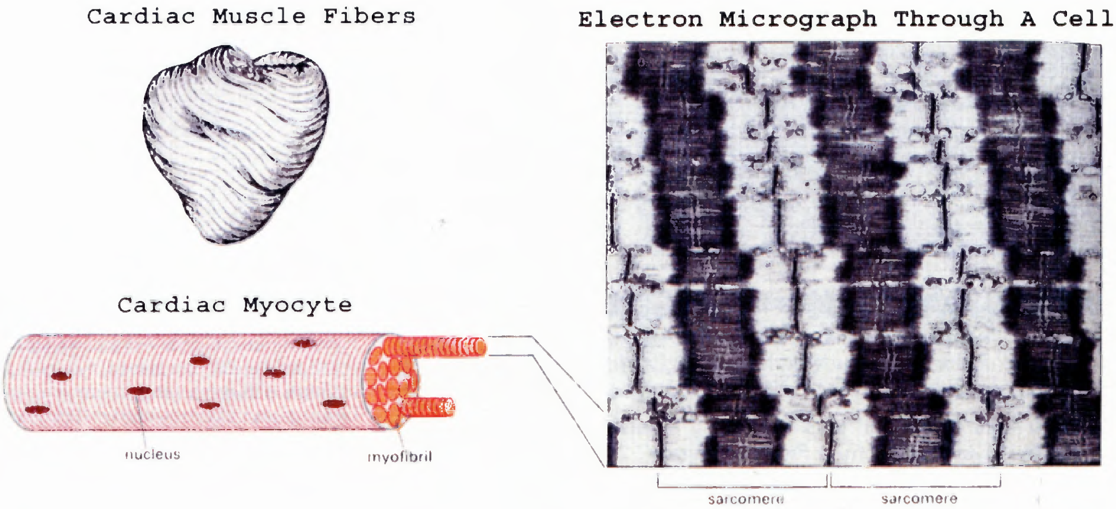

Figure 1.2 Cardiac muscle fibers consist of myocytes which consist of myofibrils. Image modified from [4, 5].

Myocytes are branched and connected to other myocytes in an end-to-end fashion throughout the myocardium via low-resistance folds known as intercalated disks. The purpose of these disks is to provide a mechanical and electrical connection between the cells so that the contractile force is felt and the action potentials can propagate along the length of the myocyte onto other connected myocytes. Myocytes are tubular structures

50-130 μm long with a diameter of 10-50 μm [5, 6]. The ability of the ventricles to generate pressure is derived from the ability of individual myocytes to shorten and generate a force [1]. Force production and shortening of cardiac muscle are created by regulated interactions between contractile proteins which are assembled in an ordered and repeating structure called the sarcomere (Figure 1.3).

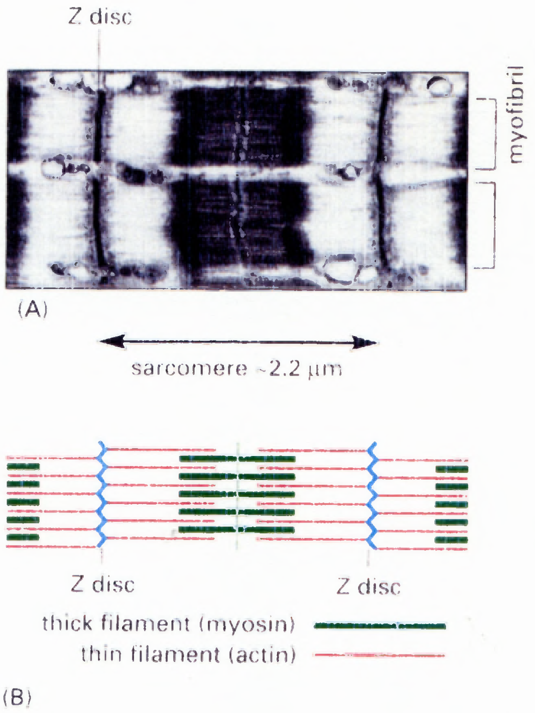

Figure 1.3 (A) Electron micrograph of a sarcomere and (B) schematic diagram showing protein structure [5].

Cardiac myocytes are electrically excitable cells and contract when they are stimulated by ionic electrical impulses (action potentials). The action potentials cause mechanical contraction through a process called excitation-contraction coupling, which occurs with a dramatic increase in the intracellular Ca^{2+} concentration (from resting 0.1 μM to maximum 100 μM) [1]. The cardiac cycle (one heart beat) is divided into the systolic (contraction) and diastolic (relaxation) phases. Systole occurs when the intracellular Ca^{2+} level is greater than 1.0 μM and the cross bridges between myosin and the actin filaments form [1, 2]. During systole, the muscles shorten and generate force along their long axis by the linking (cross bridges) between the myosin (thick filaments) and actin (thin filaments) assembled in a repeating 2.5 μm long structure (sarcomere) [5]. The actin filaments are attached in a band of structural proteins (Z disc) on the boundary of each sarcomere, and the myosin filaments are held in a strand of proteins centered between the Z-discs (M-line) [5]. Diastole (relaxation) is the period of time during which the muscle relaxes from the maximally contracted state back towards its resting state [2]. This is known as the sliding filament mechanism of contraction [1, 2].

1.4 Cardiac Myocyte Structure and Function

The outer surface of the cardiac myocyte, is comprised of a surface membrane called the sarcolemma, a lipid bilayer containing pumps and channels that control the influx and efflux of ions that produce action potentials [2]. The proteins which contribute to the cell shape, mechanical resistance, and morphological integrity of cardiac myocytes can be subdivided into several groups based on their structural and functional properties [7]. This work focuses on proteins in two major groups those which strongly contribute to mechanotransduction and those which are part of the cytoskeleton.

1.4.1 Mechanotransduction and Membrane Associated Proteins

The process of mechanotransduction refers to cellular mechanisms by which cells sense physical forces, transduce the forces into biochemical signals, and generate appropriate responses leading to alterations in cell structure and function [8]. How cells respond to variations in mechanical forces is critical to maintaining stable physiological functions (homeostasis) and in the development of many diseases [9]. Mechanotransduction in cardiac myocytes is particularly complex, in that individual muscle cells both respond to externally applied mechanical forces as well as generate internal loads that are transmitted to adjacent cells and their surrounding extracellular matrix (ECM) [8]. Understanding the cellular and molecular basis for mechanotransduction is important to our overall understanding of cardiac structure and function in the normal and diseased heart. Mechanotransduction can be further studied by investigating the common pathway for force transmission through groups of proteins. The main signaling section for the cytoskeleton is the focal adhesion complex: a multimolecular structure consisting of structural proteins, signaling molecules, and transmembrane receptors. Focal adhesions are dynamic structures that respond to mechanical stress with rapid reorganization and formation [10]. These proteins are all localized at or close to the cellular membrane and are functionally different from the extramyofilament cytoskeleton [11]. These proteins are involved in the fixation of sarcomeres to the sarcolemma and the stabilization of the T-tubular system [12]. They represent a component connecting the intracellular environment with the ECM [7, 11]. They, along with integrin, are involved in mechanotransduction where physical forces are converted into biochemical signals(Figure 1.4) [2].

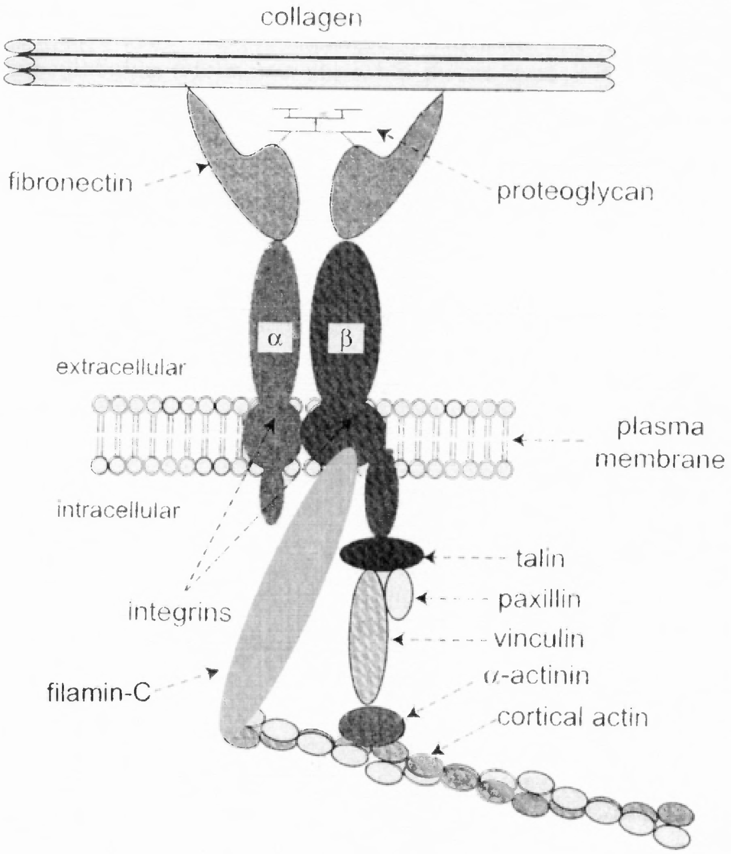

Figure 1.4 Sketch of membrane associated proteins which are involved in mechanotransduction in myocytes. Image modified from [2].

1.4.1.1 Integrins. Integrins (MW 130 kDa) are strain transducers and are the main receptors that connect the cytoskeleton to the ECM [13]. Integrins were initially considered solely as molecules necessary for adhesive interactions between cells and the ECM, but they have also been recognized as having an intimate relationship with force. [14]. Recently, integrins have also been identified as mechanotransduction molecules in cardiac cells converting mechanical signals to biochemical ones [15, 16].

1.4.1.2 Vinculin. Vinculin (*MW*116 kDa) links the cell membrane and actin filaments via talin, paxillin and α-actinin. Some have reported that Vinculin is located at the Z-disc [17]. However, others have shown through confocal microscopy studies that vinculin is part of the T-tubular membrane, which gives the impression of being localized in the Z-disc [12]. A tail domain of vinculin (MW 116 kDa) binds to actin [18], whereas the head binds to talin. Vinculin is in close contact with integrins and serves as an anchor for actin and actin-binding proteins (e.g. α actinin). Vinculin contributes to the stability of the cell membrane and is involved in communication, through integrins, between the intracellular and extracellular proteins. In cardiac myocytes, vinculin is localized in the fascia adherens part of the intercalated disk and at the costameres of the lateral sarcolemma [11].

1.4.1.3 Talin. Talin (MW 215 kDA) is important in cell substratum adhesion. Talin forms a high affinity bond with vinculin and binds to β-integrin, but not to actin. Talin is another major component of focal cell contacts and is found not only in striated muscle but also in smooth muscle cells, endothelia, and some hemopoetic precursor cells. Its major role is in establishing an attachment between the myofibrils and membranes. In cardiac myocytes, talin shows a labeling pattern similar to that of vinculin, but it is absent in the intercalated disc [11].

1.4.1.4 α-actinin. α-Actinin (MW 100 kDA) cross-links the actin filaments at the level of the Z-disc and keeps them in a fixed position. This allows interaction with the myosin cross bridges to be possible and increases the stability of the sarcomere. α-actinin is also an important link between actin and the cell membrane. It establishes communication between the intracellular environment and the ECM through cross-links with vinculin, talin, integrins, and fibronectin. α-actinin is also important in creating new myofibers [19].

1.4.1.5 **Filamin.** Filamin is a structural protein that belongs to an extended family of actin-binding proteins. Filamin-A and -B are ubiquitous, whereas filamin-C (MW ~280 kDA) is a muscle-restricted isoform [20]. The main known function of filamin is to cross-link actin filaments. This is achieved by the binding of the filamin dimer to two actin filaments through its N-terminal actin-binding domain, leading to the formation of a hinge between the two filaments. Filamin-C also binds to some transmembrane proteins such as β1 integrin [21].

1.4.2 Cytoskeletal Proteins

1.4.2.1 **Microtubules.** The tubulin molecule is a heterodimer of an α- and β-isoform with a molecular weight of 55 kDa per monomer and a diameter of 25 μm [7]. A constant turnover of microtubules by polymerization and depolymerization takes place. In cardiac myocytes, only 30% of total tubulin is present in the polymerized form as microtubules whereas 70% occurs as a non-polymerized cytosolic protein [22]. Microtubular associated proteins (MAPs) bind to α- and β-tubulin and play a significant role in stabilizing microtubules and enabling an interaction with other cellular organelles [7].

The main role of the microtubular network is to act as a railway that allows for the transport of particles between intracellular sites, which synthesize proteins and lipid particles and target organelles in construction [23, 24]. The microtubules constitute a dynamic network in the cytoskeleton that forms by polymerization and disassembles rapidly by depolymerization [25]. This process allows for rapid modifications of the extent and shape of the microtubular network, even without changes of the pool of available tubulin in the cell. One would expect that the microtubular network would be expressed in increased amounts as long as the myocyte receives a stimulus to grow and would disappear when the stimulus disappears [26].

1.4.2.2 **Desmin.** Desmin (*MW* 53 kDa) belongs to the family of intermediate filaments with a diameter of 12–15 nm, which ranges in size between microtubules (25 nm) and actin filaments (8–10 nm) [7]. This protein is found mainly in the Z-disk of striated muscles and in the dense bodies of smooth muscle cells (SMC) [27]. It plays an essential role in maintaining muscle cytoskelatal architecture by forming a three-dimensional scaffold around the myofibrillar Z-disk, and by connecting the entire contractile apparatus to the subsarcolemmal cytoskeleton, the nuclei, and other organelles [28, 29]. Desmin also forms longitudinal connections between the peripheries of successive Z-disks and along the plasma membranes of striated muscle cells [27]. Desmin is particularly abundant in the intercalated disks, which is the attachment point between cardiac myocytes in cardiac muscle. Studies indicate that desmin is essential for maintaining the structural integrity and function of muscles, and may be important for the positioning of mitochondria. Moreover, it is involved in the generation of active and passive forces through support of the sarcomere, is implicated in tissue repair, and is important in cell matrix interactions [27].

1.5 Contributions of Cellular Structure to Mechanics

The mechanical properties of tissue cells may contribute to the overall deformation of the tissue under applied forces. The field of cell mechanics addresses this topic together with how cells move, deform, interact, as well as how they sense, generate, and respond to mechanical forces. Recent developments in cell mechanics have included studies of cytoskeleton dynamics and cell ECM interactions. Cell mechanics examines the mechanical properties of not only whole cells; but also the subcellular structures (e.g. microtubules, actin filaments, and intermediate filaments) [30].

The shape and mechanical properties of tissue cells likely depends on the cytoskeleton. The internal cytoskeleton is composed of an interconnected network of actin filaments (6–10 nm in diameter), intermediate filaments (7–11 nm) and microtubules (25 nm) [31]. The three filamentous systems of the cytoskeleton are believed to be the major stress-bearing components in the cell, but also could be the structures that provide the mechanical interconnections from the membrane to the nucleus [30]. The mechanical properties of the cytoskeleton are a determinant factor in cell shape, and cellular functions including spreading, crawling, polarity, and cytokinesis [32-36]. The microtubule assembly participates in diverse processes, such as cell morphology, cellular motility, intracellular organization and transport [37]. Microtubules can also function as rigid struts opposing the force generated by the actin/myosin interaction [37, 38] and could contribute to the cytoskeleton's stiffness [39, 40].

1.6 Cardiac Pump Mechanics

The cardiovascular system (cardio refers to the heart, vascular to the vessels) consists of a central pump, the heart, and a network of tubes (blood vessels). This system transports blood which nourishes cells, removes cellular waste, and helps to protect against infection [41]. When the heart contracts (systole), blood is pumped into the large arteries (aorta) and the carotid arteries which then expand. As blood flows out of these arteries into smaller ones throughout the body the large blood vessels (aorta and carotid arteries) then recoil back to the size they had prior to the heart contraction. As the arteries relax, the heart also relaxes and fills with blood in preparation for the heart expansion (diastole) [42]. The mechanical function of the heart can be described by the pressure and volume changes that occur during one cardiac cycle (Figure 1.4) where left ventricular volume (LVV), left ventricular pressure (LVP), left atrial pressure (LAP) and aortic pressure (AOP) are plotted as a function of time. Before time **A** LVP and LVV are relatively constant and AOP is gradually declining. At time **A** there is electrical activation of the heart, contraction begins, and pressure rises inside the chamber. Early after contraction begins, LVP rises to be greater than the left atrial pressure and the mitral valve closes. Since LVP is less than AOP, the aortic valve is closed as well. Since both valves are closed, no blood can enter or leave the ventricle during this period called isovolumic contraction. At time **B** LVP is greater than AOP and the aortic valve opens, during which time there is very little difference between LVP and AOP, provided that AOP is measured just on the distal side of the aortic valve. During this time (ejection phase), blood is ejected from the ventricle into the aorta and LV volume decreases.

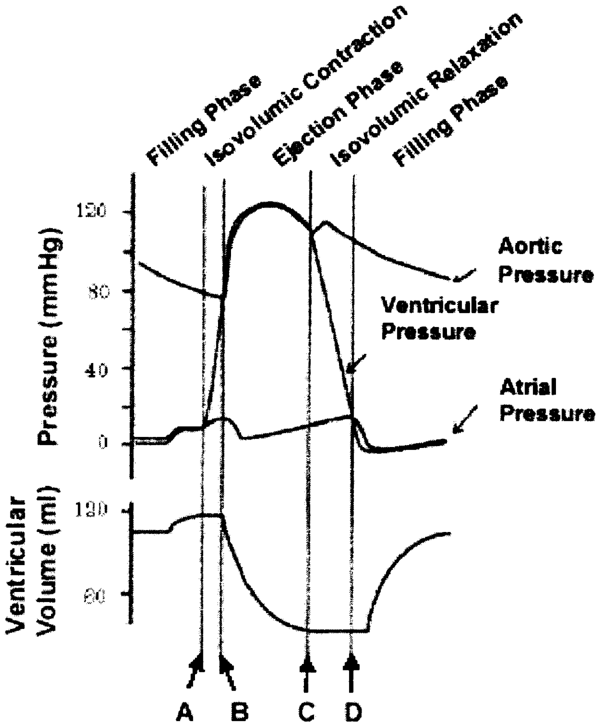

Figure 1.5 Left Ventricular Volume (LVV), Left Ventricular Pressure (LVP), Left Atrial Pressure (LAP) and Aortic Pressure (AOP) are plotted as a function of time. Image modified from [2].

As the contraction process of the cardiac muscle reaches its maximal effort, ejection slows down and ultimately, as the muscles begin to relax, LVP falls below AOP at time point C where the aortic valve closes. At this point ejection has ended and the ventricle is at its lowest volume. The relaxation process continues as indicated by the continued decline of LVP, but LVV is constant at its low level. This is because, once again, both mitral and aortic valves are closed; this phase is called isovolumic relaxation. At time D the LVP falls below the pressure existing in the left atrium and the mitral valve opens. At this point, blood flows from the left atrium into the LV as indicated by the rise of LVV with an increase in LVP as filling proceeds (filling phase) [1, 43]. The LVs pressure and volume is linked to the tension and length of the cardiac myocytes forming the muscle in its walls, where the cardiac muscle length-tension relationship is the basis for ventricular function [1]. The resting tension (preload) of the cardiac muscle fibers is set by the End Diastolic Pressure (EDP). The tension that must be developed by cardiac muscle fibers before they can shorten is referred to as afterload, which is the systemic arterial pressure [2].

The phases of the cardiac cycle can be demonstrated by displaying LVP as a function of LVV on a pressure-volume diagram (Figure 1.6), accomplished by plotting the simultaneously measured LVV and LVP on appropriately scaled axes, which corresponds to a cardiac muscle length tension relationship. In general terms, systole includes isovolumic contraction and ejection; diastole includes isovolumic relaxation and filling.

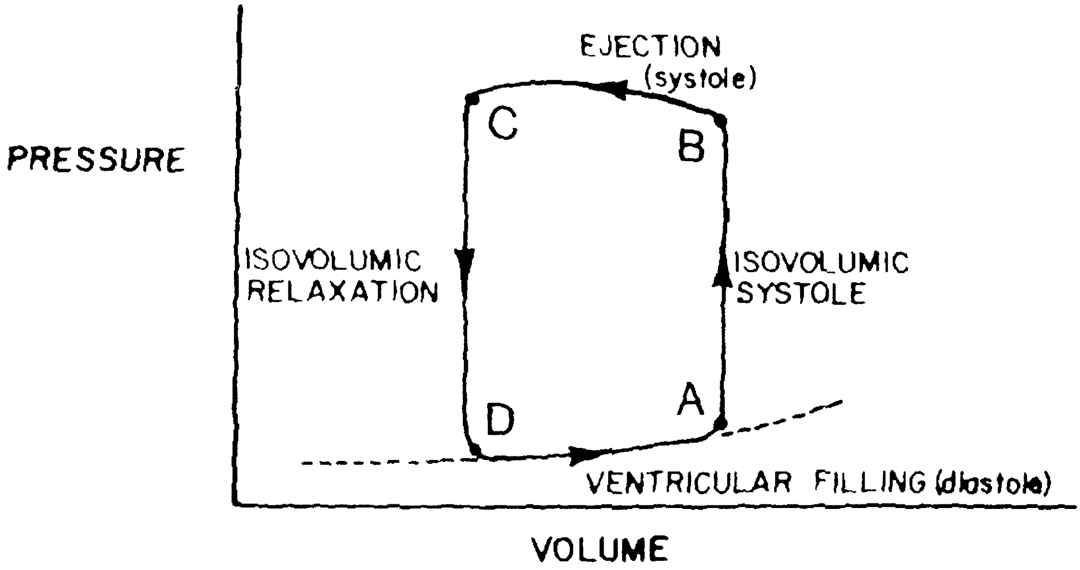

Figure 1.6 Pressure Volume (PV) Loop created by plotting LVP against LVV. Image modified from [44].

As shown in Figure 1.6, the plot of pressure versus volume (PV loop) for one cardiac cycle forms a clockwise loop. The point of maximal volume and minimal pressure corresponds to time A on Figure 1.5 which is the beginning of systole. During the first part of the cycle, pressure rises but volume stays the same (isovolumic contraction). Ultimately LVP rises above AOP, the aortic valve opens (B), ejection begins and volume starts to decrease. After the ventricle reaches its maximum activated state (C), LVP falls below AOP, the aortic valve closes and isovolumic relaxation commences. Finally, filling begins with the mitral valve opening (D). Analysis of a PV loop alone can provide several indices of the LV mechanical function; however, the major strength in this technique is the analysis during interaction. This interaction is achieved by varying the pressure conditions through occlusions in the circulatory system preventing LV filling (change in preload volume) or restricting LV emptying (change in afterload resistance) (Figure 1.7) [1, 43].

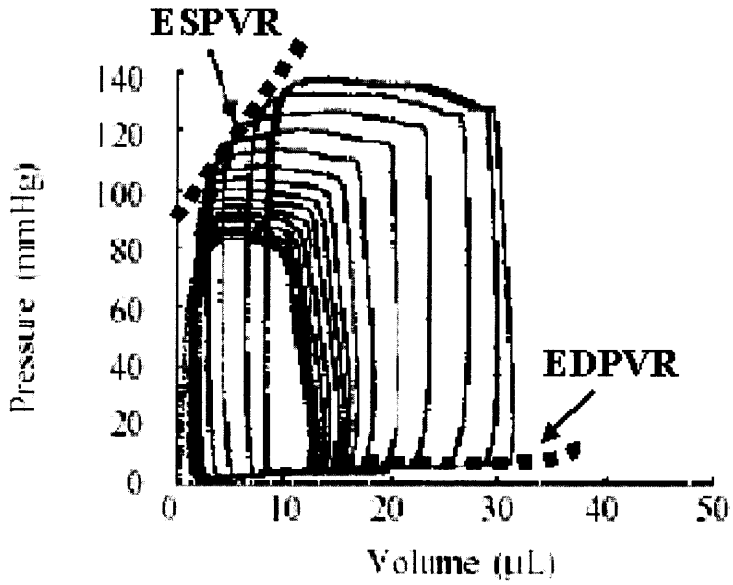

Figure 1.7 Pressure-Volume Loop with intervention (preload) allowing ESPVR and EDPVR to be determined.

Plotting of the End Systolic Pressure Volume points and End Diastolic Pressure Volume points during these interactions allows the development of indices of systolic elastance (End Systolic Pressure Volume Relationship (ESPVR)) and (End Diastolic Pressure Volume Relationship (EDPVR)). The regulation of the cardiac function depends on communications with the heart, the rest of the body, and the external environment.

These communications are made possible by signaling pathways which target receptors, that recognize and interpret the arrival of these small molecules on the cell surface. The most important regulators of the cardiac function are opposing stimuli carried by the sympathetic and parasympathetic nervous systems. Sympathetic stimulation increases heart rate, blood pressure, and myocardial contractility whereas, parasympathetic stimulation slows the heart, decreases blood pressure, and causes a negative effect on the force of muscle contraction [2].

1.7 The Effects of Cardiac Aging

Aging is marked by a decline in LV diastolic function in the absence of cardiovascular disease [45]. A significant number of patients who exhibit symptoms of congestive heart failure have preserved systolic function, but have significantly elevated LV filling pressures (diastolic heart failure). Diastolic heart failure is associated with various conditions including: aging [46]. This finding indicates that aging changes may predispose older individuals to diastolic heart failure. These changes include: increased hypertrophy and stiffness of the left ventricle, increased vascular stiffness, and decreased cardiovascular reserve [47]. Progress in understanding diastolic heart failure has been hindered by several factors: a lack of a reliable test to quantify the diastolic function, a poor understanding of the physiology of heart failure, and a lack of a standard definition of the medical condition [47]. Scientists believe that the mechanism of diastolic heart failure can be elucidated by the integration of information acquired from basic science investigations conducted in vitro and in vivo, mathematic modeling, and clinical investigations that can characterize the incidence, prevalence, and natural history of diastolic disease [46].

1.8 Rat Cardiac Aging

Aging is marked by a decline in left ventricular (LV) diastolic function in the absence of cardiovascular disease [45]. This age-related alteration in diastolic function has been linked to structural changes [48], where stiffness has been measured in the whole heart, excised papillary muscles, or cardiac muscle fibers [49, 50]. However, despite the agreement that there is an increase in collagen content in the aging heart, results of ventricular stiffness have been controversial indicating an increase [51], no change [52, 53], and even a decrease [54] with age in a number of animal species. The inconsistencies in stiffness results led us to investigate what is occurring at the level of the single LV myocyte.

The rat has been a widely accepted and used model for cardiac aging, where a 50% colony mortality is an indication of senescence [50]. In most strains of rats the senescent heart exhibits moderate LV hypertrophy (25%) compared to hearts from young and middle aged animals [50].In contrast to humans the senescent rat's LV wall thickness does not increase, but the LV cavity dilates [55], which can occur in the absence of high blood pressure (arterial hypertension) [56]. The ECM has been attributed with the majority aging induced cardiac dysfunction where the average LV collagen content doubles between adulthood and senescence [57] and LV fibronectin is markedly increased in senescent compared to adult rats [58]. The increased expression of fibronectin in the senescent heart has been linked to the overall increase in the proportion of the ECM [59]. Despite the increase in collagen content with fibrosis, there is no major uniform change in passive myocardial stiffness [49]. The changes observed in rat physiology with aging has been controversial as described in Table 1.1 where systolic parameters including Left Ventricular Systolic Pressure (LVSP), rate of pressure generation (+dP/dt), and elastance (Emax) and diastolic parameters Left Ventricular End Diastolic Pressure (LVEDP), rate of pressure generation (-dP/dt), and isovolumic relaxation time (τ), and the End Diastolic Pressure Volume Relationship (EDPVR) were measured in different strains and at different ages.

Table 1.1 Effect of Aging on Rat Physiology

Paper	Aging Effect	Species/Strain
Schmidt [60]	1) LVSP no change 2) +dP/dt no change 3) LVEDP increased 4) -dP/dt decreased 5) τ increased 6) Emax no change.	Male F344 rats aged 6, 26 mo
Zieman [61]	1) LVSP & LVEDP no change 2) τ increased	Male Wistar rats aged 4-7, 22-25 mo
Wanagat [62]	1) LVSP & LVEDP decreased 2) +dP/dt & -dP/dt decreased	Male F344xBN rats at 5 and 36-38 mo
Pacher [63]	1) LVSP & LVEDP increased 2) +dP/dt & -dP/dt decreased 3) Emax increased 4) τ increased 5) EDPVR slope increased	Male F344 rats aged 4-5-moand 24-26-mo
Brenner [53]	1) LV relaxation decreased. 2) Fractional shortening decreased. 3) LV stiffness was not affected by age.	Male F344xBN rats at 6 and 24 mo

Most of the increase in cardiac mass with aging, however, is due to myocardial cell enlargement (as is the case in humans). In individual myocytes isolated from rats of 2, 6–9, and 24–26 months of age, the average myocyte length increases by 20% between 2 and 24–26-months of age, while the average slack sarcomere length does not change although the average volume of individual cells approximately doubles over this age range [6]. There is also evidence to indicate that the number of myocytes within the heart decreases with aging, due to both necrosis (provoked cell death) and apoptosis (cell suicide), with the former predominating [59, 64, 65]. The effects of aging on single myocyte kinetics has also been documented, specifically it has been shown that the kinetics of the cellular reactions, which underlie the heart beat, are reduced in the senescent vs. the younger adult.

In rodent cardiac muscle, the action potential, the transient increase in cytosolic Ca^{2+}, and contraction are all prolonged with aging (as reviewed by [50]). The altered profile of excitation contraction mechanisms with aging results in a contraction that exhibits a reduced velocity and a prolonged time course. This has been reasoned to be energy efficient, where a prolonged contraction allows ejection of blood for a longer period of time[45, 50, 66]. The changes in myocyte contraction has been attributed to many factors including a change in the sarcomere's myosin heavy chain (MHCs) material property from a faster to a slower form [50]. Isolated myocytes and myocardium preparations have also shown β_1 and β_2 adrenergic receptor (AR) impairment with aging, where a reduced myocardial contractile response is seen to either β_1AR or β_2AR stimulation [67]. Further changes in the rat myocardium have been summarized by Lakatta in Table 1.2 [66]

Table 1.2 Myocardial Changes with Adult Aging in Rodents [66]

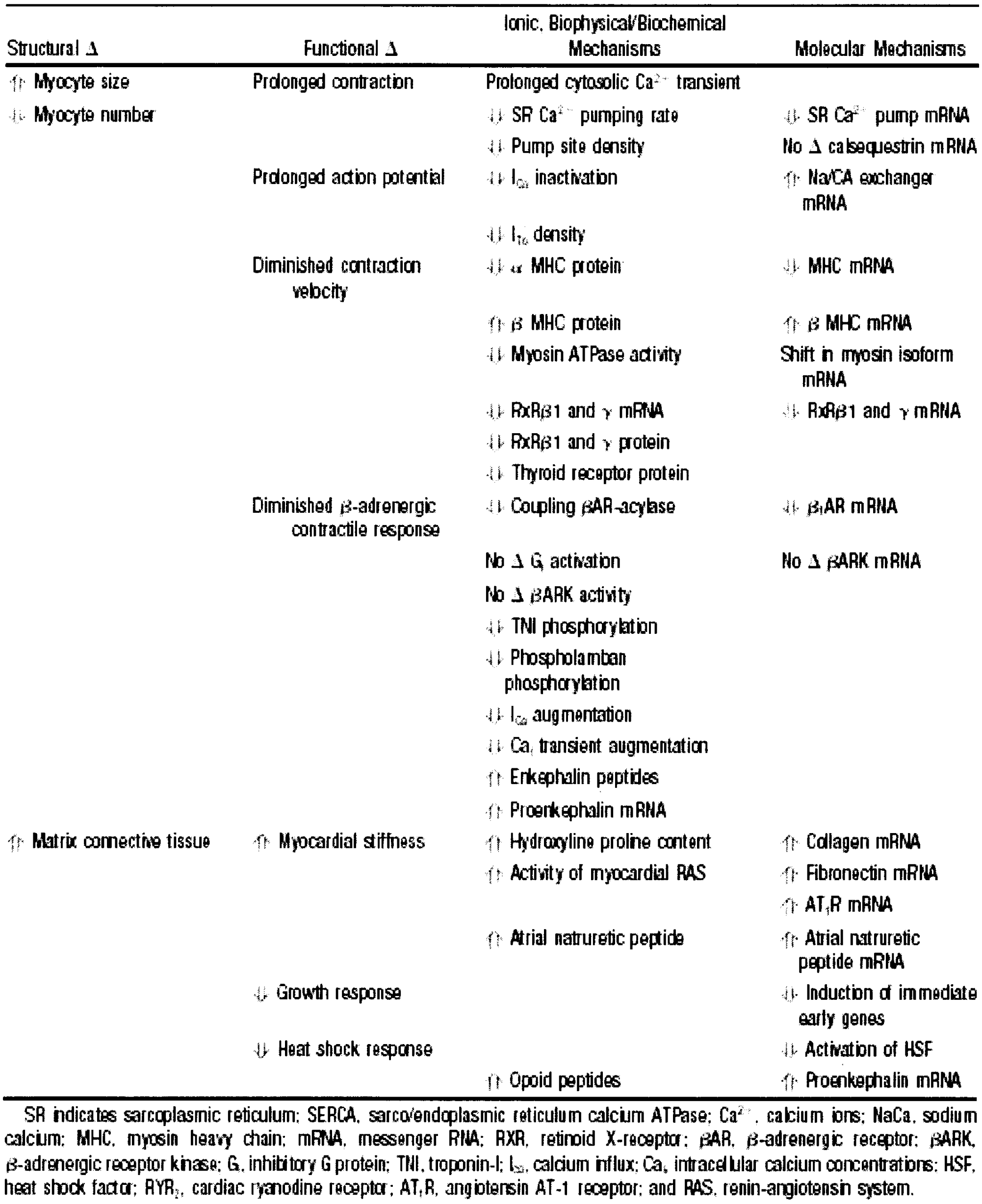

Structural Δ	Functional Δ	Ionic, Biophysical/Biochemical Mechanisms	Molecular Mechanisms
⇑ Myocyte size	Prolonged contraction	Prolonged cytosolic Ca^{2+} transient	
⇓ Myocyte number		⇓ SR Ca^{2+} pumping rate	⇓ SR Ca^{2+} pump mRNA
		⇓ Pump site density	No Δ calsequestrin mRNA
	Prolonged action potential	⇓ I_{Ca} inactivation	⇑ Na/CA exchanger mRNA
		⇓ I_{TO} density	
	Diminished contraction velocity	⇓ α MHC protein	⇓ MHC mRNA
		⇑ β MHC protein	⇑ β MHC mRNA
		⇓ Myosin ATPase activity	Shift in myosin isoform mRNA
		⇓ RxRβ1 and γ mRNA	⇓ RxRβ1 and γ mRNA
		⇓ RxRβ1 and γ protein	
		⇓ Thyroid receptor protein	
	Diminished β-adrenergic contractile response	⇓ Coupling βAR-acylase	⇓ $β_1$AR mRNA
		No Δ G_i activation	No Δ βARK mRNA
		No Δ βARK activity	
		⇓ TNI phosphorylation	
		⇓ Phospholamban phosphorylation	
		⇓ I_{Ca} augmentation	
		⇓ Ca_i transient augmentation	
		⇑ Enkephalin peptides	
		⇑ Proenkephalin mRNA	
⇑ Matrix connective tissue	⇑ Myocardial stiffness	⇑ Hydroxyline proline content	⇑ Collagen mRNA
		⇑ Activity of myocardial RAS	⇑ Fibronectin mRNA
			⇑ AT_1R mRNA
		⇑ Atrial natruretic peptide	⇑ Atrial natruretic peptide mRNA
	⇓ Growth response		⇓ Induction of immediate early genes
	⇓ Heat shock response		⇓ Activation of HSF
		⇑ Opoid peptides	⇑ Proenkephalin mRNA

SR indicates sarcoplasmic reticulum; SERCA, sarco/endoplasmic reticulum calcium ATPase; Ca^{2+}, calcium ions; NaCa, sodium calcium; MHC, myosin heavy chain; mRNA, messenger RNA; RXR, retinoid X-receptor; βAR, β-adrenergic receptor; βARK, β-adrenergic receptor kinase; G_i, inhibitory G protein; TNI, troponin-I; I_{Ca}, calcium influx; Ca_i, intracellular calcium concentrations; HSF, heat shock factor; RYR_2, cardiac ryanodine receptor; AT_1R, angiotensin AT-1 receptor; and RAS, renin-angiotensin system.

1.9 Atomic Force Microscopy (AFM)

1.9.1 AFM Development and Principle of Operation

The AFM, originally developed by Binnig, Quate, and Gerber [68], can image the three dimensional surface structure of biological specimens. The AFM has been used to image living cells, the cell's underlying cytoskeleton, chromatin and plasmids, ion channels, and a variety of membranes [69-73]. Dynamic processes such as crystal growth, mechanical pulses of cardiac cells, analysis of the mitotic cycle of living vertebrate cells, the polymerization of fibrinogen, and physicochemical properties such as elasticity and viscosity in living cells have been studied with the AFM [74-76].

The AFM tip, attached to a cantilevered spring, moves over the surface of the specimen and is deflected by the interaction forces between the tip atoms and the specimen atoms. Because the spring constant of the commonly used cantilevers (10^{-1} to 10^{-2} N/m) is much smaller than the intermolecular vibration spring constant of the atoms in the specimen (10 N/m), the cantilever can sense small forces exerted by the individual sample atoms [74]. The deflection of the tip is a measure of the forces sensed by the cantilever and the sensed forces are transduced to develop molecular images. The sample is raster scanned in the xy-plane beneath the tip. The vertical position of the sample (z) is also monitored. These movements are controlled by a piezoelectric xyz scanner; which uses the three coordinates to create an image [77].

1.9.2 AFM Cellular Imaging and Resolution

The AFM can image cellular and subcellular structures under physiological conditions with a resolution exceeding that of optical microscopes. Fixed erythrocytes dried onto glass cover slips were some of the first cells to be imaged by the AFM [69]; however, little information was obtained about the extracellular or intracellular structures. Living adult atrial cells were imaged at a resolution of ~20 nm [78]. At this increased resolution the cytoskeletal elements including muscle sarcomeres and cross bridges were able to be visualized [74]. Many cells have been imaged in aqueous conditions and many have been imaged alive [70, 71, 79-84].

The resolution obtained with the AFM may be cell dependent as well as hardware dependent. The limit of the AFM spatial resolution is not well defined. The images are formed by reconstructing the contour of forces exerted between the specimen and tip. By selecting a small scan size and appropriate operating conditions, one can often distinguish two adjacent objects that are < 1nm apart [85]. The lateral resolution in AFM is limited by the elastic indentation [86-90]. Biological materials, such as cells, often show a lower lateral resolution which can be explained by their deformation due to the AFM tip [87]. When the tip indents a soft surface, a certain contact area between the tip and the sample is created. This contact radius can be taken as a measure of the lateral resolution if one ignores the surface roughness [86]. From elastic experiments, Radmacher et al. [90] calculated a diameter between 500 and 50 nm for this contact area which is in good agreement with the lateral resolution usually obtained on cells. Forces in the pN range (1-10 pN) are required to obtain high-resolution images on biological materials with about 1 nm vertical deformation and only a few nm^2 area of contact [87, 88, 91]. The lateral resolution achieved depends on the characteristics of the tip, the operating environment, and the nature of the specimen [74].

For biological specimens in a normal imaging situation (e.g., the imaging of a living cell surface), the resolution is relatively poor (~10 nm) but higher than light microscopes and comparable to that of scanning electron microscopes. In the case of soft materials, such as cells, the achievable resolution will be limited by the elastic indentation of the sample by the tip. The resolution obtainable thus depends on the softness of the sample, the geometrical shape of the cantilever, and the loading force applied by the AFM tip [90]. The factor limiting resolution on the cell surface is the mobility of the upper membrane with respect to the lower membrane, which is anchored to the substrate, and also the mobility of the macromolecules within the membrane [74]. Improvements in resolution may be made first by increasing the surface rigidity by using suction of cells onto patch pipettes and thus reducing the lateral mobility; and second by imaging with low forces (attractive force mode imaging) [80].

Whole cell to molecule experiments in a physiological environment can be performed and dynamic changes in the molecular structure of channels, receptors, and other macromolecules can be observed [92]. AFM can be an important tool for growth and developmental studies of cells and processes such as nerve growth, synapse formation, and cell surface and cytoskeletal reorganizations [93]. Paul Hansma and coworkers [94] followed the polymerization of fibrinogen, a constituent of the extracellular matrix. This investigation was followed by the observation of other biological processes: the response of the cell membrane to a probing tip [71]; the observation of the infection of a cell by viruses [95]; the imaging of living, human platelets during their activation [96], and the monitoring of slow motion on the surface of cells [97]. Other examples for following intracellular transport of material or changes of the underlying cytoskeleton of the AFM have been reported by several groups [71, 93, 97-100].

1.9.3 Forces Affecting the AFM Probe

The sum of the forces on the tip causes the deflection of the cantilever; these forces can be attractive or repulsive. The forces acting on the tip vary depending on the mode of operation and the conditions used for imaging. In contact mode imaging, the tip is deflected, mainly due to repulsive forces from the overlapping electron orbitals between the tip atoms and the sample atoms. The dominant attractive force is a van der Waals force resulting primarily from the nonlocalized dipole-dipole interactions among atoms of the tip and specimen [68, 101]. While imaging in fluids contributions from electrostatic Coulomb interactions between charges on the specimen and tip (either occurring naturally or induced because of polarization), osmotic pressure due to charge movements and rearrangements, and structural forces such as hydration force, solvation force, and adhesion force should be considered [74]. The manner in which the AFM generates images also makes the AFM an excellent sensor of molecular forces (hydrogen bonds, van der Waals and electrostatic forces) [102, 103].

1.9.4 Measuring the Elastic Properties of Biological Material with the AFM

The elastic response of the cell is mainly due to its cytoskeleton [104, 105]. The cytoskeleton is a network of three different polymeric proteins: actin, microtubules, and intermediate filaments, along with a large number of associated proteins that control assembly, disassembly, crosslinking, and other properties of this filament network [106]. The cytoskeleton is related to the cell shape, the change of this shape, and the self movement of the cells [32, 107].

The principle of the cell poker is very similar to the method of using an AFM [108, 109]. Other methods have been used to measure the entire cell's elastic properties including pipette suction method [110, 111], flicker spectroscopy [112], and optical tweezers [113, 114]. Bereiter-Hahn and coworkers used another scanning microscopy technique, scanning acoustic microscopy, to measure the elastic properties of cells locally [115, 116]. The main difference between AFM and these techniques is the high lateral resolution (100 nm) provided by the AFM with the potential to even further increase such a resolution with improved tip design [90].

AFM data is interpreted as elasticity measurements [117-120]. The AFM allows the mechanical properties of biomolecules to be determined accurately from force-versus-distance curves (force curves) [121, 122]. The relationship between indentation force and depth depends upon the tip geometry and the mechanical properties of the specimen [123]. Measuring the elastic properties of biological material with the AFM has been pioneered by Lindsay [120] who investigated the difference of bone and bone marrow, and by Weisenhorn [87] who investigated rubber, cartilage, and living cells. If the sample is soft the tip will deform it, and elastic indentation occurs. The force-indentation relationship is non-linear for softer samples, because the compliance of the sample becomes higher for larger loading forces. Radmacher considers the geometry of AFM tips to be conical, on a scale of several 10's to 100s of nm [90]. The contact area of the probe increases with indentation, the force-depth relationship in any soft material is nonlinear, making it difficult to assess how much of the response is due to the tip geometry[123]. This process has been treated analytically by Hertz, where a relationship between the indentation and the loading force is given for smooth parabolic indenter profiles [124]. Most investigators have attributed nonlinearity of the indentation response entirely to the tip geometry, and have applied equations based on classical infinitesimal strain theory to extract the Young's Modulus of the material [87, 125].

1.9.5 Classical Infinitesimal Strain Theory Applied to Indentation

The indentation problem was originally solved by Hertz [124] for smooth parabolic indenter profiles and by Love [126] for conical indenters for which the Hertz theory does not apply [127]. The classical infinitesimal strain theory is a widely used approach because of the simple form of the theoretical equations[123]. The theory assumes that the sample is a homogeneous, isotropic, linear elastic half-space subject to infinitesimally small strains. It should be noted that each of these key assumptions are questionable for AFM indentation studies of biological specimens. First, at the macroscopic level most biological materials are heterogeneous, anisotropic, and exhibit nonlinear constitute behavior [128]. This could pertain to the microscopic level as well. Second, in order to obtain an adequate indentation response with the AFM, soft biomaterials typically need to be indented 50-500 nm, which is not infinitesimal compared to either the thickness of some cell samples (<2μm) or to the size of the indenter tip (~5-60 nm radius of curvature) [129, 130]. Although the AFM measures on a microscopic scale, the classical theory may still be reasonable because the tip indents 100 or more atoms on the surface [131].

The classical infinitesimal strain theory also indicates that pyramidal and conical indenters should have a semi-angle (α) close to 90 degrees [127] so that the gradient of displacement (strain) at the contact surface remains small (Figure 1.8). AFM tips typically have an α value of 35 degrees. For indenters such as those used for AFM where α<45 [130], the strains are likely to be large in the vicinity of the indenter, even for small indentations relative to the sample thickness. Thus, AFM indentation could be classified as a finite indentation problem, and analyses based on infinitesimal strain theory may be inappropriate.

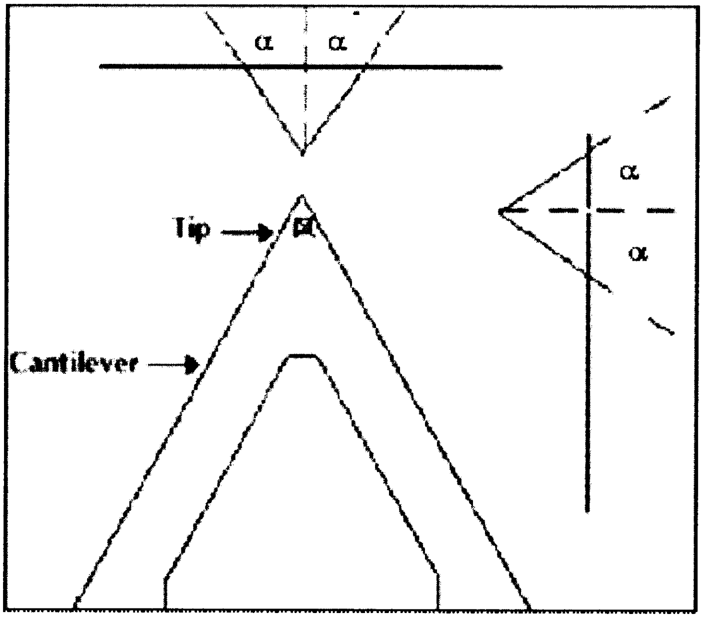

Figure 1.8 Cantilever tip with semi-angle α indicated. Image courtesy of Digital Instruments, Santa Barbara CA.

Infinitesimal strain theory requires an infinitely large specimen relative to both the indentation depth and the indenter size [127]. Indenter geometry relates to this issue because it determines the radius of contact between the indenter and the sample. A conical indenter, in theory, yields an indentation response that closely approximates that of commercially available silicon nitride (Si_3N_4) AFM Probes, the geometry of which is a four sided pyramid [129]. For cylindrical indenters, the contact radius is constant yielding a linear force-depth relation for infinitesimal indentations [132-134]. Nonlinearities arise when either the radius or indentation depth are larger than a certain fraction of the sample thickness [135, 136]. For flat ended circular cylindrical probes which may not fully pertain to AFM tips, the following guidelines were established for indentation tests: the in-plane dimensions relative to the indenter size should be >15, for the effects of finite sized boundaries to be negligible, to avoid nonlinearities and/or incorrect results due to finite thickness effects, the thickness-to-indenter size ratio should be greater than 10, and for the properties of the underlying substrate not to affect the indentation results, the thickness to indentation ratio should be greater than 5 [136].

For a conical indenter, the indentation force depth relationship is always nonlinear because the contact radius increases with indentation depth .In contrast indentations with a blunt cone approached the theoretical solution for a small indentation with respect to the thickness even for nonlinear materials and an angle less than 45 degrees [123]. This is due to the fact that in this limit the indentation depth and contact radius are smaller than the spherical tip radius as required by infinitesimal theory [127]. Costa [123] demonstrated that the two critical factors determining the accurate assessment of elastic properties by indentation are whether the deformations are infinitesimal and whether the material exhibits linear or nonlinear characteristics. Applying infinitesimal theory incorrectly to finite-deformation situations can result in large errors in the estimation of material properties. Correctly accounting for finite indentations and the geometry of the indenter to calculate an apparent elastic modulus, may reveal material nonlinearity and heterogeneity [123]. However, Some researchers consider that the absolute determination of the Young's modulus of a biological sample is not always necessary, where only a comparison between two different states is needed [131].

1.9.6 Theoretical Analysis with Conical and Blunt-Tipped Indenter Geometry

The indenter tip of an AFM, does not terminate in a point but instead is truncated in some way. Costa [123] used finite element models (FEM) to simulate a blunt cone indenter indenting into three materials. The probe was modeled as a cone with a half angle (α) 37.5 degrees which merged smoothly into a spherical tip with a radius R=30 nm simulating an AFM probe. For an indentation (D) to thickness (t) ratio >0.15 the cone and blunted cone data matched within ±10 %; however, for smaller indentations a larger discrepancy was found. Nonlinear materials indented with an ideal cone resulted in the theoretical modulus overestimating the apparent one. In contrast, with a blunt cone indenter the apparent modulus approached the theoretical one as D/t approached zero. It follows that using a blunt cone may allow more accurate quantitative estimates of some elastic properties of a material.

1.9.7 Measuring the Elastic Properties of Biological Material with the AFM

The Young modulus is the basic material coefficient of elasticity. It can range from 100 GPa for hard materials (glass, steel) to 100s MPa for typical polymers (polystyrene), and 1 MPa for soft gel-like materials [90]. Typical values for cells are somewhere between 1 kPa and 100 kPa [87, 137]. In order to accurately derive Young's modulus, the characteristics of the tip such as the tip radius, the cone angle and the force constant should be carefully estimated [129, 138-140]. In addition, the tip deformation should be negligible. In the case of Si_3N_4 tips, the modulus of Young is 150 GPa [87, 141] and for commercial silicon cantilevers it takes the value of 169 GPa (according to the manufacturer, Digital Instruments). The supporting sample (glass substrates) is crucial too, because it is often used as a reference sample appearing hard compared to biomolecules. Glass itself is softer than the Si_3N_4 tip with a Young's modulus of 50 GPa and has a spring constant of about 50 N/m [87].

The elastic response of living and fixed cells has been reported qualitatively in the work by Schoenberger and Hoh [142] and in the work of Lal and coworkers [78].Weisenhorn et al. [87] were the first to measure the elastic properties of a living cell, and to quantify the elastic behavior of cells from force curves, obtaining a Young modulus of 0.013-0.15 MPa for a living (lung carcinoma) cell. Radmacher and coworkers [84] were the first to determine quantitatively the elastic properties of cells as a function of the AFM position on the cell, finding Young moduli ranging from 1 to 50 kPa (Hertz' model) [124]. Radmacher's observed correlation between the position on the platelet and the changing elastic modulus is an interesting observation, which was found to be related to the underlying cytoskeleton. However, a discrepancy was observed between the experimental data and simulations based on Hertz' model. Micromechanical measurements performed on cultured rat atrial myocytes also showed a similar dependence of the elastic modulus on the position on the cell [143]. Young's modulus in a nuclear region of the cell was 0.5-0.67 MPa (Ca2+-free solution, Sneddon mechanics), and increased 5-8-fold toward the periphery. These variations in stiffness could be related to the cytoskeletal heterogeneity [143]. According to Costa [123] the correct classical infinitesimal strain theory equations [133, 144]} have been reported incorrecyly in several AFM publications [73, 84]}. Therefore, the mechanical properties of biological samples determined in previous work may be questionable.

CHAPTER 2

ATOMIC FORCE MICROSCOPY NANOINDENTATION ON CARDIAC MYOCYTES

2.1 Introduction

This chapter discusses experimental measurements conducted on cardiac myocytes isolated from young and old rats. This published study [145] demonstrates that aging exerts an effect on the material properties at the single cardiac myocyte level. The AFM and its nanoindentation function made it possible to test the hypothesis that aging affects the material properties of single cardiac myocytes independent of the size of the cell.

2.2 Materials and Methods

2.2.1 Animals

Variation in the apparent elastic modulus with cell length was studied in 2 month old male Sprague Dawley rats (n=3) (Charles River Breeding Laboratories Inc.). Aging effects were studied in male F344xBN rats obtained from the National Institute on Aging colony. AFM studies were conducted on rats of 4 (n=4) and 30 (n=4) months of age representing young and old rats, respectively [59, 146]. Cardiac myocyte contractile and relaxation function and measurement of myocyte general dimensions (length, width) were conducted in a parallel group of male F344xBN rats of 4 (n=3) and 30 (n=3) months of age. The myocyte cross-sectional area was measured in a third group of male F344xBN rats of 4 (n=3) and 30 (n=3) months of age.

2.2.2 Preparation of LV Myocytes

Cardiac myocytes were prepared from male F344xBN rats and Sprague Dawley rats respectively as previously described [147, 148]. In brief, the heart was rapidly excised and perfused with basic solution composed of MEM (Sigma, Joklik's modification, M 0519), taurine (5mM), creatine (2mM), hepes (5 mM), $NaHCO_3$, Insulin (20 U) and Penn Strep (1%) containing 75 U/ml each of collagenase 1 and 2 (Worthington Biochemical, Freehold, New Jersey, USA) at 37°C. All solutions were continuously bubbled with 95% O_2 and 5% CO_2 at 37°C. The digestion was stopped by adding MEM solution containing $CaCl_2$ 0.3mM and 6% BSA for 10 minutes. In every 10 minute period the supernatant was removed and the MEM solution was added in a stepwise manner with $CaCl_2$ concentration (0.5 and 1.0 mM). The myocytes were washed twice with culture medium. Young rat myocyte isolations resulted in a yield of approximately 70% whereas isolations in old rats resulted in approximately 40% yield.

2.2.3 Measurement of Contractile and Relaxation Function

Myocytes were transferred to a warmed (37°C) and continuously perfused cell chamber located on an inverted microscope stage (Nikon Inc., Melville, New York, USA). The chamber was perfused with physiological buffer containing (in mmol/l): 120 NaCl, 2.6 KCl, 1.2 $MgCl_2$, 1.2 KH_2PO_4, 11 glucose, 5 HEPES, 25 $NaHCO_3$, 2 taurine, 1 pyruvate, and 1 $CaCl_2$. Myocyte contraction was induced at 1 Hz by platinum field electrodes that were placed in the cell chamber and attached to a stimulator (S48; Grass Instrument Co., Quincy, Massachusetts, USA). Cell images were continuously monitored through an x20 objective lens (Nikon Inc.) and transmitted to a charge-coupled device (CCD) video camera (TM-640; Pulnix, Mountain View, California, USA). The output from the CCD camera was displayed on a video monitor (PVM-135; Sony, New York, New York, USA). The myocyte length was measured using a video motion edge detector (VED103; Crescent Electronics, Sandy, Utah, USA), and the data were acquired at 240 images per second. The percent contraction was calculated from the length data where the myocyte length was calibrated with a hemocytometer grid placed on the microscope stage.

2.2.4 Cell Morphology

Measurements of myocyte length and width were made from photomicrographs of the isolated myocytes and a computerized image-analysis system (Scion Corporation, Maryland USA). Dimensions were calibrated with a hemocytometer grid placed on the microscope stage. A separate method was used to measure myocyte cross-sectional area in LV tissue fixed in formalin involving the MetaMorph image system software (Universal Imaging, West Chester, PA, USA). Myocyte outlines were apparent after silver-staining methacrylate embedded sections (1-µm thick), which were obtained midway between the LV base and the apex. Traces of approximately 100 myocyte outlines were obtained in the LV of each animal.

2.2.5 Atomic Force Microscope Operation

Indentation tests were conducted with a Digital Instruments MultiMode AFM, Nanoscope IIIa control system, fluid cell, and a "J" scanner (Digital Instruments, Santa Barbara, CA) (Figure 2.1). A Digital Instruments MultiMode AFM, fluid cell, and a "J" scanner are shown in Figure 2.1 (a). Figure 2.1. (b) shows a schematic of the nanoindentation procedure with the Digital Instruments MultiMode AFM. The Nanoscope IIIa control system (A) signals the AFM head (B) to operate in contact mode and directs the movement of the piezoelectric xyz "J" scanner (C) in the z-direction and not in the xy-plane. The sample (D) is indented by the AFM probe (E). The deflection of the AFM cantilever (F) is monitored by emitting a laser beam (G) from a source (H) which after deflecting off the AFM cantilever (F) is directed by a mirror (I) into a position-sensitive photodetector (J). The measurements are sent through the Detector Electronics (K) returning to the Nanoscope IIIa control system (A) for data collection. Figure 2.1 (c) shows a schematic, not to scale, of the nanoindentation of a section of the myocyte sample with a blunted AFM probe. Boundary effects and nonlinearities in AFM measurements are avoided because the ratio (~161) of the actual myocyte thickness (~15 μm) to indentation depth (~93 nm) greatly exceeds the value of 5, and the ratio (~375) of the myocyte thickness (~15 μm) to indenter radius (~40 nm) is greater than the accepted value of 10. Moreover, in-plane boundary effects are avoided because the ratio (~2900) of myocyte length (~120 μm) to indenter size (~40 nm) as well as the ratio (~750) of myocyte width (~30 μm) to indenter size (~40 nm) are much greater than the accepted value of 15 [136].

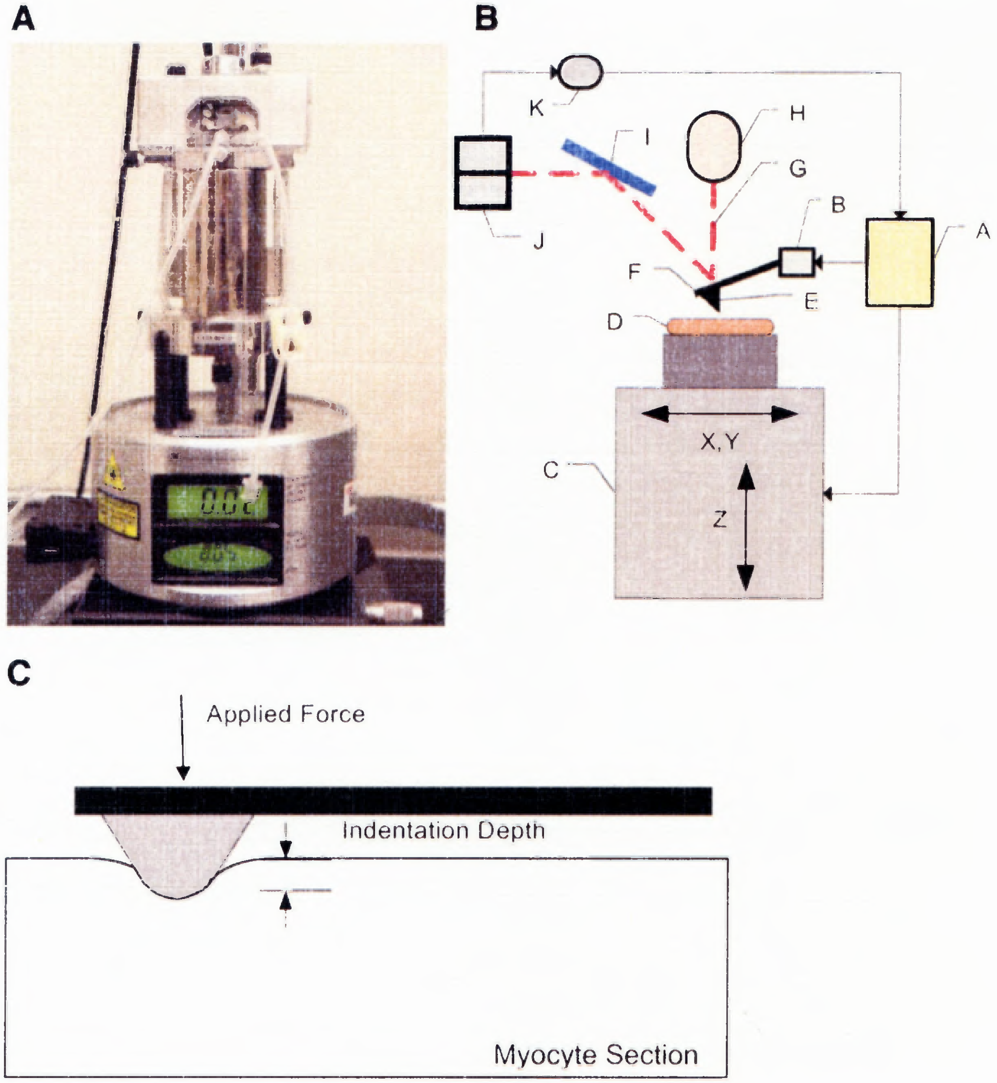

Figure 2.1 Digital Instruments MultiMode AFM, fluid cell, and a "J" scanner.

After isolation, myocytes were plated on customized (15 mm diameter) tissue culture treated petri dishes (Becton Dickinson, Bedford, MA) coated with 20 μg/ml of laminin (Sigma Chemical Co., St. Louis, MO, USA). The myocytes were studied within 6 hours from the time of isolation. When the cells were not analyzed with the AFM they were kept in a CO_2 water jacketed incubator (Thermo Forma Model 3110 Series), which kept the cells in a 37°C, 5% CO_2, humidified environment. AFM experiments were conducted by placing the myocytes plated on the 15 mm diameter petri dishes into the AFM

Multimode head. The cells were studied in a 37 ^{o}C culture media environment by using the AFM fluid cell at room temperature. All AFM measurements were conducted within one hour after insertion into the AFM head. Etched silicon nitride probes (NP-20) were used in these experiments. The NP-20 probe used had a tip radius of 20-60 nm, a cone angle of 35°, and was attached to triangular cantilevers 200 μm in length with a spring constant of 0.06 N/m (Digital Instruments, Santa Barbara, CA). The same NP-20 probe-cantilever was used throughout the experiments in order to avoid the variation of the cantilever spring constant with different AFM probes. The NP-20 sensitivity was determined consistently near 50 nm/V. The indentation protocol involved no scanning in the horizontal (xy)-plane. The cantilever was positioned directly above the surface of an immobilized myocyte with the aid of an X 30 magnification eyepiece. Proper force curves were obtained in the force calibration mode by setting the z-scan start at +220 volts with the z-scan size set at +440 volts, and a low frequency of 0.6 μm/sec, which was found to minimize not only hysteresis (Figure 2.2), but also drag force, and maximize the number of force curves that could be captured [149, 150]. Hysteresis was calculated as previously described by subtracting the area under the curves for retraction (A_{ret}) from extension (A_{ext}), which represents the energy dissipated into the cell from the indentation of the AFM tip [149]. This area was normalized by dividing the hysteresis value by the input energy, A_{ext}. The apparent elastic modulus was found to be reproducible at that frequency, and below. Force curves were taken at three positions along the middle of the longitudinal axis, as in previous work [150]. The effects of replicate indentation in the same location were studied to verify that the cell behavior and material properties did not change with repeated indentations, as shown in previous studies [149, 150].

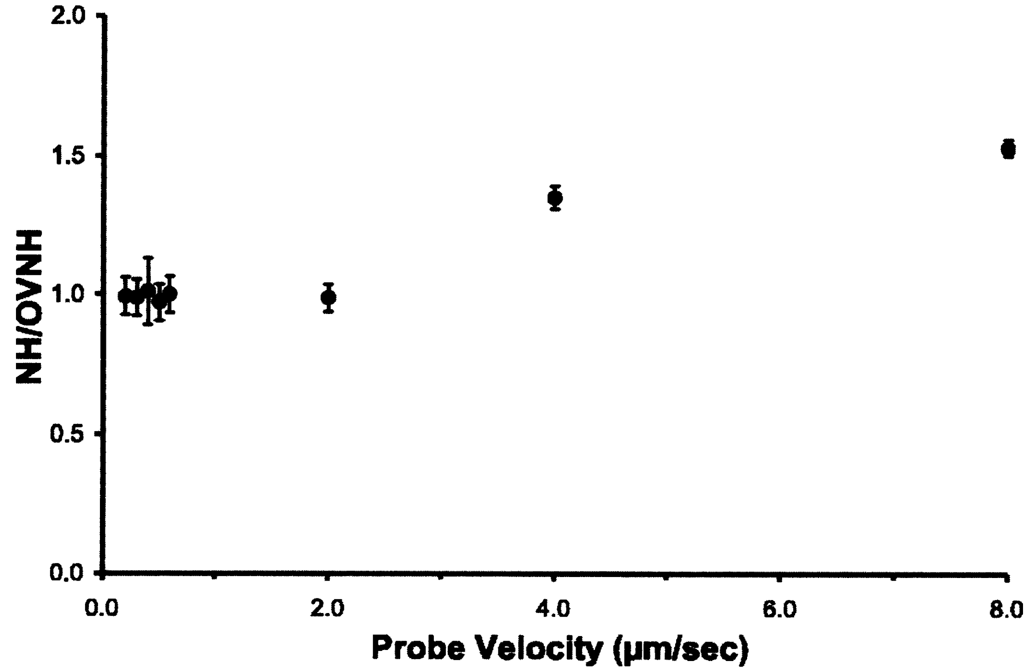

Figure 2.2 The selected probe velocity (0.6 μm/s) minimized hysteresis shown in the figure plotting the ratio of the normalized hysteresis (NH) to the operating velocity's normalized hysteresis (OVNH) with respect to probe velocity.

The indentation force (F) was calculated using Hooke's law ($F = k\delta$) where k and δ denote the cantilever's spring constant and the cantilever's measured deflection, respectively (see, e.g., ref [150]). The indentation depth (d) was calculated from the difference in the z-movement of the piezo and the deflection of the cantilever [123, 149, 150]. The general equation for the total force F exerted by an indenter for infinitesimal indentation, according to CIST with a blunted conical indenter, is given as [123]

$$F = \Omega \cdot E \tag{2.1}$$

where

$$\Omega = \frac{\pi \cdot \phi(d)}{(1-\nu^2)} \cdot \tag{2.2}$$

Here, E refers to the apparent elastic modulus, ν denotes the Poisson ratio, and d is the indentation depth. The Poisson ratio ν is assumed to be 0.5 for cells [151]. The function ϕ(d) used in this work is that corresponding to a blunted conical indenter shape with tip angle 2α (α = 35°), and radius r (r = 40 nm). Its analytical expression has been previously reported [123]. The elastic properties are defined as an "apparent" elastic modulus, because there are viscous contributions within the cellular response [123]. The apparent elastic modulus was determined by plotting the extension force in equation 1 above as a function of the coefficient Ω, and by identifying the resulting slope with the apparent elastic modulus (E).

2.2.6 Calculating the Contact Force

The force curve shows the relationship between the setpoint and the deflection of the cantilever. Because the setpoint defines the value of the deflection signal maintained by the feedback loop, the force curve can be used to calculate the nominal contact force of the tip on the sample if the spring constant, of the cantilever, is known. The contact force is defined by the equation F =kΔZ, where ΔZ is the distance from the control point to V_{CSmin} in nanometers. Local variations in the form of the F vs. D curve indicate variations in the local elastic properties. In the linear region of the F vs. D curves, the slope is related to the elastic modulus of the system.

2.2.7 Force Distance Curve Analysis with Classical Infinitesimal Strain Theory

Classical infinitesimal strain theory is a widely used approach [123]. The fundamental assumptions of the theory are that the sample is a homogeneous, isotropic, linear elastic half-space subject to infinitesimally small strains. These are the assumptions we have made regarding the cell-body material.

The following is the general equation for the total force (P) exerted by an indenter for infinitesimal indentations perpendicular to the finite stretch for the case of linear hyperelastic materials (see Appendix A for development of formula) [123, 133].

$$P=\frac{4}{3}\cdot E\cdot\pi\cdot\phi(d) \qquad (2.3)$$

E is Young's modulus and $\phi(d)$ is a function of the indenter geometry, which determines the dependence of P on the penetration depth (d). The indentation problem can be solved for different indenter geometries by developing the appropriate $\phi(d)$ and inserting it into (2.3). The following are $\phi(d)$ developed for the cone and blunted cone indenter shapes used in this analysis. A cone with tip angle, 2α is represented by the following function (see Appendix A for development of the function) [126, 133].

$$\phi(d)=\frac{2\cdot\tan(\alpha)}{\pi^2}\cdot d^2 \qquad (2.4)$$

A blunt cone with tip angle 2α, which transitions at radius R (see Appendix A for development of the function) [152]. For a smooth transition from the cone to the spherical tip, $b=R\cos(\alpha)$.

For $d < b^2/R$, $\phi(d)$ is given by a sphere with radius R.

$$\phi(d)=\frac{4}{3\cdot\pi}\cdot\sqrt{R\cdot d^3} \tag{2.5}$$

For $d \geq b^2/R$, $\phi(d)$ is given by

$$\phi(d)=\frac{2}{\pi}\cdot\left[a\cdot d-\frac{a^2}{2\cdot\tan(\alpha)}\cdot\left(\frac{\pi}{2}-\operatorname{asin}\left(\frac{b}{a}\right)\right)-\frac{a^3}{3\cdot R}+\sqrt{a^2-b^2}\cdot\left(\frac{b}{2\cdot\tan(\alpha)}+\frac{a^2-b^2}{3\cdot R}\right)\right] \tag{2.6}$$

where the radius of contact a is derived from [152]

$$d+\frac{a}{R}\cdot\left(\sqrt{a^2-b^2}-a\right)-\frac{a}{\tan(\alpha)}\cdot\left(\frac{\pi}{2}-\operatorname{asin}\left(\frac{b}{a}\right)\right)=0 \tag{2.7}$$

A Newton's method [153] was applied to (2.7) with a tolerance of 10^{-15} in order to find the radius of contact a.

The cardiac myocyte apparent elastic modulus was found to be constant (up to 2%) at three positions on the cell's longitudinal line close to the center, avoiding boundary effects. All data reported here were obtained at a probe speed of 0.6 μm/sec and analyzed at the depth of 93.2 ± 0.1 nm (n=111) from the approaching part of the force curve. In order to verify that nonlinearities associated with finite thickness effects are avoided we measured the adult cardiac myocyte thickness by confocal microscopy (14.5± 0.7 μm, in good agreement with published data [154]) and found that the myocyte thickness-to-indentation depth ratio exceeds by far the accepted value necessary to avoid nonlinearities [136]. Moreover, the indentation depth (~93 nm) and probe size (~40nm) were sufficiently minimal to prevent the underlying substrate properties and boundary effects from affecting indentation results. As noted in Table 2.1 there were differences in the number of myocytes that could be studied successfully from each animal, with variations from animal to animal but not between old and young.

Table 2.1 Average Elastic Modulus and Number of Myocytes Measured per Animal

	Young Rat (4 months)			
	Rat 1	**Rat 2**	**Rat 3**	**Rat 4**
Average Elastic Modulus (kPa)	36.2 ± 1.0	35.7 ± 2.0	34.6 ± 1.3	36.2 ± 1.0
n (# of cells)	21	7	17	8

	Old Rat (30 months)			
	Rat 1	**Rat 2**	**Rat 3**	**Rat 4**
Average Elastic Modulus (kPa)	44.2 ± 1.9	42.2 ± 2.6	42.7 ± 1.7	40.6 ± 1.9
n (# of cells)	12	12	21	13

2.2.8 Geometry Independence of Apparent Elastic Modulus

Hypertrophy is known to be characteristic of aging; however, the apparent elastic modulus is a material property measure and should be independent of geometry. To prove that this is the case, we conducted an experiment on 2 month old Sprague Dawley Rats (n=33 cells from 3 animals). The apparent elastic modulus was determined as described above and myocyte morphology was determined by conducting photomicroscopic measurements with the AFM Multimode's X 30 magnification eyepiece and image analysis software (Scion Corporation, Maryland USA). Myocyte morphology (length, width) was calibrated by using the AFM cantilever known length (200 μm) (Figure 2.3).

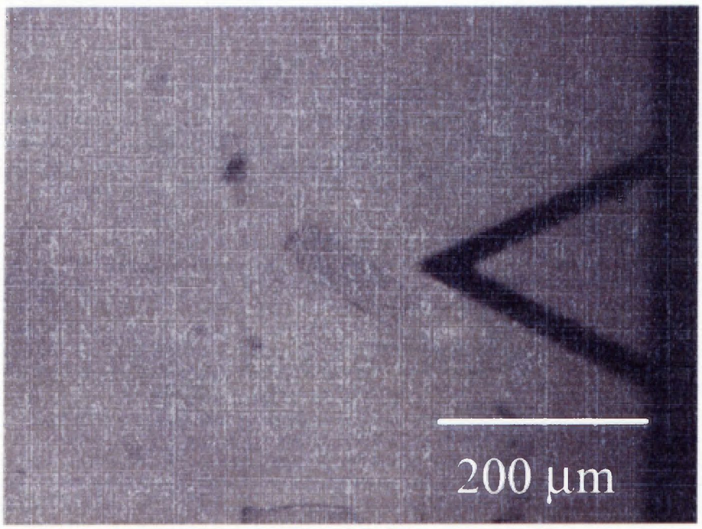

Figure 2.3 Image of AFM probe with cardiac myocyte. Length of the cantilever (200μm) used as a scale to measure myocyte dimensions.

2.2.9 Statistical Analysis

All data are presented here as mean ± standard error of the mean (SEM) and the statistical significance was determined by calculating a probability value (p) with an Analysis of Variance (ANOVA) t-test. Values of $p<0.05$ were considered to be significant.

2.3 Results

2.3.1 Myocyte Contractile and Relaxation Function

Figure 2.4 shows representative contraction/relaxation recordings at baseline in young and old rats . Figure 2.4 (a) shows a photomicrograph of a representative myocyte used for morphological and contractile measurements obtained through a x40 objective lens (Nikon Inc.), charge-coupled device (CCD) video camera (TM-640; Pulnix, Mountain View, California, USA), and video capture system. Figure 2.4 (b) shows a representative contraction/relaxation recording at baseline in young and old rats, demonstrating a difference in myocyte contraction and relaxation with aging Figure 2.4 (c) shows how age affects myocyte contraction and relaxation, where the % contraction data shows a significant (*$p<0.01$) decrease (38.3%) and a significant (*$p<0.01$) increase (88.2%) in the time for the myocyte to return from the contracted state to 70 % of its original length.

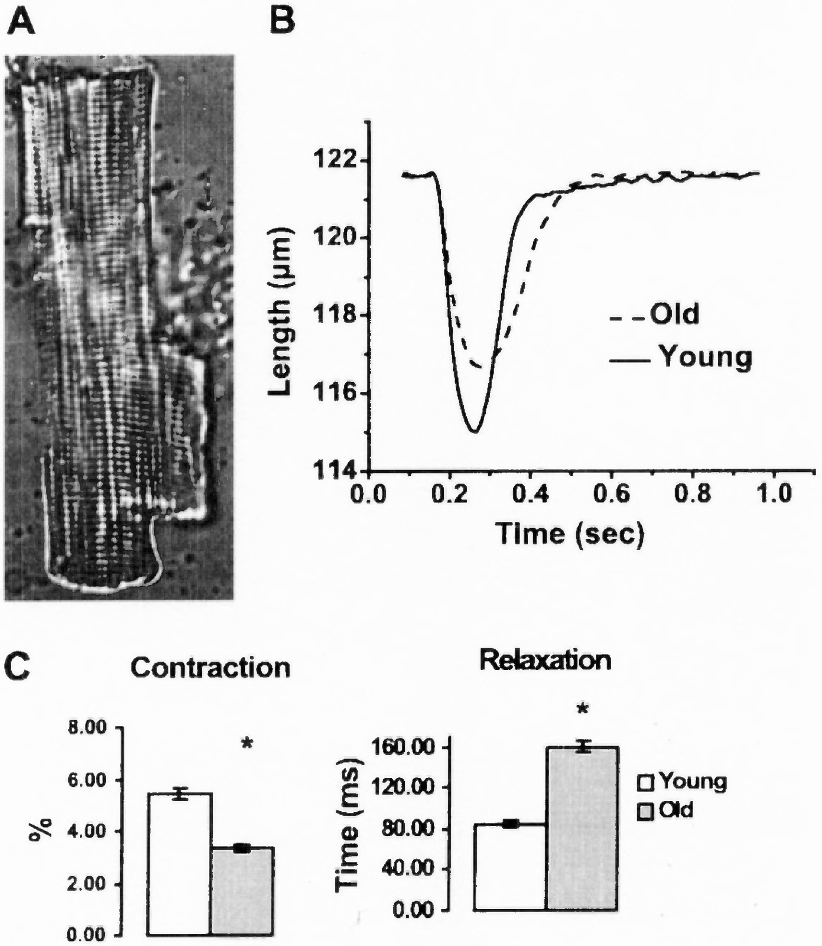

Figure 2.4 Contractile measurement summary.

A significant ($p<0.01$) decrease in myocyte contraction was found from young (5.4%) to old (3.4%). The relaxation function as assessed by the time required for 70% relaxation was also increased in old myocytes (159.7 msec.) compared with young myocytes (84.9 msec.).

2.3.2 Myocyte Morphology

A significant increase ($p < 0.01$) was seen in length from young (113.7±1.5 µm (n=64)) to old (120.0±1.8 µm (n=70)) and also an increase in width from young (28.2±0.5 µm (n=64)) to old (31.5±0.7 µm (n=70)). A significant 22% increase ($p < 0.01$) was also seen in the cross-sectional area from young (249±9.3 µm^2) to old (305±12.7 µm^2) (Table 2.2).

Table 2.2 Myocyte Size and Morphology

	Young (4 mos)	**Old (30 mos)**	
Rest Length (µm)	113.7±1.5 (n=64)	120.0±1.8 (n=70)	p<0.01
Rest Width (µm)	28.2±0.5 (n=64)	31.5±0.7 (n=70)	p<0.01
Cross-Sectional Area (µm^2)	249.0±9.3 (n=257)	305.2±12.7 (n=184)	p<0.01

2.3.3 Geometry Independence of Apparent Elastic Modulus

Figure 2.5 shows that there was no significant difference in the apparent elastic modulus 32.4±2.5 kPa, 31.8±0.7, 35.1±2.1 kPa, and 30.8±1.7 determined from myocytes of length 71.2±2.4 µm (n=6), 89.8±1.3 µm (n=11), 104.3±1.0 µm (n=6), and 131.5±2.8 µm (n=10) respectively with an average modulus value of 32.3± 0.7 kPa.

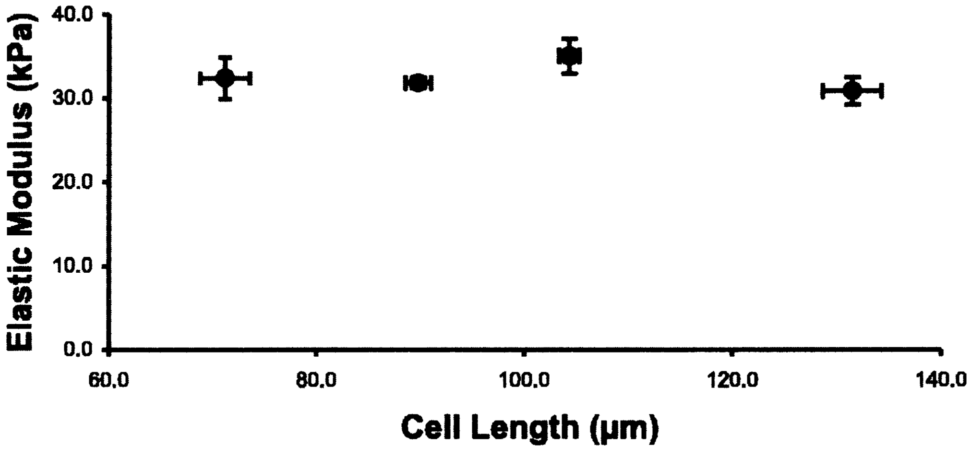

Figure 2.5 Study demonstrating that the apparent elastic modulus is a material property essentially independent of geometry.

Myocytes isolated from 2 month old Sprague Dawley Rats (n=33 cells from 3 animals) showed no significant difference ($p>0.05$) in the apparent elastic modulus 32.4±2.5 kPa, 31.8±0.7, 35.1±2.1 kPa, and 30.8±1.7 determined from myocytes of length 71.2±2.4 µm (n=6), 89.8±1.3 µm (n=11), 104.3±1.0 µm (n=6), and 131.5±2.8 µm (n=10) respectively..

2.3.4 AFM Measured Effect of Age on Mechanical Properties

A Force-Indentation graph (Figure 2.6 a) was plotted for single cardiac myocytes. The linear regression fit of the force F as a function of the coefficient Ω (Figure 2.6 b) gives correlation coefficient (R^2) values near 1 for the myocytes of young and old F344xBN. The force indentation data fit CIST well with the AFM probe modeled as a blunted conical indenter (R^2 values near 1). The slope of the linear regression fit is then identified with the apparent elastic modulus E of the young and old myocyte cells.

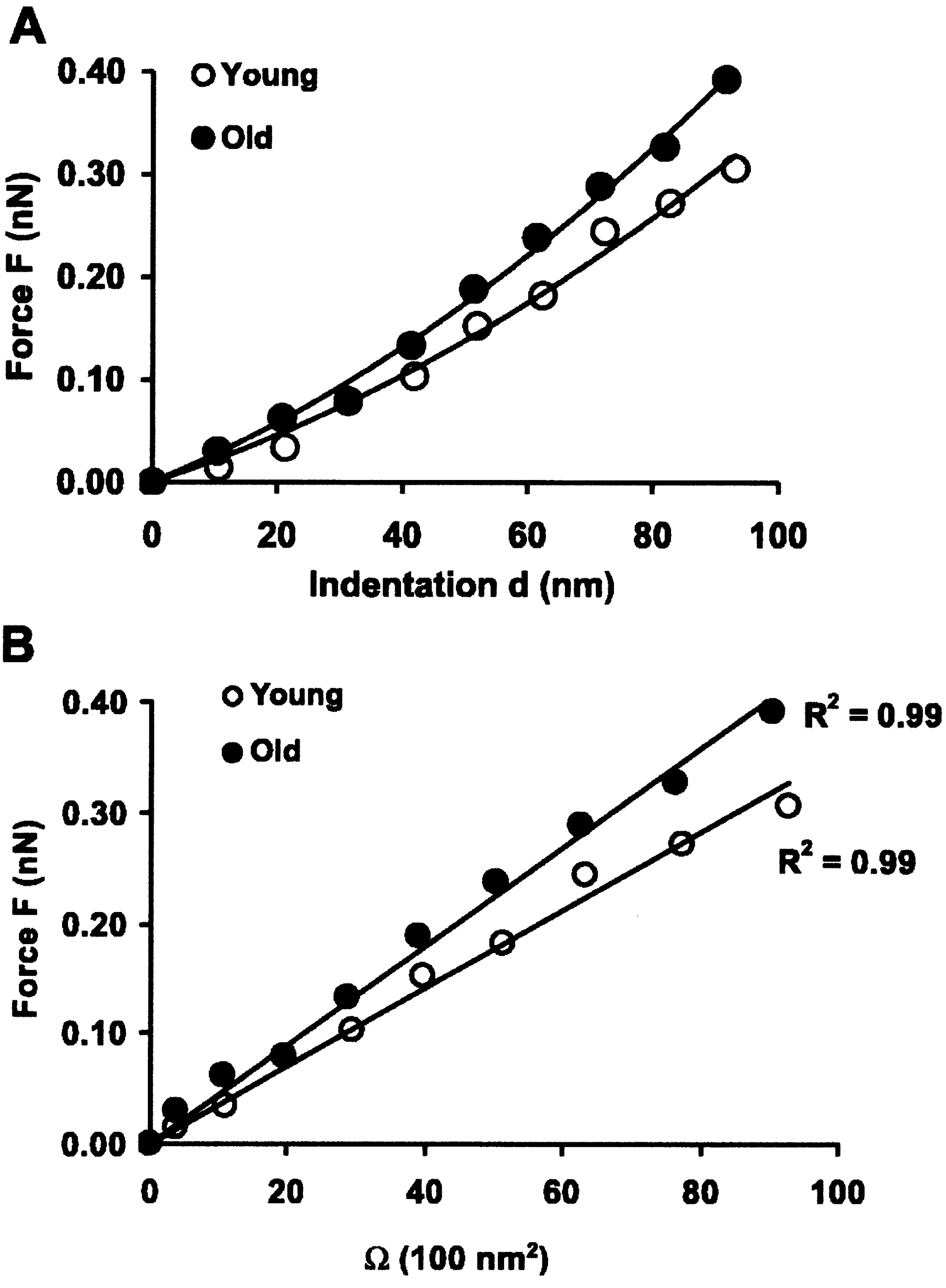

Figure 2.6 (a) Sample Force-Indentation plot on young and old F344xBN myocytes (b) Representative sample plot of the linear regression fit of the force F as a function of the coefficient Ω for young and old F344xBN myocytes.

The slope of this linear regression fit is analyzed as the apparent elastic modulus (E) of the young and old myocyte cells. The cardiac myocyte apparent elastic modulus did not vary significantly between different animals in their respective age group, and the lowest apparent elastic modulus from the old group was significantly higher ($p<0.01$) than the highest apparent elastic modulus from the young group. Therefore, the apparent elastic moduli of myocytes from animals in their respective young and old age groups were grouped for statistical purposes. The average apparent elastic modulus value reported is an average of the results obtained with all myocytes collected from rats in the respective young (4 animals, n=53 cells) and old (4 animals, n=58 cells) F344xBN myocytes. The AFM data (Table 2.1) show a significant difference ($p< 0.01$) in the apparent elastic modulus of young vs. old rats 35.1 ± 0.7 kPa (n=53) and 42.5 ± 1.0 kPa (n=58), respectively (Figure 2.7).

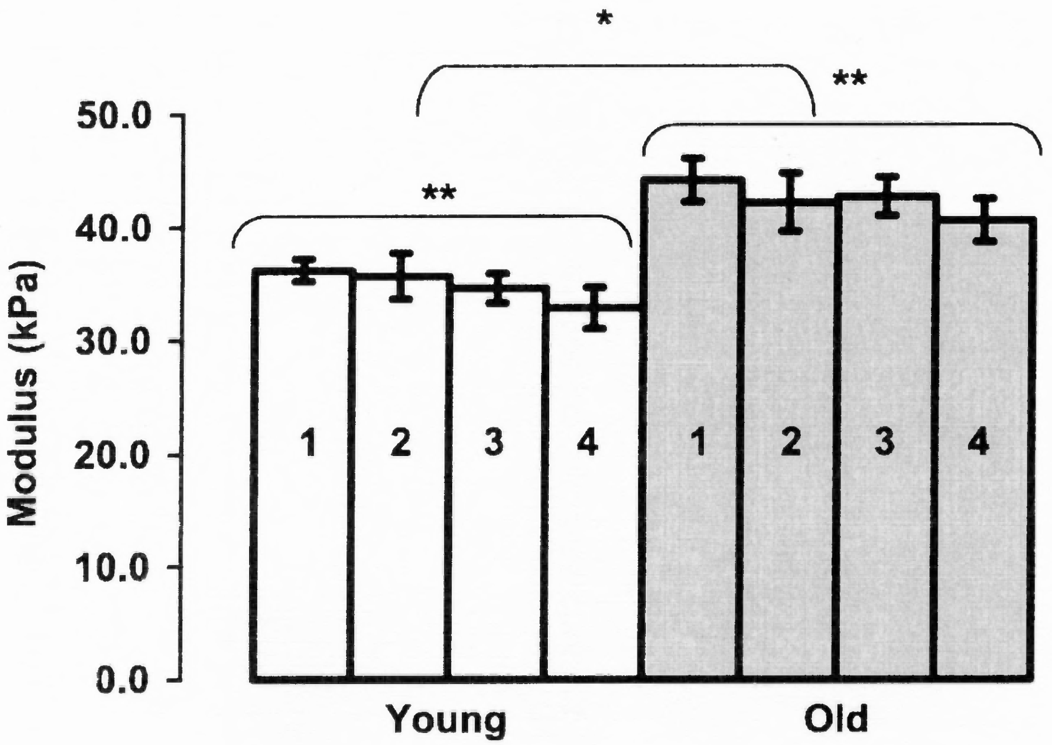

Figure 2.7 The apparent elastic modulus of young and old myocytes.

The cardiac myocyte apparent elastic modulus did not vary significantly between different animals in their respective age group (**$p > 0.05$). AFM data show a significant difference (*$p<0.01$) in the apparent elastic modulus of young and senescent rats: 35.1 ± 0.7 kPa (n=53) and 42.5 ± 1.0 kPa (n=58), respectively, demonstrating a 21% increase with age. The AFM data show no significant (NS) difference in the effects of replicate indentation in the same cellular location on young (n=9 cells) and old (n=10 cells) cardiac myocytes respectively (Figure 2.8a), while still showing a significant difference ($p<0.01$) in the apparent elastic modulus of young and senescent rats. The cardiac myocyte apparent elastic moduli did not vary significantly (NS) over the time period (0-2 hours, 2-4 hours, and 4-6 hours) during which they were analyzed (Figure 2.8b). However, significant differences ($p<0.01$) in the apparent elastic modulus of myocytes from young and senescent rats were observed at each time period. The ratio of old myocyte normalized hysteresis to young myocyte normalized hysteresis was 0.90, indicating a 10% change in hysteresis with aging.

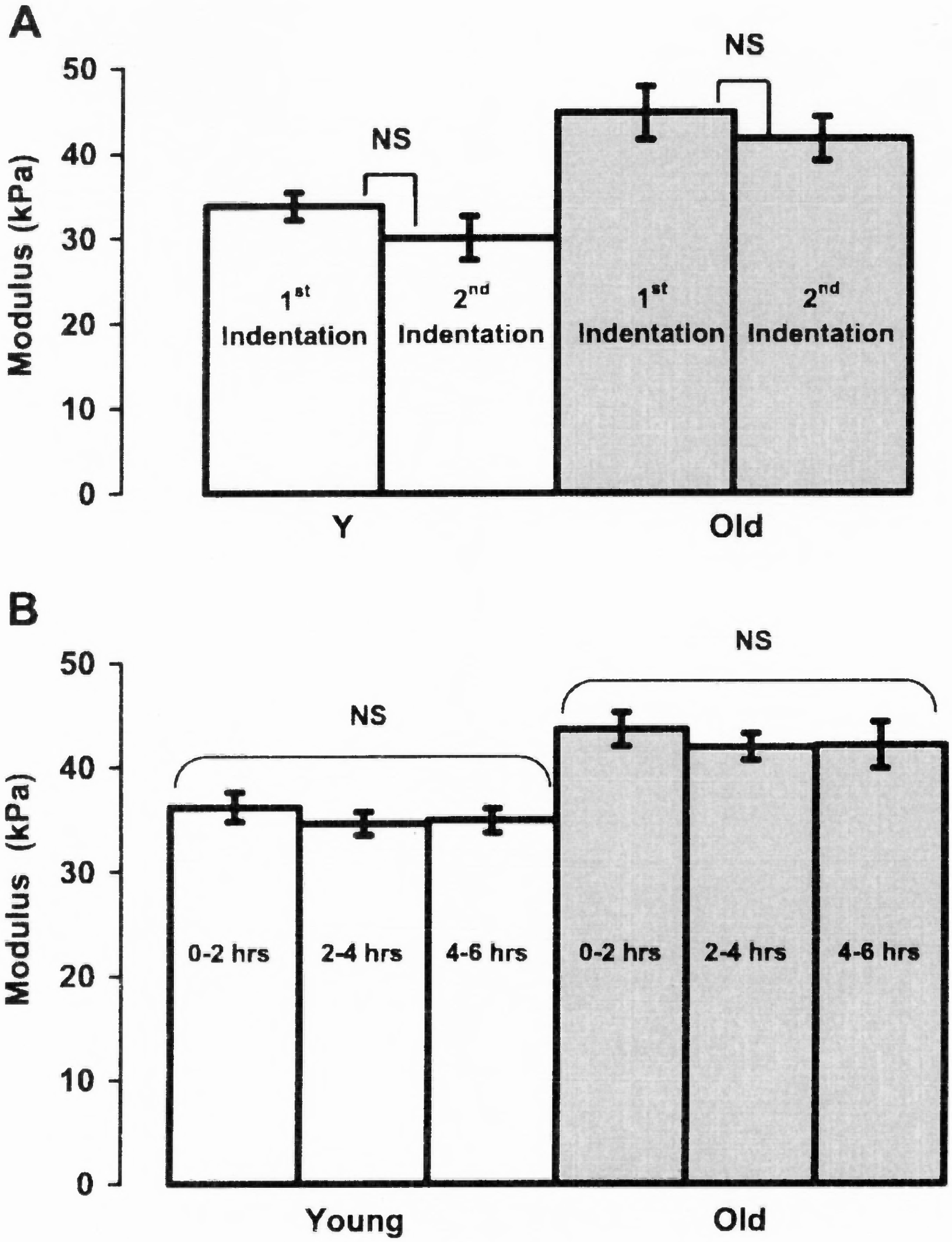

Figure 2.8 (a) Cardiac myocyte apparent elastic modulus between replicate indentations on the same cellular location in the young and old myocytes. (b) Cardiac myocyte apparent elastic moduli over the time period (0-2 hours, 2-4 hours, and 4-6 hours) during which they were analyzed.

CHAPTER 3

FINITE ELEMENT MODEL OF AFM NANO-INDENTATION

3.1 Introduction

This chapter discusses modeling conducted with ABAQUS Finite Element Software in order to investigate how an AFM probe interacts with known materials modeled the same size as a myocyte. The relationship between indentation force and depth depends upon the geometry and mechanical properties of the specimen. Because the contact area of the probe increases with indentation, the force depth relationship in any soft material is nonlinear. Most investigators have used CIST to extract an elastic modulus where the fundamental assumptions of the theory are that the sample is a homogeneous, isotropic, linear elastic half-space subject to infinitesimally small strains. Two accepted hyperelastic materials (Mooney Rivlin, and Polynomial) were chosen to test whether nanoindentation conducted with the AFM into a large object (i.e. myocyte) could be considered infinitesimal small and predict accurately the elastic modulus.

3.2 Modeling

3.2.1 AFM Probe Model

The AFM probe was modeled in ABAQUS as a previously described axisymetric rigid indenter [123] with dimensions provided by the manufacturer (Veeco Metrology) (Height 3 μm, $\alpha=35^{\circ}$, with a 40 nm blunted end) (Figure 3.1 A-B). The Scanning Electron

Microscope (SEM) image of the AFM probe (Figure 3.1C) looks similar to the axisymetric rigid indenter modeled in ABAQUS (Figure 3.1 D).

A

Measure	Size
Tip Height (h)	2.5-3.5 μm
Front Angle (FA)	35°
Back Angle (BA)	35°
Side Angle (SA)	35°
Tip Radius	20-60 nm
Tip Set Back (TSB)	4 μm

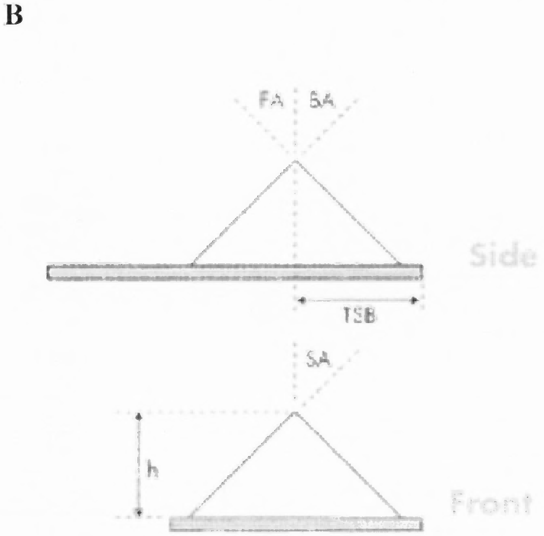

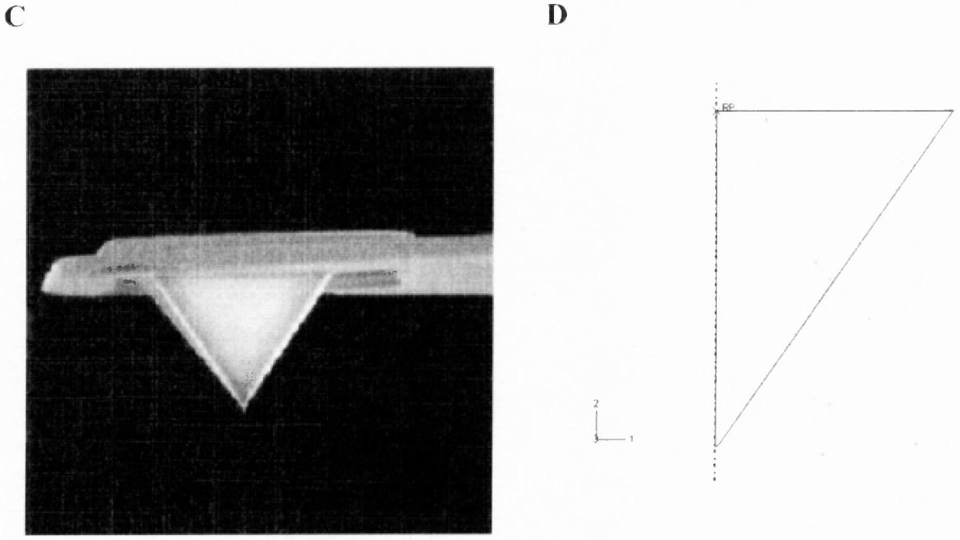

Figure 3.1 (A) AFM probe measures described in the sketch (B). A SEM image of the AFM probe looks similar to the axisymetric rigid model (D) constructed in ABAQUS. (Images A-C provided courtesy of Veeco Metrology).

3.2.2 Sample Model

We constructed a finite element model (FEM) of an incompressible, hyperelastic material (Figure 3.2) to represent a sample the same size as a myocyte.

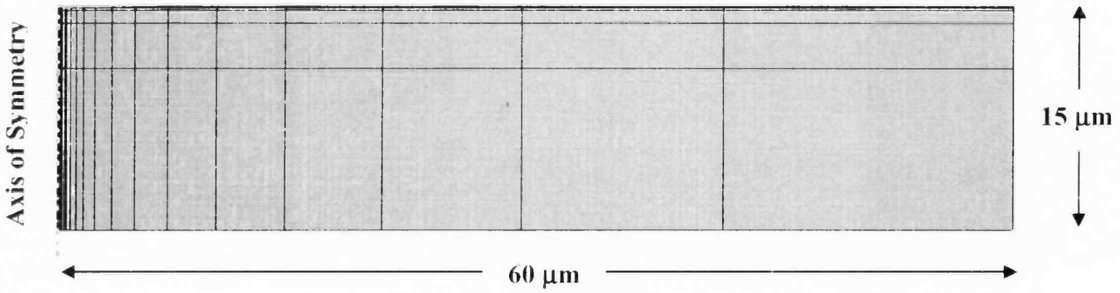

Figure 3.2 Finite Element Model (FEM) of sample to be indented as the same size as a myocyte with a biased mesh providing smaller elements toward axis of symetry.

The myocyte size was chosen to represent the average thickness (15 μm) and length (120 μm) of typical myocytes as discussed in section 2.2.7 and Table 2.2. The model consisted of 330 axisymetric, quadrilateral, bilinear, hybrid elements (10 axially & 33 radially) as previously described [123] biased (100,000 to 1) with smallest elements located under the indenter.

3.2.3 Boundary Conditions

The modeled AFM probe is positioned in contact withy the sample surface as shown in Figure 3.3. Nodal displacements on the bottom surface of the material were unconstrained radially (UR) and constrained axially (CA) to simulate frictionless sliding contact with a rigid substrate (Figure 3.4).

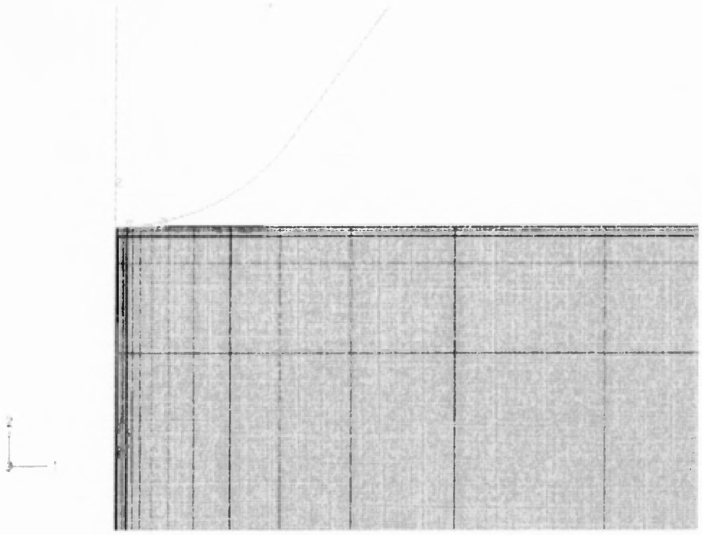

Figure 3.3 Modeled AFM probe in contact with material surface.

The nodal displacements on the axis of symmetry were constrained radially (CR) but unconstrained axially (UA). Contact between the indenter and material was also frictionless. Indentation was caused by incremental axial displacements of the rigid indenter (100 nm) into the cell surface (Figure 3.4). The resulting indentation force (P), is the axial component of the reaction force on the indenter and the indentation depth (d) is of interest because these are the parameters measured with the AFM.

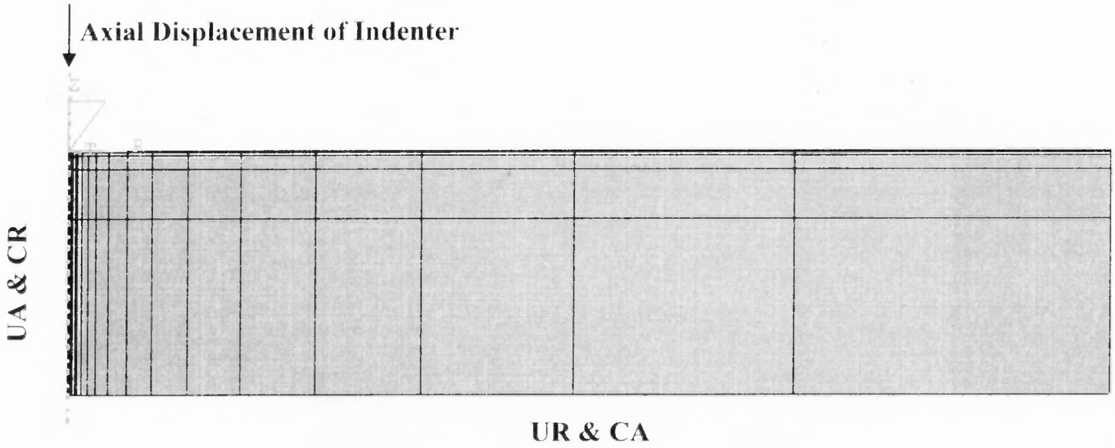

Figure 3.4 Boundary conditions applied to Finite Element Model.

3.3 Materials Tested

The response of two different types of incompressible materials characterized by the following strain energy functions was examined:

Mooney Rivlin $W=C_{10}(I_1-3)+C_{01}(I_2-3)+D$ (3.1)

Isotropic Polynomial $W=C_{10}(I_1-3)+C_{01}(I_1-3)^2+D$ (3.2)

Where I_1 and I_2 are invariants of the Cauchy-Green deformation tensor. Equation 3.1 is the nearly linear Mooney-Rivlin (MR) from characterizing rubberlike material with $C_{10}=0.085$ kPa and $C_{01}=0.025$ kPa and D=0 (incompressible n=0.5). Equation 3.2 is a simple isotropic polynomial (POLY) form to introduce material nonlinearity with $C_{10}=0.167$ kPa and $C_{01}=2.39$ kPa and D=0 (incompressible n=0.5). These values were chosen based on previous work conducted with FEM analysis of AFM indentation [123].

3.4 Results of Mooney-Rivlin and Polynomial Indentation

Figure 3.5 A & Figure 3.6 A demonstrates an enlarged view of the indentation of the MR & POLY material respectively in the ABAQUS Finite element software. The probe reaction force and indentation plot for both the MR (Fig. 3.5 B) and Poly (Fig. 3.6 B) is consistent with what is typically seen in force indentation plots. Applying the similar calculation incorporating Classical Infinitesimal Strain Theory described in section 2.2.7 demonstrates a linear relationship for both the MR (Fig. 3.5c) and POLY (Fig. 3.6c) materials consistent with what is seen in AFM indentation experiments. The maximum reaction force on the bottom surface is significantly smaller (MR: ~800 million times, & POLY ~462 million times) than the force needed to indent the material.

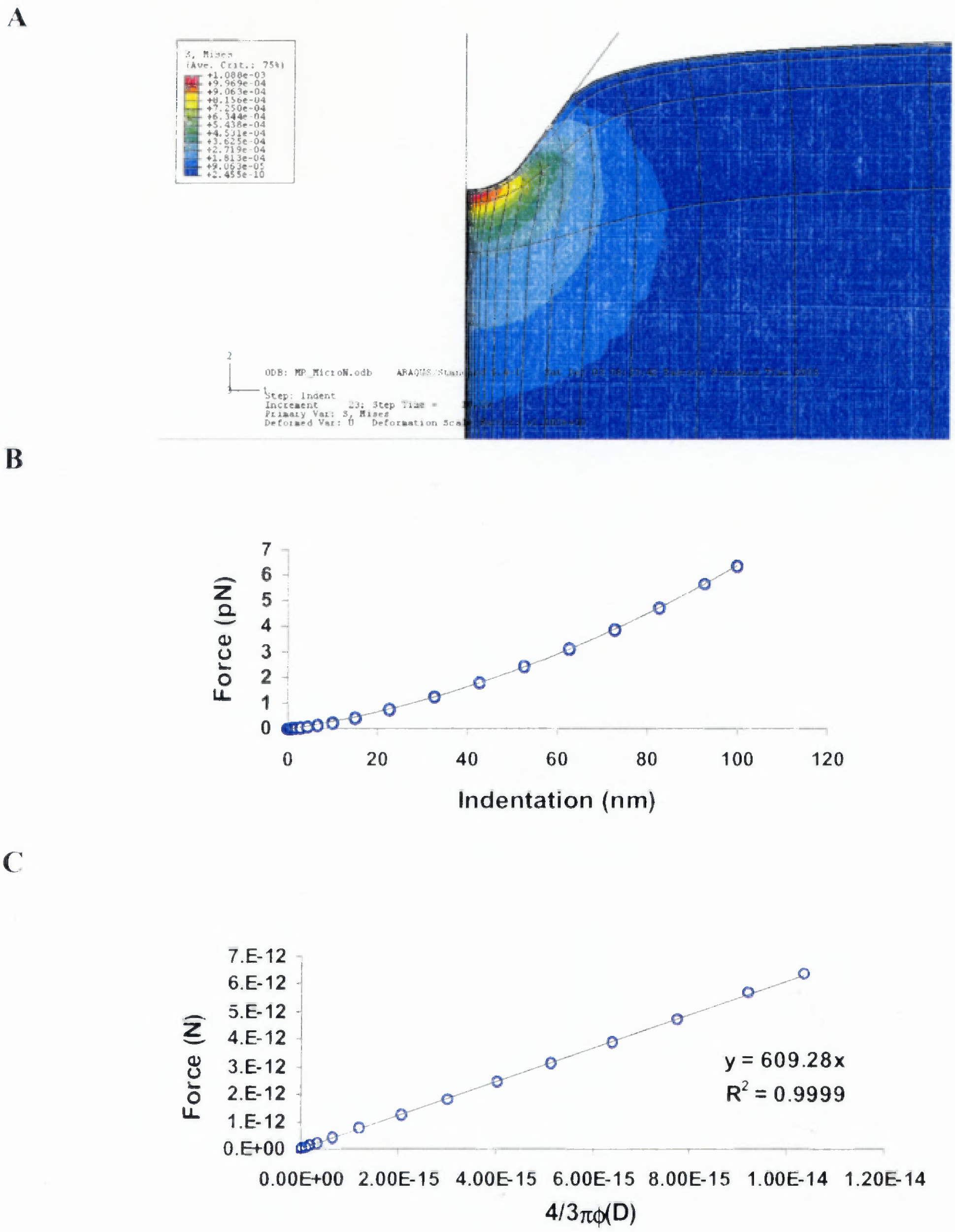

Figure 3.5 (A) 100 nm Indentation of AFM probe into myocyte modeled with an MR material. (B) the reaction Force-myocyte indentation plot compares well to other curves produced from indentation and (C) fitting this data with CIST using a blunted cone model produces a linear effect.

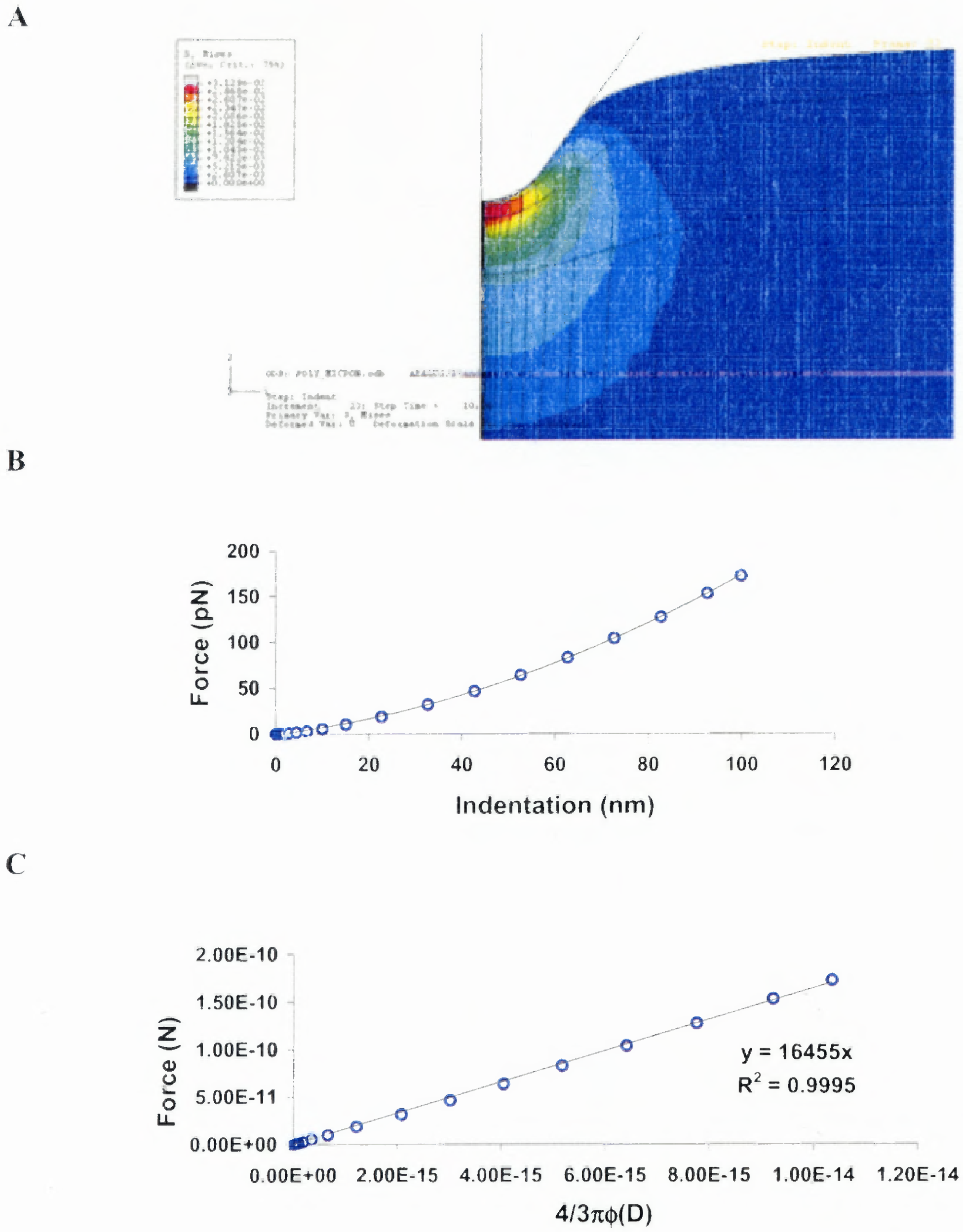

Figure 3.6 (A) 100 nm Indentation of AFM probe into myocyte modeled with a POLY material. (B) the reaction Force-myocyte indentation plot compares well to other curves produced from indentation and (C) fitting this data with CIST using a blunted cone model produces a linear effect.

The Young's elastic modulus of linear hyperelastic materials can be calculated according to the equation given by Green and Zerna [123, 155] (Equation 3.3).

$$E = 6 \cdot (C_{10} + C_{01}) \tag{3.3}$$

A comparison between Young Elastic Modulus determined by the Green equation and that determined on the ABAQUS Force-Indentation data using CIST and the AFM tip modeled as a blunted cone is shown in Table 3.1 for the MR and POLY materials.

Table 3.1 Comparison of Elastic Modulus Determined from Green Equation & F-I Relationship using CIST with the AFM Probe Modeled as a Blunted Cone.

	Green Elastic Modulus	ABAQUS Elastic Modulus
MR	660 Pa	609.3 Pa
POLY	15.342 kPa	16.455 kPa

There is a 7.7 % under prediction of the MR elastic modulus comparing the Green theoretical value to the ABAQUS results (Figure 3.7). There is a 7.3 % over prediction of the POLY elastic modulus comparing the Green theoretical value to the ABAQUS results (Figure 3.8).

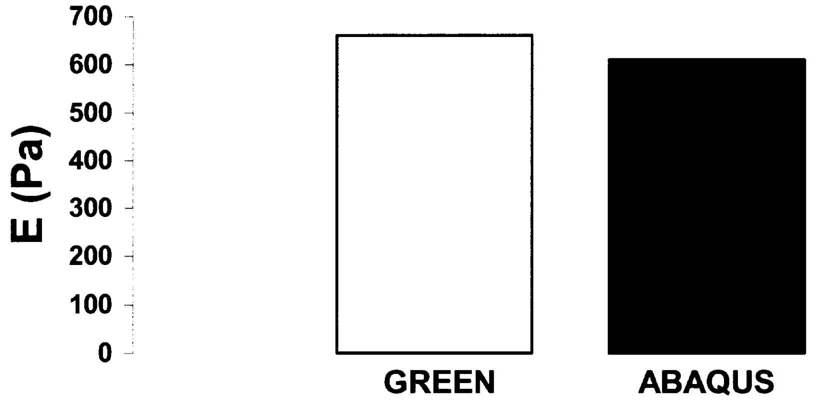

Figure 3.7 MR Young's Elastic Modulus (E) comparison between Green theoretical equation and ABAQUS indentation results.

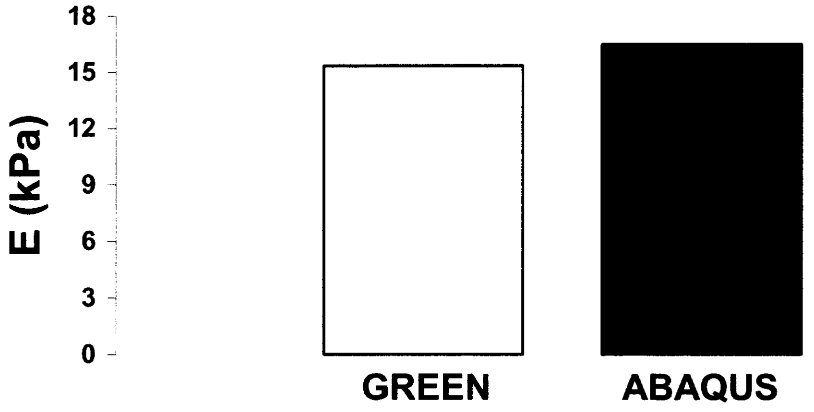

Figure 3.8 POLY Young's Elastic Modulus (E) comparison between Green theoretical equation and ABAQUS indentation results.

CHAPTER 4

MEASUREMENT OF CYTOSKELETAL PROTEINS

4.1 Introduction

This chapter describes experimental work conducted to determine cytoskeleton and mechanotransduction protein changes with aging. Established immunoblot gel electrophoresis (western blot) techniques were used where the conditions necessary to measure each protein type had to first be determined before proteins were quantified in each tissue type. The results indicate that in addition to a material property change, a change in proteins involved in mechanotransduction takes place with aging.

4.2 Materials and Methods

4.2.1 Protein Sample Preparation and Concentration Determination

The LV samples from 7 young (4-6 months) and 7 old (29-31 months) F344xBN rats were prepared for protein extraction. The masses of each animal and their tissue masses were recorded for analysis. Dry ice is prepared to transport tissue samples from a -80°C freezer to the lab. A box of ice is prepared to place prepared sample solutions. Small eppendorf tubes were also prepared to aliquot the preparation. An empty plastic test tube was massed, while a small weighing boat was used on top of a Styrofoam container with dry ice. The frozen sample was placed on top of the weighing boat and cut with a razor blade. The cut sample is placed inside a test tube, and the tube and sample were weighed. The mass of the tube was subtracted to determine the mass of the sample. This procedure was repeated until a desired mass of sample was achieved, and the stock tissue samples were returned to the –80°C freezer. The cut samples were kept on dry ice.

The extraction buffer (EB) was then added (0.9 ml) to each sample and the homogenizer mixer was cleaned and prepared to grind the tissue. After the grinder was inserted into the tube held in an ice container, the unit was turned on and mixed once to soften hard sample then 3X for 5 sec periods. Once the finished solution was returned to ice and the grinder head cleaned, warmed SDS is then added in order to create a 2% SDS solution: The samples were vortexed and kept on ice for 10-20 minutes. The tubes were centrifuged in 4°C at 1000 G for 15-20 min. After the supernatant was removed and placed in eppendorf tubes on ice, the remaining pellets were centrifuged at 10,000 G for 10 minutes. The supernatant was then added to the previous supernatant, the sample aliquoted into eppendorf tubes (100-200 μl), and the aliquots stored in –80°C freezer. The protein concentration of each sample was determined in an automated fluorometer microplate reader (Spectramax, Molecular Devices). Based on the concentration of each protein sample, a certain amount of H_2O and 2% SDS dye was added to make a fixed concentration for all samples (e.g. concentration of 1μg/μl). This was done in order to compare the same amount of protein for each sample.

4.2.2 Gel Electrophoresis

4.2.2.1 Gel Preparation. The tissue sample's proteins were separated according to their molecular weights on polyacrylamide gels. Gel solutions were prepared for each protein of interest in an assembled glass plate apparatus (BioRad) (Figure 4.1) and were prepared according to the recipes given in Table 4.1 in the order shown in Table 4.2.

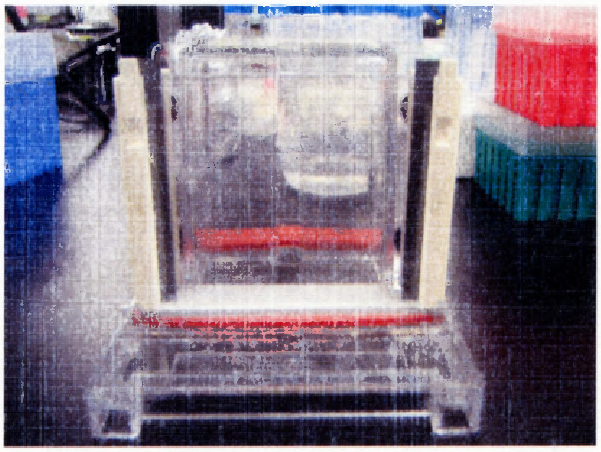

Figure 4.1 Assembled BioRad glass plate apparatus for gel preperation.

The gel concentration was determined by the amount of acrylamide mix added with respect to the total volume and the polymerization rate controlled by the amount of TEMED and persulfate in the solution. A resolving gel (4.5 ml) was first poured into the gel plate apparatus while a thin layer of 0.1% SDS was added on top to create a seal from the air. Once the resolving gel polymerized, the 0.1% SDS layer was removed with blotting paper and the stacker gel added (2.5 ml). After pouring the stacker gel, the 15 well comb was quickly inserted and positioned. Once the stacker was polymerized the combs were gently removed and the wells rinsed with millipure water to make sure they were free of polyacrylamide. A stacker gel was not used in the case of 6% gels, which consisted only of a resolving gel solution (7 ml).

Table 4.1 Recipe For Preparing Resolving and Stacking Gel Solutions

Solutions for Preparing Resolving Gels for Tris-glycine SDS-Polyacrylamide Gel Electrophoresis

	Component volumes (ml) per gel mold volume of							
Solution components	**5 ml**	**10 ml**	**15 ml**	**20 ml**	**25 ml**	**30 ml**	**40 ml**	**50 ml**
6%								
H_2O	2.6	5.3	7.9	10.6	13.2	15.9	21.2	26.5
30% acrylamide mix	1.0	2.0	3.0	4.0	5.0	6.0	8.0	10.0
1.5 M Tris (pH 8.8)	1.3	2.5	3.8	5.0	6.3	7.5	10.0	12.5
10% SDS	0.05	0.1	0.15	0.2	0.25	0.3	0.4	0.5
10% ammonium persulfate	0.05	0.1	0.15	0.2	0.25	0.3	0.4	0.5
TEMED	0.004	0.008	0.012	0.016	0.02	0.024	0.032	0.04
8%								
H_2O	2.3	4.6	6.9	9.3	11.5	13.9	18.5	23.2
30% acrylamide mix	1.3	2.7	4.0	5.3	6.7	8.0	10.7	13.3
1.5 M Tris (pH 8.8)	1.3	2.5	3.8	5.0	6.3	7.5	10.0	12.5
10% SDS	0.05	0.1	0.15	0.2	0.25	0.3	0.4	0.5
10% ammonium persulfate	0.05	0.1	0.15	0.2	0.25	0.3	0.4	0.5
TEMED	0.003	0.006	0.009	0.012	0.015	0.018	0.024	0.03
10%								
H_2O	1.9	4.0	5.9	7.9	9.9	11.9	15.9	19.8
30% acrylamide mix	1.7	3.3	5.0	6.7	8.3	10.0	13.3	16.7
1.5 M Tris (pH 8.8)	1.3	2.5	3.8	5.0	6.3	7.5	10.0	12.5
10% SDS	0.05	0.1	0.15	0.2	0.25	0.3	0.4	0.5
10% ammonium persulfate	0.05	0.1	0.15	0.2	0.25	0.3	0.4	0.5
TEMED	0.002	0.004	0.006	0.008	0.01	0.012	0.016	0.02
12%								
H_2O	1.6	3.3	4.9	6.6	8.2	9.9	13.2	16.5
30% acrylamide mix	2.0	4.0	6.0	8.0	10.0	12.0	16.0	20.0
1.5 M Tris (pH 8.8)	1.3	2.5	3.8	5.0	6.3	7.5	10.0	12.5
10% SDS	0.05	0.1	0.15	0.2	0.25	0.3	0.4	0.5
10% ammonium persulfate	0.05	0.1	0.15	0.2	0.25	0.3	0.4	0.5
TEMED	0.002	0.004	0.006	0.008	0.01	0.012	0.016	0.02
15%								
H_2O	1.1	2.3	3.4	4.6	5.7	6.9	9.2	11.5
30% acrylamide mix	2.5	5.0	7.5	10.0	12.5	15.0	20.0	25.0
1.5 M Tris (pH 8.8)	1.3	2.5	3.8	5.0	6.3	7.5	10.0	12.5
10% SDS	0.05	0.1	0.15	0.2	0.25	0.3	0.4	0.5
10% ammonium persulfate	0.05	0.1	0.15	0.2	0.25	0.3	0.4	0.5
TEMED	0.002	0.004	0.006	0.008	0.01	0.012	0.016	0.02

Solutions for Preparing 5% Stacking Gels for Tris-glycine SDS-Polyacrylamide Gel Electrophoresis

	Component volumes (ml) per gel mold volume of							
Solution components	**1 ml**	**2 ml**	**3 ml**	**4 ml**	**5 ml**	**6 ml**	**8 ml**	**10 ml**
H_2O	0.68	1.4	2.1	2.7	3.4	4.1	5.5	6.8
30% acrylamide mix	0.17	0.33	0.5	0.67	0.83	1.0	1.3	1.7
1.0 M Tris (pH 6.8)	0.13	0.25	0.38	0.5	0.63	0.75	1.0	1.25
10% SDS	0.01	0.02	0.03	0.04	0.05	0.06	0.08	0.1
10% ammonium persulfate	0.01	0.02	0.03	0.04	0.05	0.06	0.08	0.1
TEMED	0.001	0.002	0.003	0.004	0.005	0.006	0.008	0.01

Tables are modified from Harlow and Lane (1988).

Table 4.2 Order in which Gel Ingredients were Added for Resolving & Stacking Gels

Step	Resolving Gel	Stacking Gel
1	Millipure H_2O	Millipure H_2O
2	30% acrylamide mix	30% acrylamide mix
3	1.5 M Tris (pH 8.8)	1.0 M Tris (pH 6.8)
4	10% SDS	10% SDS
5	TEMED	TEMED
6	10% ammonium persulfate	10% ammonium persulfate

Several different gel concentrations (Table 4.3) were used in these experiments depending on the type of protein investigated. In each case a specific amount of protein was loaded in each well (Table 4.3).

Table 4.3 Protein Gel Concentration and Amount of Protein Mass Loaded

Protein	**Gel Concentration**	**Protein Mass**
β1-Integrin	10%	20 μg
Vinculin	8%	10 μg
Talin	6%	10 μg
α-Actinin	8%	10 μg
Filamin-C	6%	30 μg
α-Tubulin	10%	10 μg
β-Tubulin	10%	20 μg
Desmin	10%	10 μg

4.2.2.2 Running Gel Apparatus. The gels were placed into a running chamber filled with 1X SDS running buffer (Figure 4.2). Protein samples were loaded into each well by starting with the molecular weight marker.

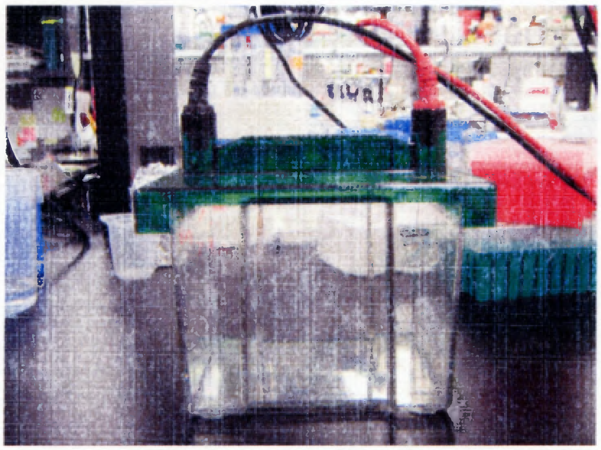

Figure 4.2 Photograph of the BioRad electrophoresis gel running chamber.

After the running chamber was filled with running buffer, the gel was run at a constant current (25 mA/gel), corresponding to a starting voltage of 100 V. The gel was then run until the protein sample dye solutions run out of the bottom of the gel (approximately 1 hr), or until the appropriate mass of sample entered the gel (i.e. 250 marker has entered the gel). Notice that the voltage increased with time as the resistance of the gel increased.

4.2.2.3 **Gel Transfer.** The gel was removed from the glass plates in the running chamber setup. The stacker gel and wells were removed, or in the case of a 6% gel only the wells were removed. A sandwich sitting in a plastic container was prepared in a transfer sandwich setup (Figure 4.3). The plastic container was filled with 1X Transfer Buffer. A BioRad transfer sandwich is placed in the container with the black side facing the bottom of the container. A Scotch Brite pad was placed in the sandwich followed by one sheet of blotting paper (Size: 2.5"x4" & Small Plate Size for 6% gels). One blotting paper was layed on the gel still attached to the glass plate and used to gently peel the gel off the glass. The blotting paper and gel were then placed on top of the other blotting paper. A nitocellulose membrane (Size: 2.5"x4" & Small Plate Size for 6% gels) was labeled in the upper right hand corner, wetted and then placed on top of the gel. The membrane was then rolled in order to remove air bubbles.

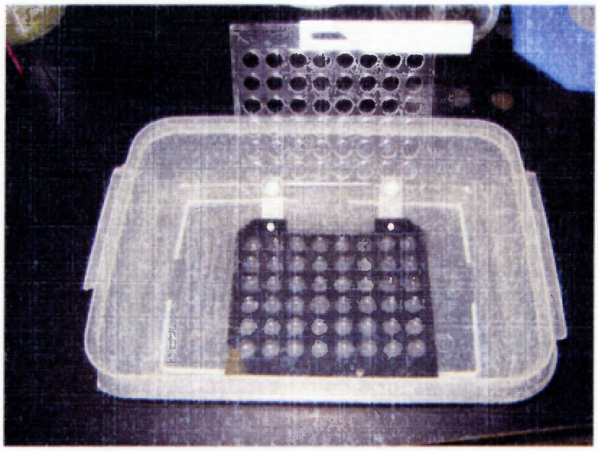

Figure 4.3 Gel transfer sandwich in a tupperware container.

The membrane had protein binding properties and binded proteins non-specifically (i.e. binded all proteins equally well). Protein binding was based upon hydrophobic interactions, as well as charged interactions between the membrane and the proteins. Two more blotting papers were placed on top along with a Scotch Brite pad, removing air from each layer by rolling. The sandwich was then closed, making sure that no air was introduced into the layers. The sandwich(s) were placed into the transfer apparatus (Figure 4.4) with the black face of the sandwich touching the black wall of the apparatus. A frozen pack was placed on one end and filled with transfer buffer covering the gel. The lid was connected (red to red, black to black) and the unit was run for 1 hr at the constant voltage of 100V in a container of ice. In some cases, the unit was run longer if the proteins needed a longer transfer time (90 minutes).

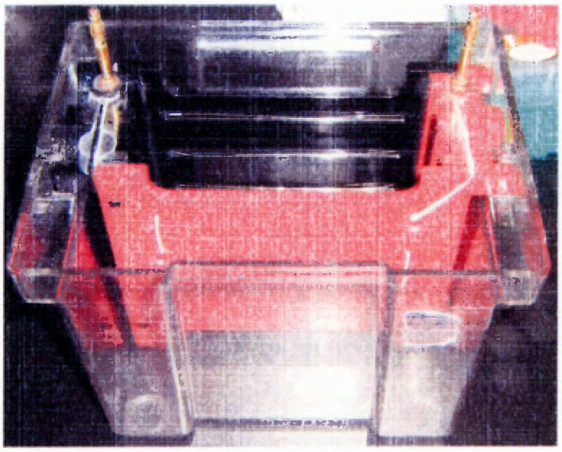

Figure 4.4 Photograph of the BioRad gel transfer apparatus.

4.2.2.4 Blocking. After the transfer time was complete, the sandwich was disassembled and the membrane carefully cut with scissors using the gel as a template. Gloves were worn when handling the gel and tweezers used to handle the membrane. The membrane was then washed in TBST to remove methanol, and the membrane blocked in order to prevent non-specific protein interactions between the membrane and the antibody protein. This was accomplished by placing the membrane in a solution of 5% non-fat dry milk in TBST for 30 minutes (in a plastic box on the rocking platform).

4.2.2.5 Probing with the Primary Antibody. The individual membranes were then probed for the protein of interest by exposing the membrane to the respective amount (e.g. 1:1000 (1μl of antibody in 1ml of solution) and type of antibody (Table 4.4). This primary antibody, which only recognizes the protein of interest, was incubated with the membrane. The antibody was diluted in a solution containing 5% milk typically prepared on ice. You typically need 1-2 ml of solution was typically needed to cover a plot. The diluted antibody solution and the membrane were sealed in a plastic bag and gently agitated for an overnight incubation at 4°C.

Table 4.4 Respective Protein Gel Concentration and Amount of Protein Mass Loaded

Protein	**1^{ry} Antibody Concentration**	**1^{ry} Antibody Type**	**2^{ry} Antibody**
β1-Integrin	1:1000	Becton Dickinson, 610468	mouse
Vinculin	1:1000	Sigma, V9133	mouse
Talin	1:1000	Sigma, T3287	mouse
α-Actinin	1:1000	Sigma, A5044	mouse
Filamin-C	1:1000	Abdellatif [20]	rabbit
α-Tubulin	1:1000	Sigma, T6199	mouse
β-Tubulin	1:1000	Sigma, T7816	mouse
Desmin	1:1000	Sigma, D8281	rabbit

4.2.2.6 Washing and Applying Secondary Antibody. The bag containing the membrane was opened, and the membrane placed in a plastic box and rinsed with TBST. The box was filled with TBST and rocked on the platform three times (First: 10 minutes, Second: 7 minutes, and Third: 7 minutes). TBST was removed and replenished after each wash. After the final wash the secondary antibody (type listed in Table 4.4) was added in 5% milk at a concentration of 1:5000, and allowed to rock at room temperature for 1 hour. The secondary antibody only recognizes the first antibody and was used for visual identification of where on the membrane the primary antibody had bound. Once the secondary antibody incubation period was complete, the milk was removed and the blot rinsed with TBST. The membrane was then rocked on the platform in TBST three times (First: 10 minutes, Second: 7 minutes, and Third: 7 minutes).

4.2.2.7 Photo Developing and Analysis. The membranes were then treated with developing solution to be transferred to photo paper. Three milliliters (ml) of reagent A developing solution and three ml of reagent B developing solution (Perkin Elmer Western Lightning) were added in separate corners of a plastic box. The membrane was dried on blotting paper and then placed into the mixed developing solution for one minute. After exposure to the developing solution the membrane was blotted dry and placed in a photo developing canister on blue photo paper covered with seran wrap. The membrane was then covered with seran wrap and the canister closed. In the dark room a piece of blue photo paper was inserted in the canister and the film exposed initially for one minute. The one-minute results were interpreted in the following manner: if they were too dark the photo paper was exposed for a shorter amount of time, and if they were too light it was exposed for a longer amount of time. The developed membrane was only good for roughly 20 minutes, at which point more developing solution would have to be used. Once a clear picture was seen the standard marker location was noted on the developed photo. The blots were then scanned and an image analysis software (Quantity One, BioRad) used to quantify the protein's band black levels, which correspond to the amount of protein present.

4.3 Results

4.3.1 Physiological Indices

The tissue samples collected from young F344xBN (n=7) and old F344xBN (n=7) were analyzed. A comparison was made between the LV mass (mg) and the animal body weight (BW) (g) and the LV mass (mg) and the Tibia length (TL) (cm), which are known indices of hypertrophy. An non-significant (NS) difference was seen in the LV to BW ratio, whereas a significant (*, $p<0.05$) 30.1% increase was obtained in the ratio of LV to TL with age (Figure 4.5).

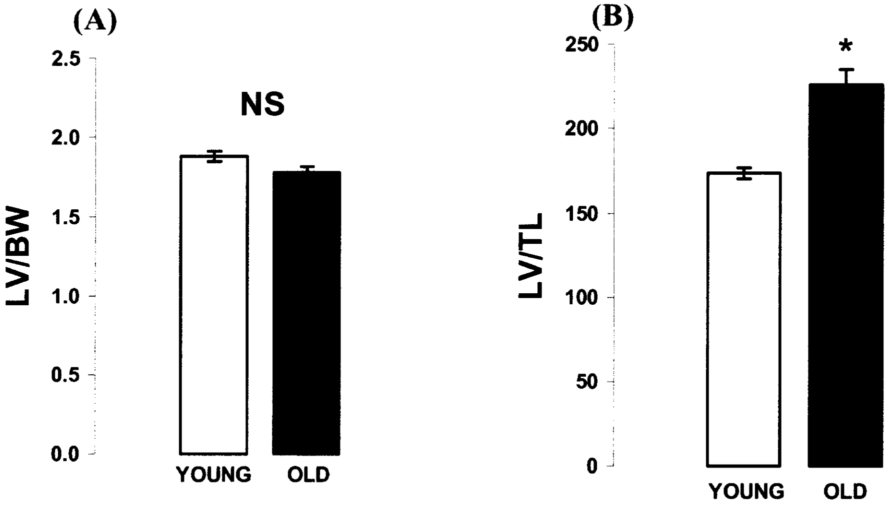

Figure 4.5 Comparison of (A)Ratio of LV/BW and (B) Ratio of LV/TL, between young and old animals.

4.3.2 Mechanotransduction Proteins

Figure 4.6 shows the β1-Integrin (MW 130 kDa) western blot where there is a significant (*, $p<0.05$) 63.7% increase in β1-Integrin's arbitrary density units (ADU) from young (n=7) to old (n=7) samples.

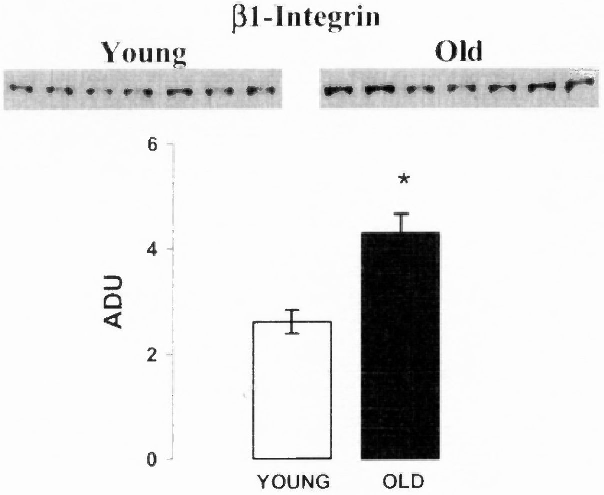

Figure 4.6 β1-Integrin Western blot and quantification in young and old animals.

Figure 4.7 shows the Vinculin (MW 116 kDa) western blot where there is a significant (*, p<0.05) 26.5% increase in Vinculin ADU from young (n=7) to old (n=7) samples.

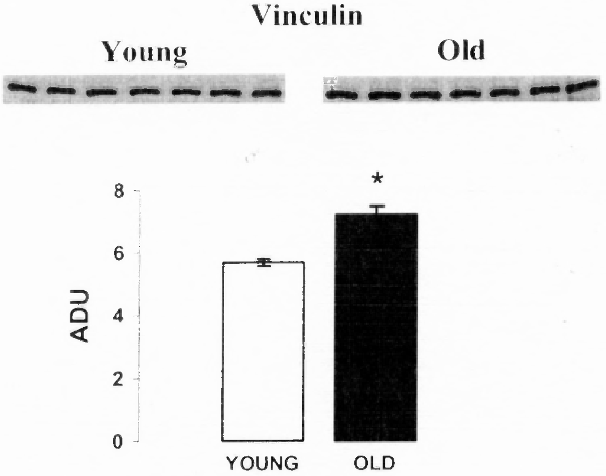

Figure 4.7 Vinculin Western blot and quantification in young and old animals.

Figure 4.8 shows the Talin (MW 215 kDa) western blot where there is no significant (NS, p>0.05) change in Talin ADU from young (n=7) to old (n=7) samples.

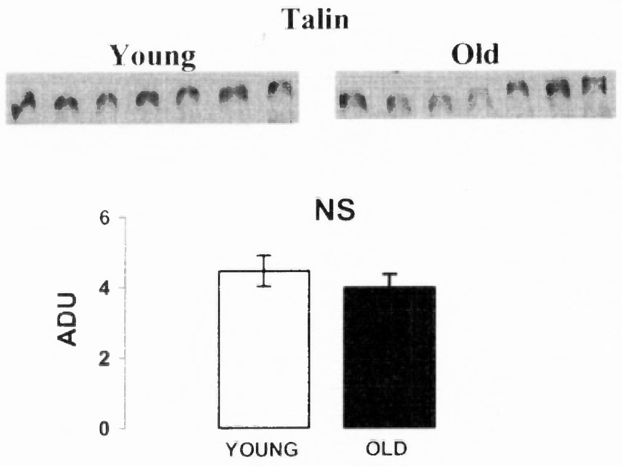

Figure 4.8 Talin Western blot and quantification in young and old animals.

Figure 4.9 shows the α-actinin (MW 100 kDa) western blot where there is no significant (NS, $p>0.05$) change α-actinin ADU from young (n=7) to old (n=7) samples.

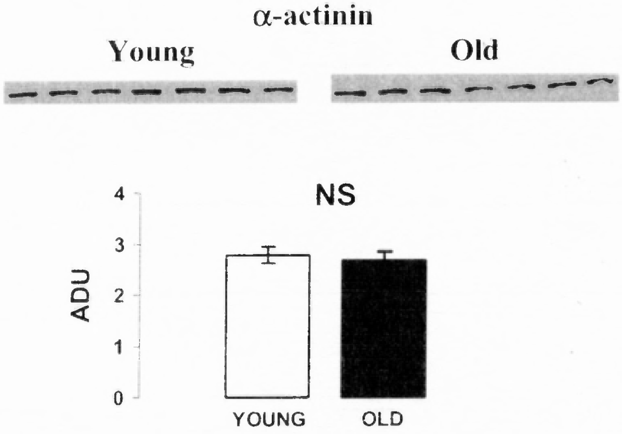

Figure 4.9 α-actinin Western blot and quantification in young and old animals.

Figure 4.10 shows the Filamin-C (MW 280 kDa) western blot where there is a significant (*, $p<0.05$) 74.2% increase in Filamin-C ADU from young (n=7) to old (n=7) samples.

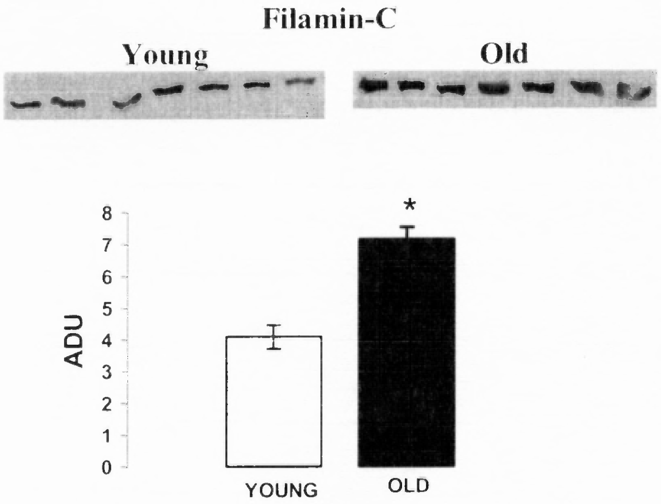

Figure 4.10 Filamin-C Western blot and quantification in young and old animals.

4.3.3 Cytoskeletal Proteins

Figure 4.11 shows the α-Tubulin (MW 50 kDa) Western blot where there is a significant (*, $p<0.05$) 2.3 fold increase in α-Tubulin ADU from young ($n=7$) to old ($n=7$) samples.

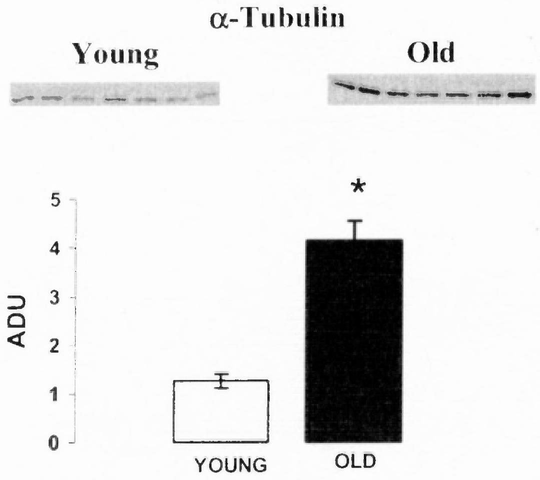

Figure 4.11 α-Tubulin Western blot and quantification in young and old animals.

Figure 4.12 shows the β-Tubulin (MW 55 kDa) Western blot where there is a significant (*, $p<0.05$) 1.7 fold increase in β-Tubulin ADU from young ($n=7$) to old ($n=7$) samples.

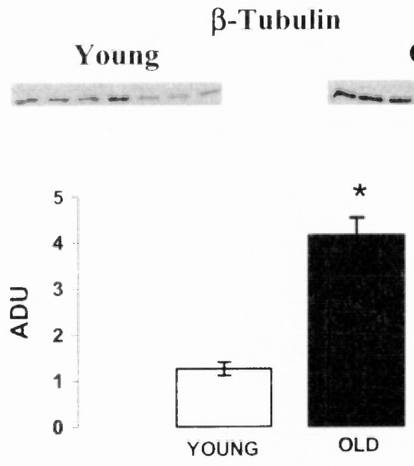

Figure 4.12 β-Tubulin Western blot and quantification in young and old animals.

Figure 4.13 shows the Desmin (MW 53 kDa) Western blot where there is a significant (*, $p<0.05$) 40.9% decrease in Desmin ADU from young ($n=7$) to old ($n=7$) samples.

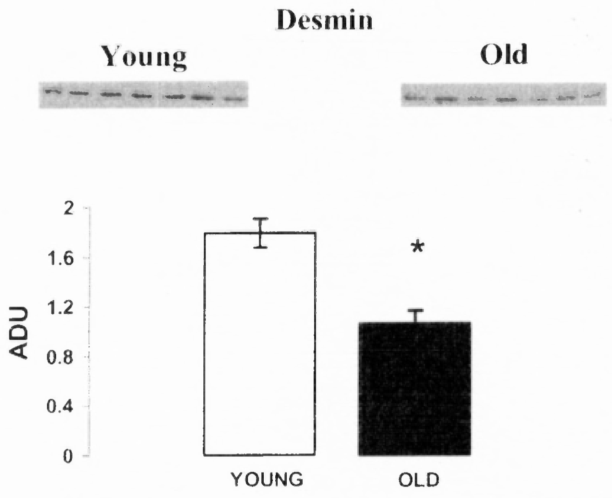

Figure 4.13 Desmin Western blot and quantification in young and old animals.

4.3.4 Summary

The relationship between LV tissue mass and rat body weight did not indicate the presence of hypertrophy. However, when the LV tissue mass was compared to the Tibia length, hypertrophy was observed with aging (Figure 4.4). Table 4.5 summarizes the cellular protein changes with aging.

Table 4.5 Summary of Cellular Protein Changes with Aging

Protein	Result
β1-Integrin	UpRegulated
Vinculin	Up Regulated
Talin	No Change
α-Actinin	No Change
Filamin-C	Up Regulated
α-Tubulin	Up Regulated
β-Tubulin	Up Regulated
Desmin	Down Regulated

Several key proteins linked to mechanotransduction were observed to be up regulated with aging. Moreover, the measurements presented above show that there are changes in cytoskeletal proteins, including up regulation in the microtubules and down regulation in the intermediate filament Desmin.

CHAPTER 5

PHYSIOLOGY MEASURES IN CONCIOUS RATS

5.1 Introduction

This chapter discusses the development of an instrumentation technique to measure LV pressure and dimension in a conscious rat, while applying interventions (drug delivery, occlusions). This method will be used to determine the effects of aging induced cellular changes on global cardiac function in the aging rat model.

5.2 Materials and Methods

5.2.1 Instrumentation for Implantation

Standard instrumentation consists of the following instruments placed through a left intercostal thoracotomy (Figure 5.1). The pressure is measured by using a solid-state pressure transducer (Konigsberg P1.5) A solid-state micromanometer (Konigsberg P1.5) is placed in the left ventricle and the left ventricle short axis dimension is measured by using a pair of piezoelectric crystals. One crystal is excited by an electrical signal and oscillates sending out sound wave (pinger) while the other crystal receives the sound wave. The time that the sound travels from the pinger to the receiver is measured. The distance is calculated by multiplying this time by the speed of sound in water (1.54 mm/μsec).

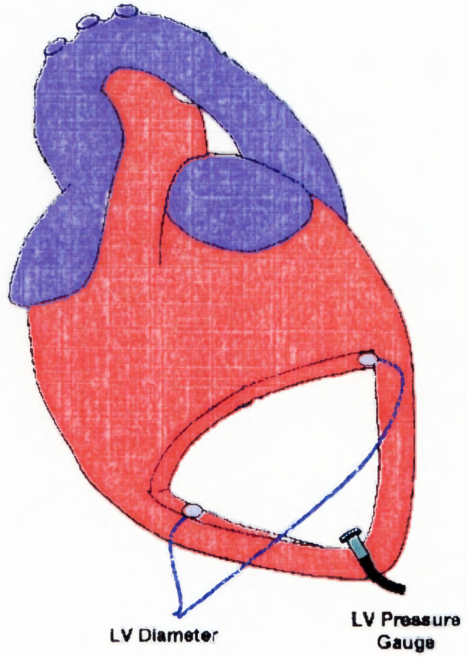

Figure 5.1 Instrumentation used to measure LV pressure and dimesion.

The volume of the LV can be determined by approximating the LV as a sphere and calculating the volume (V) with the short axis dimension (d) (Equation 5.1).

$$V = \frac{\pi \cdot d^3}{6} \tag{5.1}$$

A Braintree Micro-Renathane (MR) tubing catheter (7 inch length) was placed in venous for drug injection, while a Braintree Rena Pulse (RP) tubing catheter (8 inch length) was placed in the ascending aorta for aortic pressure (AOP) measurement. LV filling, in the conscious closed chest model, was altered by Inferior Ven Caval Occlusions (IVCO) by using an embolectomy balloon catheter (Model-120502F, Edwards Life Sciences with diameter 2 French—OD (0.64mm & ID 0.30-0.34mm) inserted femorally. The inferior vena cava (IFC) was occluded, in the open chest case, with a 3-0 silk snare followed by LV volume overload with saline (20% of blood volume). IVCO was performed with a suture in the open chest case. During recovery from surgery, the animals were kept warm and continuously monitored in a thermal care unit (31°C, 30-50% humidity, and low flow O_2). Physiology experiments were conducted 7 days after surgery to provide recovery time.

5.2.2 Electronics Setup and Calibration

5.2.2.1 General Setup. The implanted instrumentation was connected to an amplifier electronic filter setup as shown in Figure 5.2. All the data were displayed on an oscilloscope, recorded on tape, and recorded on a computer through a data acquisition system (Notocord) with a 1000 Hz sampling rate. The Konigsberg LV pressure signal was filtered with a 1000 Hz low pass filter, and the AOP signal with a 60 Hz low pass filter. Basic physiology measures were deduced by configuring toolboxes in Notocord. These include the rate of pressure generation (dP/dt, determined with 1msec of smoothing)), heart rate, systolic and diastolic pressures, and maximum and minimum dimensions. A further analysis of the pressure volume relationship (PV loops) was performed with a custom designed software written in the MatLab programming language based on established physiological relationships [156-159].

Figure 5.2 Electronic setup consisting of pressure transducer amplifier, dimension crystal amplifier, and electronic filter.

5.2.2.2 Konigsberg Calibration. The P1.5 was calibrated before placing it into the animal with a manometer and fluid tank system (Figure 5.3A) filled with 300 ml of water maintained at 37°C (Figure 5.3B). The pressure amplifier's offset and gain were adjusted so that the ambient pressure (0 mm Hg) corresponded to 0 Volt and the maximum applied pressure of 200 mm Hg corresponded to the maximum voltage of 1 Volt. The gain and offset knobs were then locked into position, as shown in Figure 5.4, to preserve calibration until experimentation.

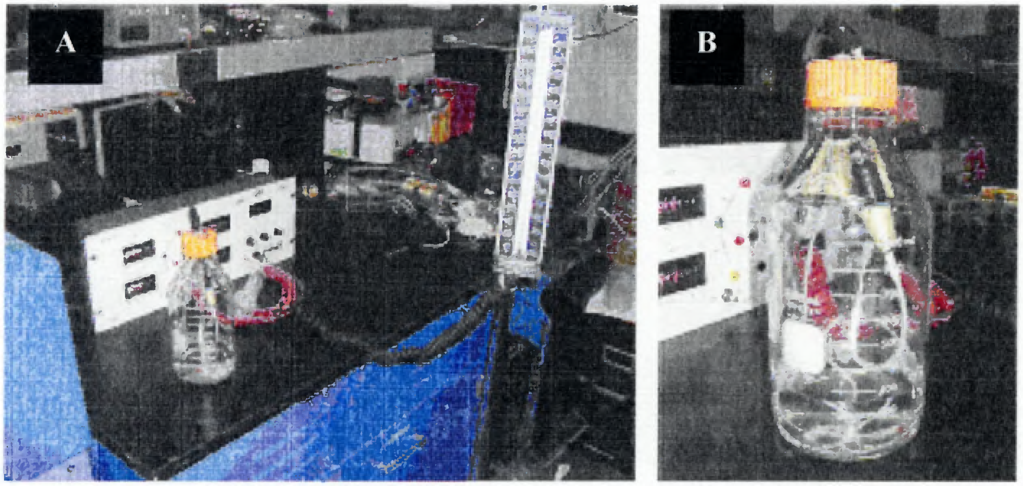

Figure 5.3 Photographs of (A) Manometer and Konigsberg calibration setup (B) pressure vessel used to apply pressure to the Konigsberg.

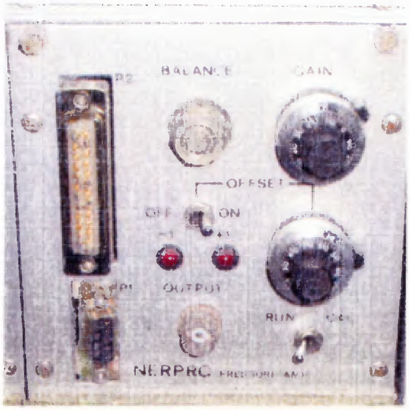

Figure 5.4 Photograph of the pressure amplifier with lockable gain and offset knobs.

The Konigsberg's sensitivity was checked by applying 25%, 50%, 75%, and 100% of the total pressure (200 mm Hg) with the calibration setup shown in Figure 5.3. The relationship between the applied and measured pressure should be linear to indicate a properly working transducer, as verified in Figure 5.5.

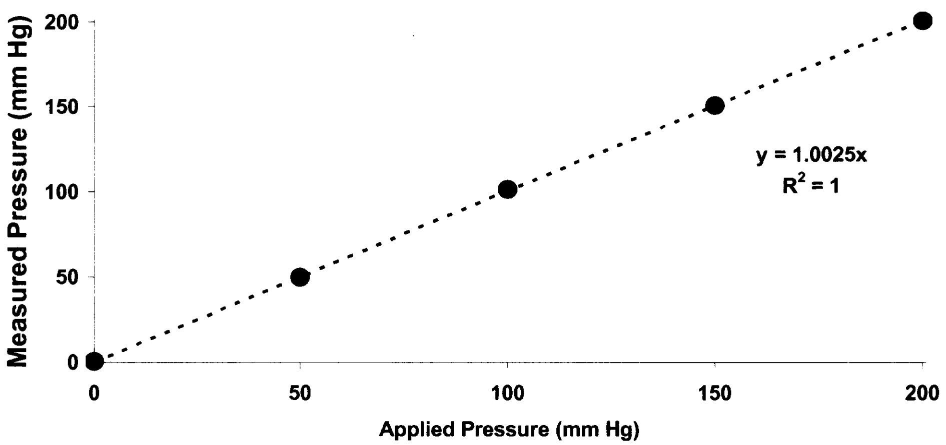

Figure 5.5 Konigsberg's sensitivity plot of measured pressure versus applied pressure indicating the linearity of the transducer.

The Konigsberg was sent for low temperature Gas ETO sterilization. High temperature sterilization requires the use of a vacuum which disrupts the offset's calibration. The gain decreases approximately by 1-2% per year. The gain value, for all intents and purposes, should never change during the experiment. The offset can vary over time due to the baseline drift (as much as 15 mm Hg/month). The AOP measured with a fluid catheter was used to calibrate the Konigsberg offset where the LVP systolic pressure was matched with the AOP systolic pressure on the day of experimentation (example shown in Figure 5.6). The AOP fluid catheter was connected to a Becton Dickinson Pressure Transducer, and calibrated with a manometer.

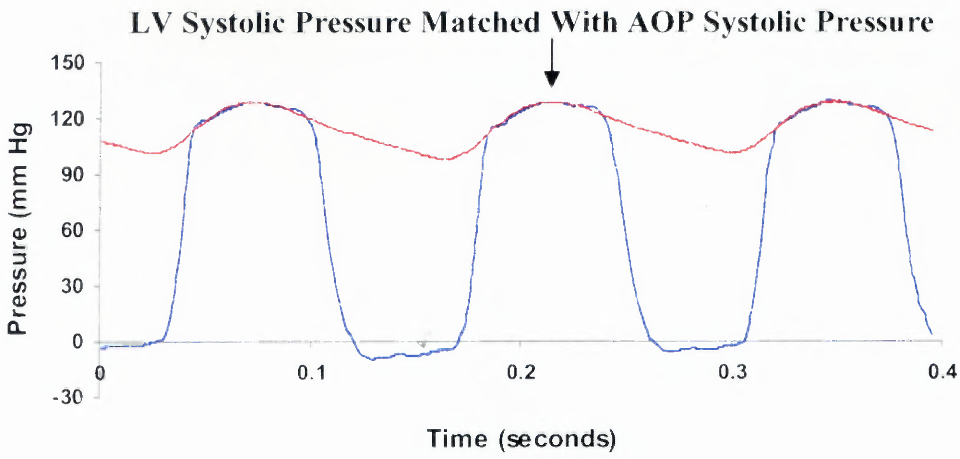

Figure 5.6 Konigsberg offset adjusted to match the LV systolic pressure with the AOP systolic pressure.

5.2.2.3 Dimension Crystal Calibration and Operation. The LV short axis dimension was measured by using a pair of piezoelectric crystals connected to their amplifier unit (Figure 5.7).

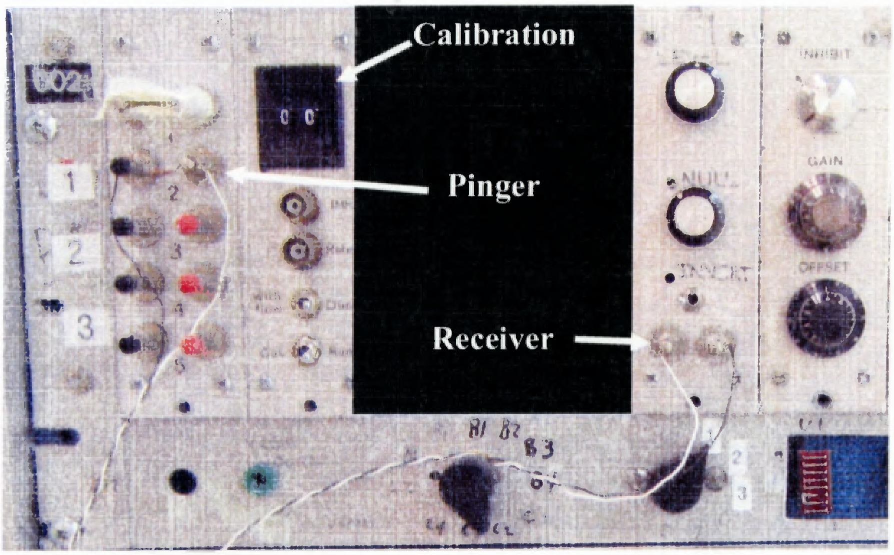

Figure 5.7 Photograph of the piezoelectric crystal dimension amplifier.

The pinger crystal was excited by an electrical signal coming from the pinger connection on the amplifier. The pinger oscillates, sending out a sound wave, which is received by the other crystal (receiver) attached to its respective amplifier connection. The signals are triggered by manipulating the null and inhibit levels on the amplifier (Figure 5.7). This method measures the time it takes for one crystal to send a sound wave and the other crystal to receive that signal. Therefore, the voltage signal measured is converted first into time with the amplifier's calibration (Figure 5.7) and then to distance by multiplying this time by the sound wave's speed. The amplifier calibration dial indicates time in microseconds. Therefore, setting the dial to 2 would send a voltage corresponding to a time of 2 μsec. Several voltages were used in order to calibrate the crystals.

5.2.2.4 Experimentation. Upon arrival from the vendor, the rat is trained to enter the conscious study restraining box (RB). A week after its arrival, the rat undergoes a surgery through which the Konigsberg and dimension crystal are implanted. The animal is allowed to recover for one week, during which time the rat continues to be trained to enter the RB. After one week, the MR and RPT are inserted into the animal. The animal then recovers for three days before experimentation. During this time, both catheters are heparinized first by flushing the line thoroughly with saline (2cc) and then by filling each catheter with heparin (.1cc) before closure. This procedure was conducted in order to prevent the lines from clogging. The rest of the procedure is as follows. On the third day, the Konisberg's offset drift is adjusted with the AOP systolic pressure, and baseline physiological measures are recorded. After the baseline levels are recorded, the drug is delivered bolus through the MR catheter according to the concentrations (mass of drug/mass of animal) listed in Table 5.1.

Table 5.1 Drug Concentrations for Physiology Experiments

Isoproteranol (ISO) Concentrations (μg/kg)			
0.05	0.1	0.2	0.4

Dobutamine (DOB) Concentrations (μg/kg)			
2.5	5	10	20

The animal is then allowed to recover back to its baseline condition before the next drug concentration is applied. At the end of testing cathers are heparanized and the rat is returned to its cage. The following day the embolectomy catheter is inserted in order to perform IVC occlusions later that same day. Open chest procedures involve no drug experimentation. The animal is anesthesized with pentobarbital (50 mg/kg) and IVC occlusions are performed with a snare technique following loading the LV with 20% of the animals total blood volume (50ml/kg).

5.3 Results

5.3.1 Baseline Signals

The solid state transducer produced clean signals (Figure 5.8) and reasonable values for Left Ventricular Systolic Pressure (Fig 5.8 (a) ~120 mm Hg), Short Axis Dimension (Fig 5.8 (b) 6.5-8.5 mm) and the maximal rate of pressure generation (dP/dtmax) (Figure 5.8 (c) ~10000 mm Hg/sec).

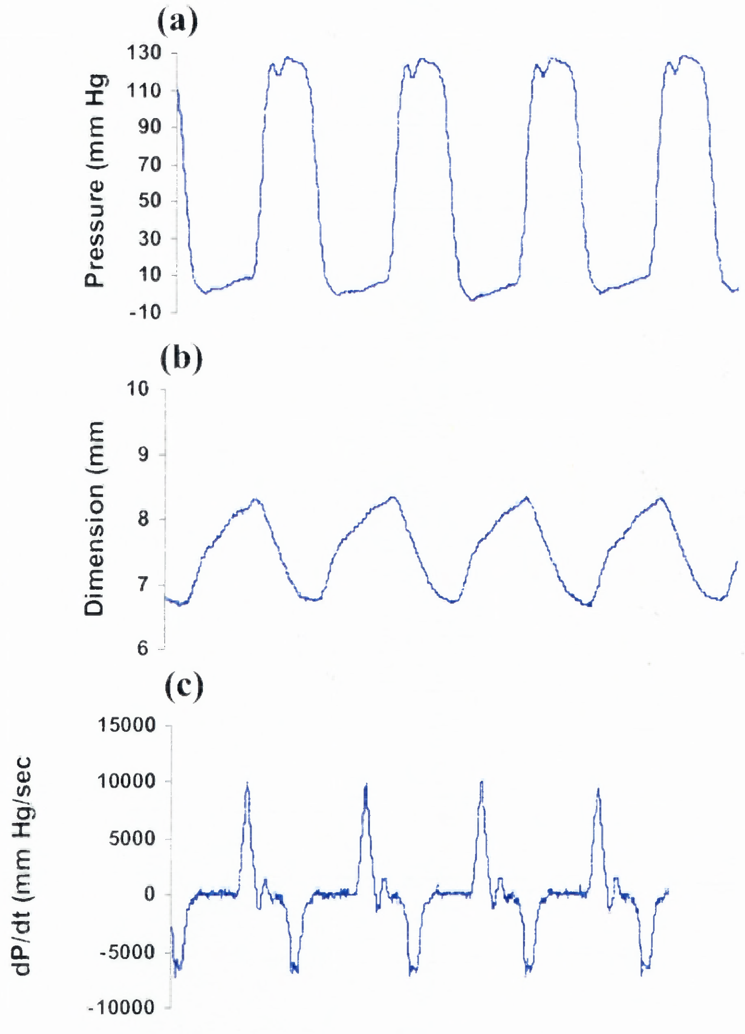

Figure 5.8 (a) Left Ventricular Pressure (LVP), (b) Left Ventricle Short Axis dimension, and (c) rate of pressure generation (dP/dt).crystal dimension amplifier.

5.3.2 Konigsberg Measures on Anesthetized and Conscious Animals

A comparison was made between an anesthetized (A)(n=3) and a conscious (C) (n=3) group of rats with the prototype Konigsberg. The results indicate that there is no significant difference between the LV End Systolic Pressure (LVESP) and the LV End Diastolic Pressure (LVEDP) (Figure 5.9).

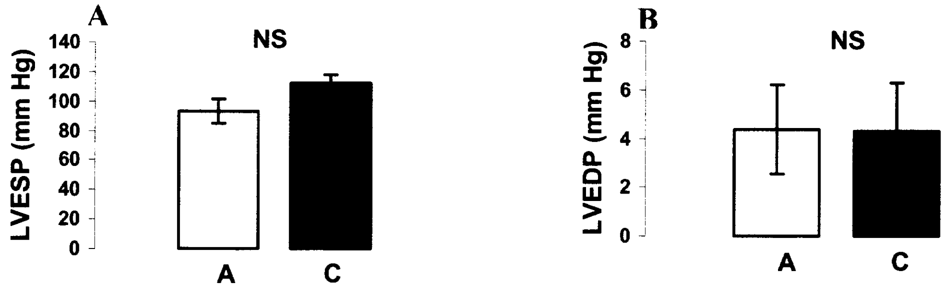

Figure 5.9 There is no significant (NS) difference in LVESP (A) and LVEDP (B) measured in anesthetized (A) and conscious (C) rats.

The rate of pressure generation (dP/dt) shows a significant (*, $p<0.05$) 40.5% increase in + dP/dt and 49.7% increase in –dP/dt from the anesthetized group (A) and the conscious(C) groups (Figure 5.10)

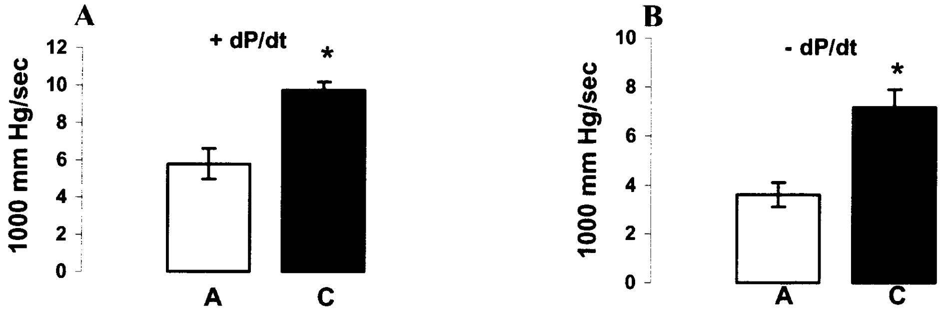

Figure 5.10 Significant (*, $p<0.05$) difference in +dP/dt (A) and –dP/dt (B) measured in anesthetized (A) and conscious (C) rats.

The heart rate (HR) shows a significant (*, $p<0.05$) 36.8% increase from the anesthesized (A) to conscious(C) groups (Figure 5.10 A). There is also a significant (*, $p<0.05$) 142.1% decrease in the isovolumic time constant for relaxation (τ, msec) from the anesthesized (A) to conscious(C) groups (Figure 5.11 B).

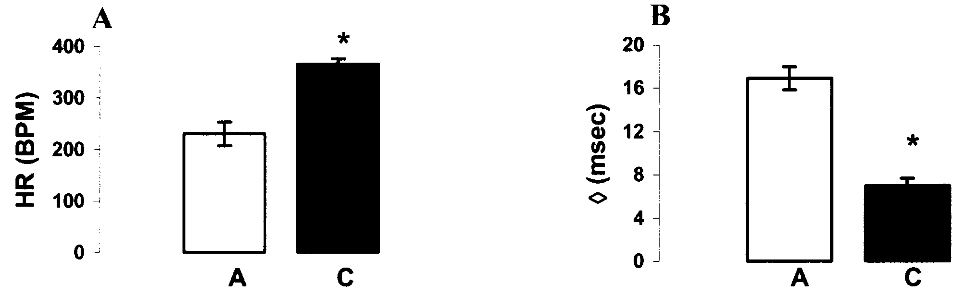

Figure 5.11 Significant (*, $p<0.05$) difference in HR (A) and τ (B) measured in anesthetized (A) and conscious (C) rats.

5.3.3 Comparison of Anesthetized to Conscious PV Loop

The occlusions conducted in both anesthetized open chest (Figure 5.12 (a)) and closed chest conscious (Figure 5.12 (b)) animals; show a significant reduction in pressure (20 mm Hg), allowing LV pressure volume relationships to be determined. The End Systolic Pressure Volume Relationship (ESPVR) and Pressure Recruitable Stroke Work (PRSW) could be measured in both cases, but only the open chest method allowed the End Diastolic Pressure Volume Relationship (EDPVR) to be measured, because intra-thoracic pressure affected EDP in the closed chest case (Table 5.2).

Table 5.2 Pressure Volume (PV) Measures between Anesthetized and Conscious Rats

	Anesthesized	**Concious**
ESPVR	0.60	0.75
PRSW	90.1	99.3
EDPVR	0.18	Not Applicable

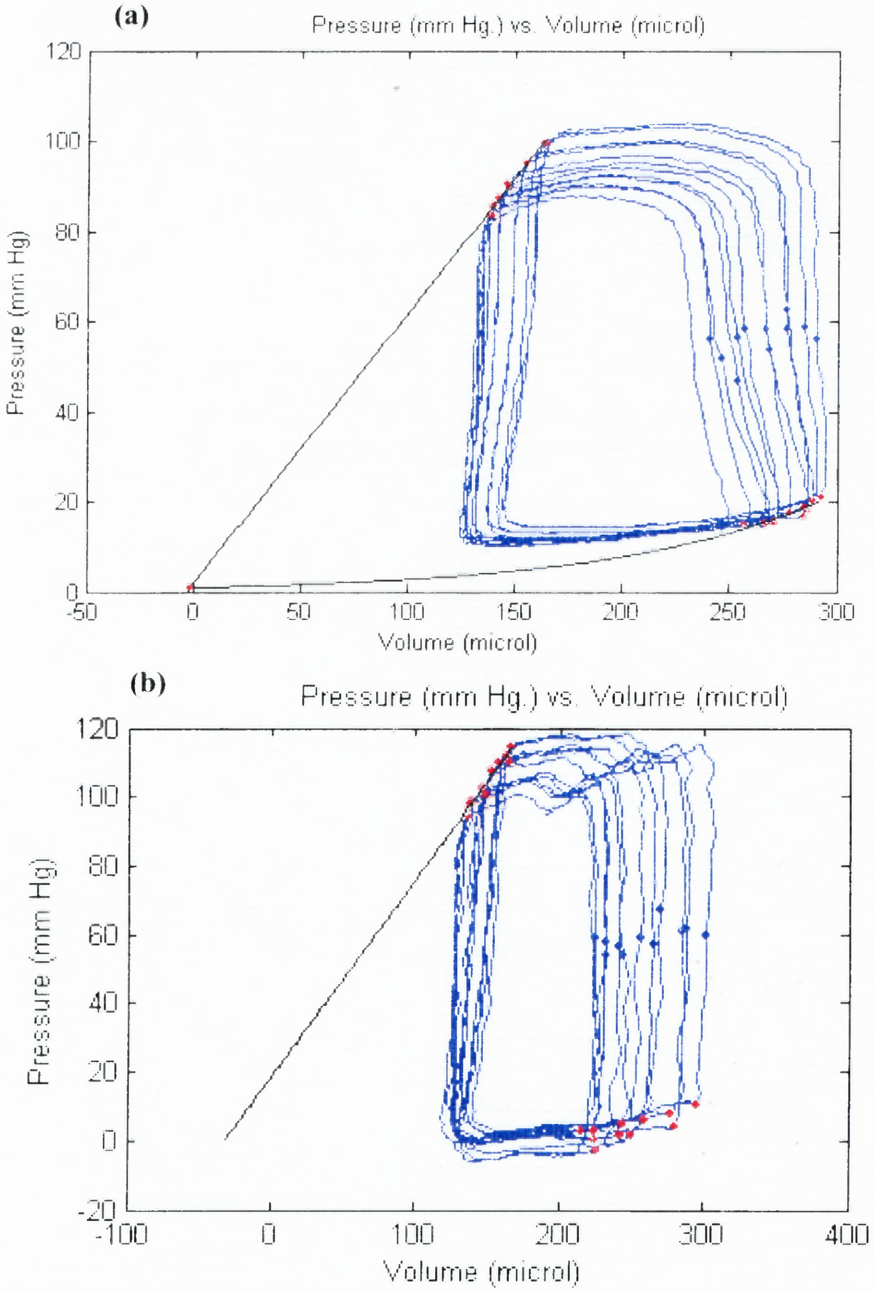

Figure 5.12 PV loops generated from (a) open chest preparation (b) conscious condition.

5.3.4 Conscious Measure of Drug Response

A major advantage of a conscious measure of cardiac physiology allows the effect of drugs to be measured without the influence of anesthesia. Aging is known to have an effect on the β adrenergic receptors in both the heart and vessels. The effect of isoproterenol (ISO) which affects the β_1 and β_2 receptors, as well as dobutamine (DOB) which affects the β_1 receptors, was tested on young (n=3) and old (n=1) F344xBN rats. The ISO effect on the contractility index (dP/dt) was seen in each animal (example shown in Figure 5.13).

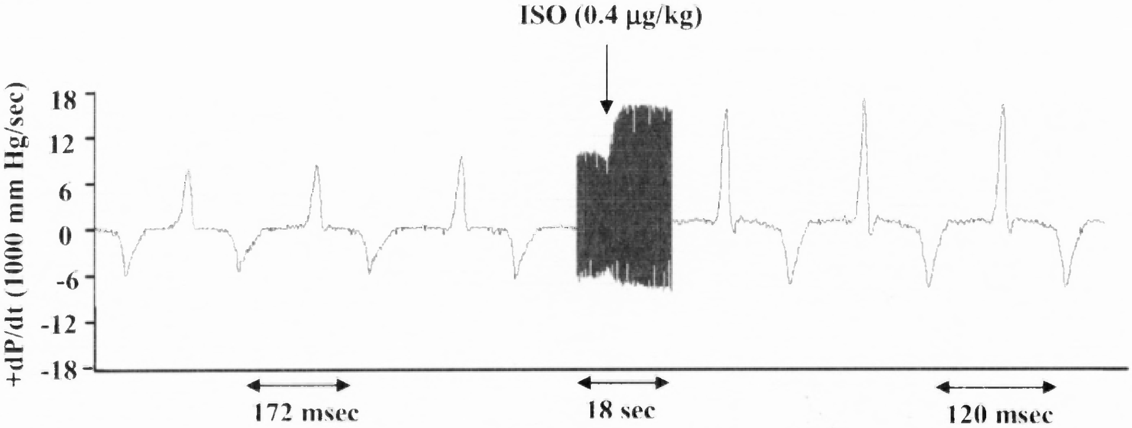

Figure 5.13 Isoproterenol effect seen on the contractility index (dP/dt) of rats.

While there was a response to high doses of ISO on the young rats, that effect was not found to be as dramatic on old rats (Figure 5.14).

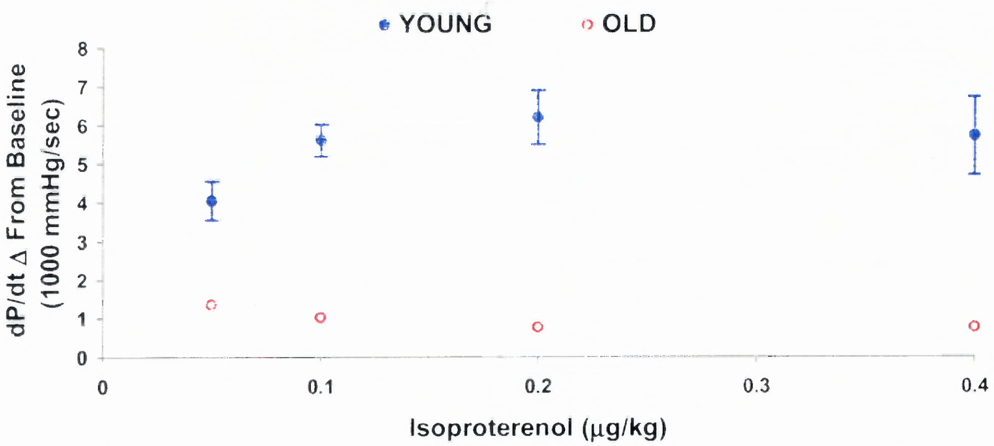

Figure 5.14 Effect of Isoproterenol dose on the contractility index (dP/dt) of young and old F344xBN rats.

The DOB effect on the contractility index (dP/dt) was studied in each animal (example shown in Figure 5.15).

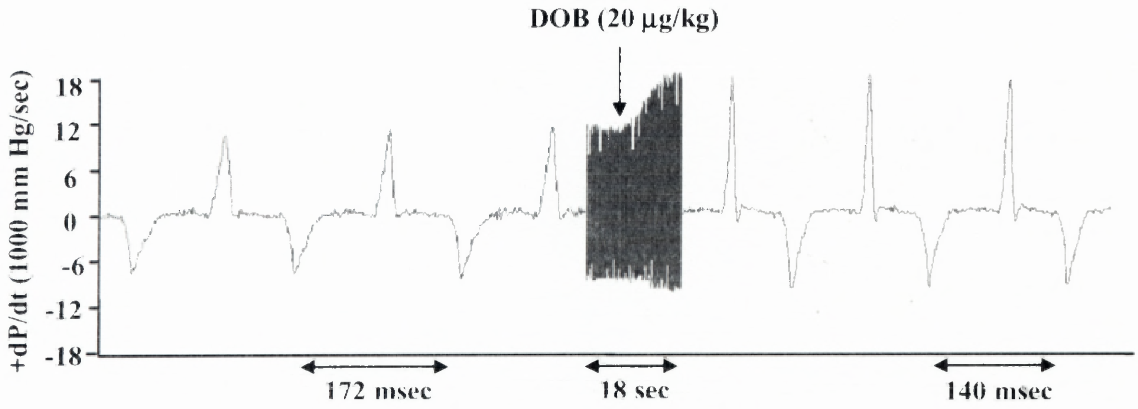

Figure 5.15 Dobutamine effect on the contractility index (dP/dt) of rats.

There was a response to high doses of DOB in the young rats but that effect was less pronounced in the old rats (Figure 5.16).

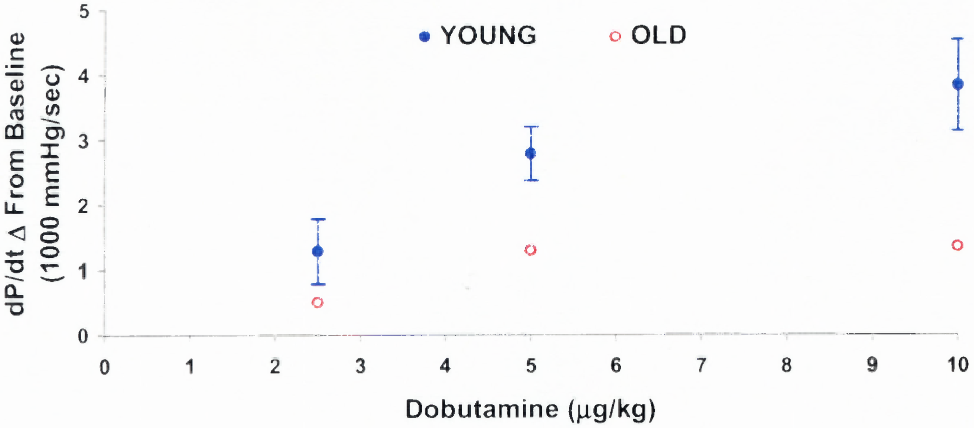

Figure 5.16 Effect of dobutamine dose on the contractility index (dP/dt) of young and old F344xBN rats.

CHAPTER 6

DISCUSSION AND CONCLUSION

Most studies on aging have demonstrated LV diastolic dysfunction [45]. The implications from these studies is that the mechanical dysfunction observed with aging is due to changes in the extracellular matrix, which could be attributed to increases in collagen [50]. The underlying hypothesis of the current investigation was that mechanical changes in the myocytes could participate in the LV diastolic dysfunction due to aging. Moreover, the current study was conducted in LV myocytes from male hearts, since aging-induced LV diastolic dysfunction is more pronounced in males than in females [45, 160]. The male F344xBN rat model is an accepted animal model of cardiac aging [146] and the results presented in this thesis showed that the increase in cell size (Table 2.2) and decrease in isolated myocyte contraction-relaxation data (Figure 2.4) are consistent with results of previous studies in other aging male rat strains [6, 50, 161, 162], which have been conducted previously in male animals.

To test the hypothesis that the material properties of cardiac myocytes change with aging in the rat model, indentation tests were performed with an AFM, which has been used to measure the viscoelastic response of different cell types (e.g. endothelial, platelets) with typical cellular apparent elastic modulus values between 1 kPa and 200 kPa, as previously described [131, 150]. The AFM technique has been well documented in its ability to measure cytoskeleton components [131]. A Finite Element Model (FEM) of AFM indentation was conducted using the ABAQUS software to investigate the use of CIST to analyze nano-indentation of known hyperelastic materials, specifically Mooney-Rivlin (MR) and Polynomial (POLY) materials. The numerically obtained AFM probe sample interaction in the MR (Figure 3.5) and POLY (Figure 3.6) materials compared well with typical Force-Indentation relationships observed in AFM indentation experiments. The FEM showed that boundary forces do not effect measurements where the maximum reaction force on the bottom surface is significantly smaller (MR: ~800 million times, & POLY ~462 million times) than the force needed to indent the material. Furthermore, the elastic modulus determined from the CIST fitting compared well to that calculated using Green's equation [123] based on the shear strain coefficients (MR Figure 3.7, POLY Figure 3.8). These data confirmed that the interpretation of AFM nanoindentation results with CIST could indeed determine the material properties of a sample.

The AFM indentation measurement registered changes in the myocyte sarcolemma, sarcomeric skeleton, and general cytoskeleton proteins (tubulin, desmin, and actin). The force indentation graph (Figure 2.6a) conducted on a myocyte compared favorably with previously published theoretical and experimental curves for biological cell material [123, 150]. For the same indentation depth, the cantilever deflection was greater on old F344xBN myocytes than on the young F344xBN myocytes, indicating that on average a larger force is necessary to indent the myocyte surface of old F344xBN rats as compared to that of young F344xBN rats (Figure 2.6a). Therefore, before even deriving a measure of the stiffness (apparent elastic modulus) from the force-indentation relationship, the stiffness of aged cardiac myocytes was shown qualitatively to be greater than young ones. The force indentation data fitted CIST well, with the AFM probe modeled as a blunted conical indenter (Figure 2.6b).

The results of the investigation reported here demonstrated that the apparent elastic modulus of isolated cardiac myocytes increases significantly ($p<0.01$) with advanced age (Figure 2.7). This increase was found to be approximately 21% from 35.1 ± 0.7 kPa ($n=53$) to 42.5 ± 1.0 kPa ($n=58$). The apparent elastic modulus (E) was determined by analyzing the relationship between the AFM indentation force and depth by means of the accepted and widely used CIST approach, and modeling the AFM probe as a blunted conical indenter, the latter having been shown to be an accurate representation of the AFM probe shape [123, 150]. Cardiac myocytes behave in a viscoelastic manner and when they are indented by the AFM tip, energy is dissipated into the cell (hysteresis). In order to accurately determine the apparent elastic modulus of the myocyte, the energy dissipated into the cell was minimized by selecting a tip speed (0.6 μm/sec) above which hysteresis remained essentially constant (Figure 2.2) while also maximizing the number of force curves that could be captured. Since minimal hysteresis is still present, the measurements do not reflect a purely elastic modulus but rather an apparent elastic modulus, which takes into account the viscoelastic nature of the myocyte. Analysis of the effects of age on normalized hysteresis show a significant 10% decrease in the energy dissipated into the myocyte cell with aging. A decrease in the energy dissipated by the cell implies that the viscous component of the cell's mechanical properties decreases with aging.

The apparent elastic modulus determined for young cardiac myocytes using AFM nanoindentation are in accord with data derived from studies in isolated rat cardiocytes using a variety of other techniques. However, no previous measurements are available in the literature for old cardiac myocytes to compare with our data. The apparent elastic modulus value of 35.1 ± 0.7 kPa (n=53) on young (4 mos old) cardiac myocytes compares favorably with Granzier's stiffness value (32 kPa) obtained by studying the stress versus strain relationship on skinned rodent cardiocytes by attaching glass micro-needles with urethane foam and applying a tensile force [163, 164]. It is also in good agreement with Brady's stiffness measure (26 kPa) found in skinned rodent cardiocytes held between double micropipettes by suction and barnacle cement [165]. Differences in the measured value between the data reported here and previously published results could be attributed to the fact that in this work the measured myocytes were not skinned, thus still having their membrane, in contrast to other works. The removal of the cell membrane could indeed have an effect on cardiac myocyte viscoelasticity. The measurement technique itself could also affect viscoelasticity values, since the measurements described above were carried out in the transverse direction, contrarily to other studies in which measurements were performed in the tangential direction (through the application of a tensile force).

Moreover, the myocytes studied by AFM were not electrically stimulated to contract and therefore remained essentially motionless during nanoindentation. However, the myocytes could not be considered completely passive because of the effect of cross bridge cycling. The variation in stiffness with location prevalent for other cell types (e.g. embryonic cardiocytes) measured with the AFM was negligible with adult mammalian cardiac myocytes (see also [150]. It is worth also noting that the boundary effects that are known to influence the results of AFM indentation on smaller cells are not relevant in this experimental design, because of the AFM probe's nano-size which remains much smaller than the myocyte's micro-size. Therefore, boundary effects such as the interaction between the myocytes laminin-receptors and the laminin-coated-substrate, as well as the material properties of the substrate itself, do not affect the indentation measurements. AFM indentation may also affect the material properties of the cell; however, experiments proved that replicate indentation in one cellular location does not significantly change the apparent elastic modulus (Figure 2.8a) as has also been shown by others [150]. AFM measurements were conducted within a six-hour period from the time of isolation. The variation in the time at which AFM measurements were conducted could affect the apparent elastic modulus measured; however, the experiments proved that this was not the case in both young and old myocytes by displaying similar data from the AFM over a six-hour period (Figure 2.8b). It is also possible that the size of the cell, per se, may have an influence on the apparent elastic modulus measurements. This point is particularly important to consider here, since aging indeed causes myocyte hypertrophy [50], as demonstrated in the current study. However, the apparent elastic modulus is a material property reflecting the extent to which cardiac myocytes deform under a stress and should thus be independent of the cell's geometry, a property indeed verified experimentally in Figure 2.5. Nonetheless, the age related increase in the myocyte apparent elastic modulus could be a result of hypertrophy [49]; however, as noted by Lakatta [67], aging induced hypertrophy is different from hypertrophy produced by pressure overload. In fact, Lakatta found that a portion of the mechanical property alterations seen in the aged heart is due to the underlying hypertrophy; however, the hypertrophy resulting from the mechanical loading of the LV cannot explain all the changes resulting from aging [166]. In any case, this point would not impact the conclusions of the current study that material properties of myocytes become altered with aging and that such changes could contribute to the altered properties of the aging heart.

Cellular material property changes were analyzed with established immunoblot (western blot) techniques. Proteins involved in the process of mechanotransduction were measured along with cytoskeletal proteins involved in the cell's structure. Mechanotransduction refers to the mechanisms by which cells sense physical forces, transduce the forces into biochemical signals, and generate appropriate responses leading to alterations in the cellular structure and function [8, 167]. Mechanotransduction is a key component of myocytes since cardiac cells are constantly sensing and transducing external forces, and at the same time developing internal contractile forces [10, 168]. The mechanical forces sensed by myocytes are linked to chemical signals that lead to modifications both within the cell with changes occurring in signaling proteins, the contractile apparatus, and the cytoskeleton, and outside the cell with a dynamic restructuring of the extracellular matrix (ECM). These structural changes alter the mechanical properties of the cells and the ECM, resulting in a redistribution of mechanical stimuli until a new (mechanical and biological) equilibrium is achieved. This balancing system is an essential part of normal cardiac growth and development, but when the system goes out of balance, the result can lead to abnormal physiology and disease [10]. Myocyte mechanotransduction, although not well understood, is directly involved in the development of heart disease [169]. Therefore, an understanding of mechanotransduction and the changes to cytoskeletal proteins with aging is crucial for a better understanding of the mechanisms involved in the progression to cardiac dysfunction with aging.

In this thesis, it was shown that some proteins involved with mechanotransduction changed with age (Table 4.5). While an upregulation in β1-Integrin (Figure 4.6), Vinculin (Figure 4.7), and Filamin-C (Figure 4.10) was detected, no change was observed in the expression of α-actinin (Figure 4.9) and Talin (Figure 4.8). Cardiac myocyte integrins are not randomly distributed on the cell surface but are found embedded within the sarcolemmal membrane [170]. β1-Integrin is regarded as a strain transducer and is the main receptor that connects the cytoskeleton to the ECM [13]. Integrins were initially thought of as molecules necessary for adhesive interactions between cells and the ECM, but it has been shown that they are bidirectional signaling molecules involved in external to internal signaling and vice versa in internal to external signaling [171]. They provide a linkage between the cardiac ECM and the cardiac myocyte cytoskeleton through several proteins (talin, α-actinin, filamin, etc.) [8]. Various studies have been conducted to investigate the role of integrins in cardiac function. An aging study on mice revealed a down regulation (reduction) in β1-Integrin measured by immunoblot techniques [172]. This finding is in disagreement with this study; however, Burgers et al.'s experiments were conducted for a different species (mouse). Cardiac myocytes require integrin adhesion to stay alive. The signals resulting from integrin attachment, along with growth factor receptors, prevent apoptosis (programmed cell death) [173]. Apoptosis is known to take place with cardiac aging [50]; therefore, an upregulation of β1-Integrin with aging could possibly be a preventive response to these events. Investigations involving the over-expression of β1-Integrin have demonstrated the importance of integrins in cardiac function. The over-expression of β1-Integrin in the rat cardiac myocyte was found to increase hypertrophic marker gene expression and protein synthesis [15]; moreover, it resulted in reduced contractility and relaxation in the intact heart [174]. Previous studies have shown that aging is accompanied by hypertrophy and contractility dysfunction [50], as was also shown in this thesis. Furthermore, it was also demonstrated that the removal of β1-Integrin impaired cardiac function, weakened myocyte membranes, and reduced the ability of the heart to withstand pressure overload, while not enhancing apoptosis [175]. The relationship between β1-Integrin and the amount of microtubules (cytoskeletal protein) was investigated, with a β1-Integrin blocking agent inhibiting the stretch-induced increase in microtubule polymerization in hypertrophic cardiac myocytes [14]. Therefore, it could be assumed that an increase in β1-Integrin could promote an increase in microtubule polymerization. This would fall in line with the results of the current study where an increase in both α and β tubulin is observed with aging (Table 4.5).

Vinculin plays a role in muscle structure and stability to mechanical forces, and is involved in the attachment of myofibrils to the sarcolemma, and in the lateral translation of force through the extracellular matrix to neighboring myocytes (as reviewed by [176]. Vinculin contributes to the stability of both the cellular membrane and the intracellular–extracellular connections via the integrins. The protein Vinculin has also been associated with adhesion [177], while the loss of this protein has been linked to myocardial fragility in isolated, perfused rat hearts [178, 179]. It was also shown that a partial reduction of decreased Vinculin leads to abnormal myocyte structure (disorganized Z-lines), but without physiological evidence of cardiac dysfunction [180]. An increase of Vinculin has been revealed in failing human hearts [181]. A study conducted with AFM indentation on Vinculin deficient cells demonstrated that a decrease in Vinculin resulted in a decrease in measured stiffness [182, 183]. Therefore, one can assume that an increase in vinculin would contribute to an increase in stiffness measured by AFM nanoindentation.

Filamin-C is mainly a structural protein that belongs to an extended family of actin-binding proteins [20]. Loo et al. [21] suggested that the interaction between β1-Integrin and Filamin provides a mechanism for the interaction of the cell surface receptor with cytoskeletal proteins, and that this interaction may play an important role in the normal receptor function. The increase in Filamin-C with aging detected in this study could be an indication of increased actin binding, which could result in direct changes of the myocyte's cytoskeletal properties.

The analysis of cytoskeleton protein changes indicated a significant increase in α-tubulin (Figure 4.11) and β-tubulin (Figure 4.12). It is generally accepted that the main role of the microtubular network is to act as a transport system which sends particles between sites that synthesize proteins and lipids [23, 24]. However, the importance of microtubules in the development of hypertrophy and heart failure has been investigated by several groups and remains controversial. Investigations by Cooper's group on feline right ventricular hypertrophy showed contractile dysfunction in isolated myocytes [184, 185] and loss of compliance [186]. These changes were accompanied by increased cytoskeletal stiffness characterized by a change in the amount of total Tubulin and an elevated degree of polymerization. The conclusions from the present thesis are such that an increased microtubule amount could be related to increased cellular stiffness. The role of microtubules in cardiac hypertrophy and failure was further investigated by Cooper's group in numerous experimental studies that showed the reduction of microtubules with colchicines (microtubule depolymerizing agent) treatment, which in turn reversed myocyte stiffness and returned contraction dynamics. Studies by Cooper's group also showed that Taxol (microtubule polymerizing agent) treatment of normal myocytes produced an overload of microtubules and cardiac dysfunction similar to what has been observed in in-vivo hypertrophy [7]. The conclusion drawn from the studies of Cooper's group was that cytoskeletal abnormalities, rather than changes of myofilaments, are responsible for cellular contractile dysfunction observed in hypertrophied and the failing heart. Contractile dysfunction, seen in cardiac hypertrophy, was considered to be a result of an increased density of microtubules [7]. The same group published data on the role of microtubules in the transition from compensated to decompensated hypertrophy in a canine model of left ventricular pressure overload due to aortic banding [22]. Isolated myocytes from failing hearts showed contractile dysfunction and an increase in microtubules, which could both be reversed with colchicines treatment. The findings of Copper's group have been questioned by others including Bailey et al. [187] who did not observe an effect of colchicine on contraction dynamics in isolated feline myocytes from hypertrophied hearts, and de Tombe [188] who did not observe any effect of colchicine and taxol on rat trabeculae contractility.

The view of Cooper's group is that an increase in microtubules is an important factor in causing cytoskeletal stiffness and contractile dysfunction is shared by Wang et al. [189] who examined the transition from hypertrophy to failure in guinea pig hearts. Wang found an increase in microtubule density using quantitative confocal microscopy, but no increase in total tubulin in Western blots. These findings led Wang to believe that changes in the cytoskeleton (including desmin and titin) may be involved in ventricular dysfunction. Collins et al. [190], using the same guinea-pig model for studying hypertrophy and failure, came to the conclusion that neither the level of tubulin nor the degree of polymerization is involved in changes occurring in cardiac hypertrophy. The results of the aging study presented above show a significant upregulation in α and β tubulin (Table 4.5), a decrease in contractile function (Figure 2.4), and an increase in myocyte stiffness (Figure 2.7). Whether the myocyte functional changes are solely linked to microtubule changes is not yet established; however, the previous work suggests that there is a role of microtubules in cardiac function.

This thesis has also shown a decrease in the intermediate filament Desmin (Figure 4.13), which plays an essential role in maintaining muscle cytoarchitecture by forming a three-dimensional scaffold around the myofibrillar Z-disk and by connecting the entire contractile apparatus to the subsarcolemmal cytoskeleton, the nuclei, and other organelles [28, 29]. Studies in Desmin knockout mice (Des−/−) have been conducted to demonstrate Desmin's function. Although these (lacking Desmin) mice develop normally and are fertile, after birth, they suffer from cardiomyopathy, skeletal myopathy, and smooth muscle dysfunction, which reduce their life span and make them less tolerant to exercise [191, 192]. Moreover, a heart without Desmin develops cardiomyocyte hypertrophy and eventual cardiomyopathy characterized by cardiomyocyte death, calcification, and ECM changes [192, 193].

The mechanical function of the Desmin filaments in the heart wall has also been studied by means of a Langendorf technique which showed an increase in diastolic pressure, lower developed pressure, and structural remodelling of the ventricle [27]. It has been suggested that the contractile apparatus generates less active force in Des−/− [194], which could result from a change in the structure of the ventricle wall, an inability of the cell to transmit forces, or an inability to align sarcomeres. Desmin filaments may be involved in generating active force in the cardiac muscle by supporting sarcomere alignment and force transmission [27]. The morphology and function of mitochondria are also abnormal in mice lacking Desmin [192, 193]. Studies suggest that the Desmin cytoskeleton influences the position, movement, and activity of mitochondria in cardiac muscle [195, 196]. The results of previous studies suggest that a reduction in Desmin could contribute to the changes seen with aging where contractile dysfunction (Figure 2.4), myocyte hypertrophy (Table 2.2), and a down regulation in Desmin (Table 4.5) were found.

In this thesis, an instrumentation technique was developed to determine the effects of aging induced cellular changes on global cardiac function in the aging rat model. LV pressure and dimension were measured in a conscious rat (Figure 5.8). The pressure measurements compared well to previously published work in conscious rats with a fluid catheter [197], a telemetered pressure volume catheter [198], and in several studies performed on anesthesized animals [63]. Cardiac contractility was altered by delivery of isoproterenol (Figure 5.14) and dobutamine (Figure 5.16), as evidenced by the index of cardiac contractility (dP/dt) which increased as higher drug doses were delivered. The observed change in dP/dt was found to be in good agreement with previously published work [197]. Moreover, a clear difference was observed between young and old rats' responses to isoproterenol and dobutamine. These results are the first to demonstrate β-adrenergic dysfunction in a conscious aged rat model, although such a dysfunction had previously been described in in-vitro setups of isolated cells and hearts [50, 67]. The anesthesized pressure volume relationships compared well with previously published work [63]. In addition, a new method was developed to produce occlusions in conscious rats, which will allow future independent load measures of contractility to be conducted in conscious young and old rats.

In conclusion, this is the first study to use the AFM to examine either a disease state or a change in physiological function in cardiac myocytes. The findings indicate that the altered LV diastolic function in the whole heart resulting from age may not only be due to structural changes in the heart, but also due to changes occurring at the single myocyte level, such changes being independent of the extra cellular matrix. A limitation of this study, as well as of most other studies examining myocyte function, is that the yield of healthy myocytes is less in the old heart than in the young heart. However, there is very little difference in myocyte function in cells from young rats over a broad range of cell sizes, although there is a reduction in yield (Table 2.1). Material property changes were seen in proteins involved in mechanotransduction and cytoskeletal structure (Table 4.5). Future investigations in this area will need to examine not only alterations in collagen/elastin, but also the mechanisms involved in changing the myocyte's resilience and stiffness, as well as potential differences due to gender. The development of the novel method presented above to measure LV pressure and dimensions within the conscious rat will also allow further testing of the effects of cellular changes on the entire cardiac function.

APPENDIX A

AFM FLUID CELL OPERATION

This appendix covers the use a fluid cell which consists of a small glass assembly with a wire clip for holding an AFM probe (Figure A.1).

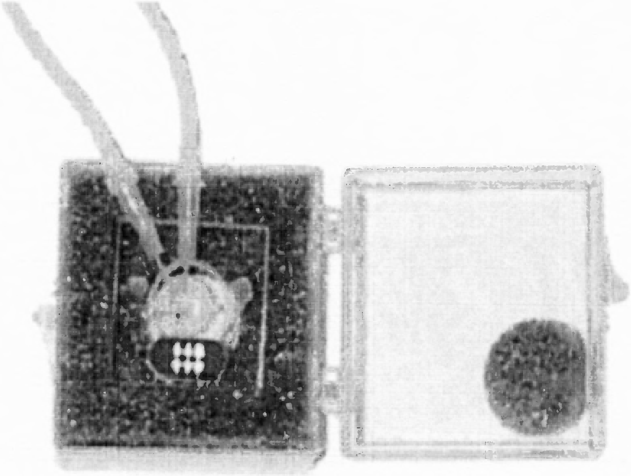

Figure A.1 Tapping Mode Fluid Cell in Case. Images Courtesy of Digital Instruments, Santa Barbara CA.

The glass surfaces provide a flat, beveled interface so that the AFM laser beam may pass into the fluid without being distorted by an unstable fluid surface (Fluid Cell Operation Information From Digital Instruments Support Note 290B Fluid Operation)[199].

A.1 Clean Fluid Cell and O-ring.

To reduce contamination problems and to obtain high-quality images, it is necessary to clean the fluid cell, and O-ring if applicable, in the following manner:

1. While soaking the fluid cell and O-ring in warm, soapy water, place a few drops of liquid dish soap on them.

2. Gently rub the fluid cell and O-ring with a cotton swab or finger. Avoid scratching the glass surface with abrasive material.
3. Using distilled water, rinse the fluid cell and O-ring of all soap.
4. Using 0.2 mm-filtered, compressed air or dry nitrogen, blow dry the fluid cell until all moisture evaporates.

A.2 Select the Probe

AFM probes featuring low stiffness cantilevers produce the best results for biological applications. Models NP-S (standard) or NP-STT (oriented twin tip) 100μm ("short"), V-shaped cantilevers with oxide-sharpened silicon nitride tips are recommended.

A.3 Remove Organic Contamination from the Probe Tip

Since contaminants on the probe tip may limit AFM resolution, it is necessary to use ultraviolet (UV) light to remove contaminants, in the following manner:

1. Place the fluid cell with installed tip face-up on a clean surface.
2. Position a UV lamp very close (3-5 mm) to the fluid cell and irradiate the probe for two minutes at full intensity.

A.4 Load the Fluid Cell with a Probe

The probe is held in a small pocket on the bottom side of the fluid cell by a gold plated, stainless steel wire clip. A tiny coil spring mounted on the top of the fluid cell holds the wire clip against the probe. Load a probe into the fluid cell by performing the following procedure:

1. Turn the fluid cell upside down, and gently raise the wire clip by pressing from beneath.
2. With the wire clip raised, use tweezers to slide a probe into the pocket. Lower the clip to hold the probe (Figure A.2).

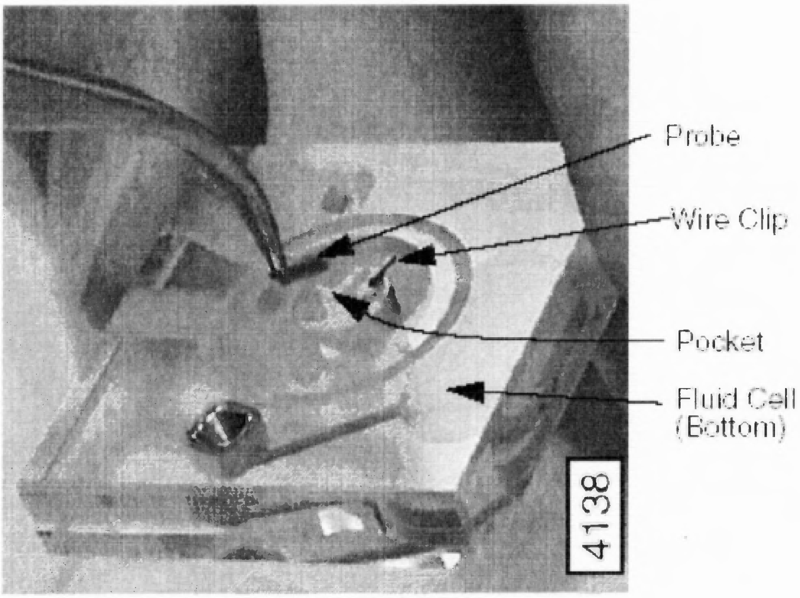

Figure A.2 Probe loaded into the fluid cell. Image courtesy of Digital Instruments, Santa Barbara CA.

3. Verify that the probe is squarely set against one side of the pocket and flush against the back. Verify the probe is held firmly by the wire.

A.5 Sample Mounting

Secure a 15mm glass sample slide containing cells to a magnetic stainless steel sample puck. Supports may be secured to the puck with epoxy (Fig. 3.5).

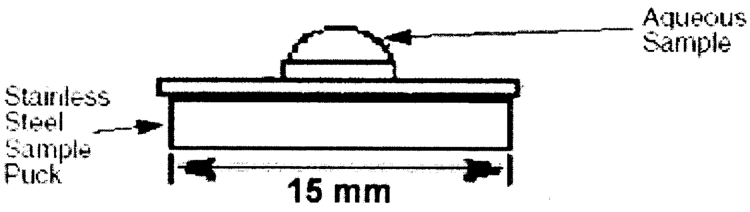

Figure A.3 Stainless-steel puck with aqueous sample image courtesy of Digital Instruments, Santa Barbara CA.

A.6 Method To Load Fluid Cell With Solution

A.6.1 Install The Protective O-Ring Into The Fluid Cell

1. Insert the O-ring into the recessed groove in the underside of the fluid cell. The O-ring slides up into the recessed groove.
2. Position the O-ring so that it forms a seal around its periphery and does not overlap any edges.

A.6.2 Pre-Wet The Fluid Cell (Figure A.4)

Occasionally, air bubbles form in the fluid cell and block laser light. Preventing bubbles from forming can be obtained by following the steps below:

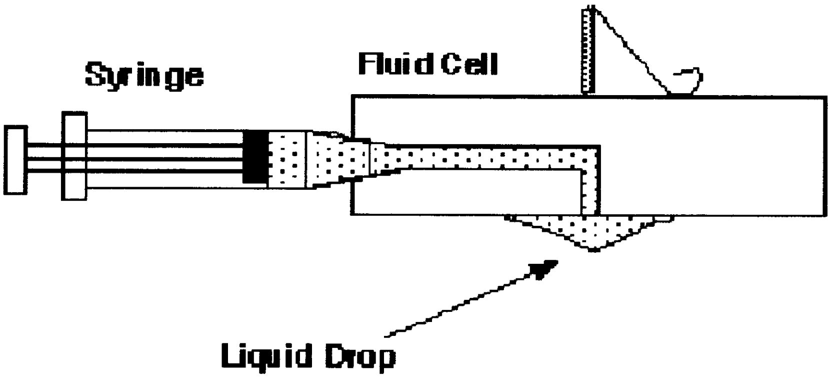

Figure A.4 Fluid inserted into the fluid cell. Sample image courtesy of Digital Instruments, Santa Barbara CA.

1. Before installing the fluid cell into the head, insert a syringe filled with liquid solution into a fluid port, or connect the syringe to the inlet tubing on the fluid cell.
2. Push enough fluid through the fluid chamber in order to flood the fluid cell port, allowing liquid to drip out of the bottom of the cell.
3. Leave the solution-filled syringe inserted. A small amount of solution should be held to the bottom of the cell by surface tension.

A.6.3 Install The Sample.

Install the sample attached to puck in the AFM head.

A.6.4 Install The Fluid Cell

Carefully install the fluid cell in the AFM head (Figure A.5).

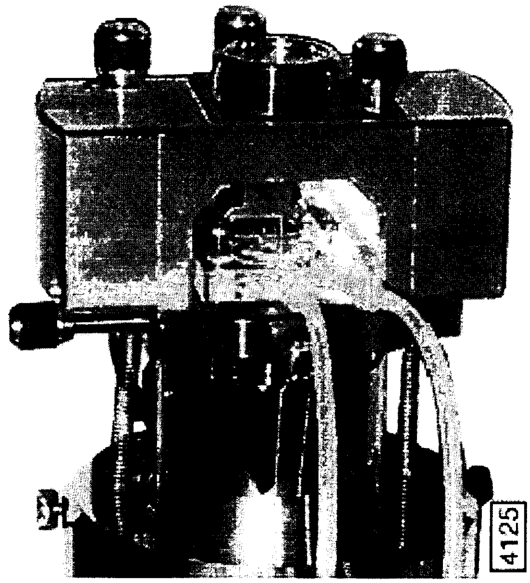

Figure A.5 Fluid cell inserted into AFM head. Sample image courtesy of Digital Instruments, Santa Barbara CA.

1. Tighten the clamp to hold the fluid cell in place, making certain that the O-ring positions properly between the sample and the fluid cell.
2. Verify the head is leveled side-to-side and that the head is tilted slightly forward, so the tip is leveled when it contacts the surface.
3. Fill the fluid cell with liquid. Limit the volume of liquid in the fluid cell to 30 – 50 μl, if possible, in order to limit thermal drift.
    a. Attach a drain line to the other fluid cell port.
    b. Slowly flush the fluid cell with solution from the syringe. Check for leaks and wipe away any spilled liquid with filter paper until the AFM components are dry.
4. Remove bubbles and clamp off fluid cell lines. Bubbles inside the fluid cell near or on the probe can interfere with the laser beam. Remove them by performing the following procedure:
    a. Observe the fluid cell and probe through the viewing port using an optical microscope.
    b. Rapidly push liquid through the cell with a syringe. If sufficient force is applied, the bubbles will be carried out of the fluid cell.
    c. Clamp off the drain line with a pair of hemostats or similar clamp.
5. Adjust the laser:
    a. If the presence of fluid causes the laser spot to refract, slightly adjust the laser aiming screw, to move the laser spot onto the end of the probe.

b. If air bubbles become trapped near the probe, interfering with the laser beam path, use the syringe to force liquid quickly through the cell to break the bubbles loose.

A.7 Align the Laser

Use the x- and y- laser adjustment knobs to align laser spot onto the tip of the cantilever. Insert a small slip of paper into the laser beam path to perform fine laser alignment. Carefully adjust the laser adjustment knobs in both directions to achieve a solid rectangle bar-shaped pattern reflected onto the slip of paper.

A.8 Adjust the Detector Offsets and Setpoint (Contact Mode)

Turn the detector mirror adjustment screws to center the laser spot on the laser detector. For contact mode, set the vertical deflection signal to roughly -1.0 V and the setpoint to 0 V to begin. The difference between the vertical deflection signal before engaging and the setpoint determines the amount of force that the probe applies to the sample. Typically, samples are softer in liquid than in air. Before engaging, verify that there is not much difference between the setpoint and the vertical deflection signal as to damage the sample.

A.9 Engage the Surface

Using the coarse adjustment screws and MOTOR DOWN switch on the NanoScope® MultiMode™ ™ base, lower the tip until it is just above the level of the sample surface. In the Real Time / Motor menu, click ENGAGE, or click the Engage icon. The motor begins to move the AFM head and probe down to the sample. When the tip reaches the surface, the system should automatically stop, beep, and begin to image the sample.

A.10 Adjust Scan Parameters (Contact Mode)

Once engaged, adjust the scan parameters to obtain the best image as follows. To avoid sample damage, adjust the setpoint as low as possible:

1. Reduce the setpoint in increments of 1/100 volt.
2. Stop when the tip pulls off the surface and the Z Center Position on the display monitor jumps to Limit (-220 V).
3. Increase the setpoint until the tip begins to touch the surface again and an image appears.
4. Set the two gains as high as possible (starting with the integral gain) without causing oscillation distortion to appear in your image.
5. Choose a scan rate that is sufficiently slow to image without degrading your data.

A.11 Fluid Cell Operation In Tapping Mode

Operation of Tapping Mode in fluid provides the same advantages of TappingMode in air, with the additional ability to image samples under native liquid conditions. In fluid TappingMode, the probe is oscillated so that it only intermittently contacts the sample surface. This can reduce or eliminate lateral forces that can damage soft or fragile samples in contact mode.

A.11.1 Procedure for Tapping Mode Imaging in Fluid

1. Load the sample in the AFM.
2. Align the laser on the end of the cantilever portion of the probe.
3. Center the photodiode to give a deflection signal near 0V.
4. Choose the TappingMode operation in software.
5. Set the initial scan parameters, by entering the View/Sweep/Cantilever Tune menu to select a drive frequency and manually tune the probe using the Zoom in and Offset functions above the Cantilever Tune display.
6. Center the laser spot on the photodiode detector. Adjust the photodiode until deflection is roughly zero. The deflection signal can drift when the probe is first in fluid, so it is best to adjust just prior to engaging.
7. Click the Engage icon to bring the tip into tapping range.
8. Adjust the setpoint when engaged.

APPENDIX B

INFINITESIMAL INDENTATION SUPERIMPOSED ON A FINITE EQUIBIAXIAL STRETCH

This appendix covers the development of the formulas used related to the infinitesimal indentation by a rigid axisymmetric punch superposed on finite deformations of an elastic half-space for compressible and incompressible, isotropic, hyperelastic materials taken from the following sources [123, 132-134, 152]. Costa [123] presented the equations relating indentation force and depth for axisymmetric punch geometries based on Humphrey's work [134]considering incompressible materials indented by a flat-ended cylinder.

The following is the general equation for the total force (P) exerted by an indenter for infinitesimal indentations perpendicular to the finite stretch [123, 133].

$$P=2\cdot\pi\cdot\frac{\Gamma(W)}{\Sigma(W)}\cdot\phi(d) \tag{B.1}$$

Where $\phi(d)$ is a function of the indenter geometry, which determines the dependence of P on the penetration depth (d). $\Gamma(W)$ and $\Sigma(W)$ incorporate the material properties and in-plane deformation through their dependence on the strain energy function, $W(I_1, I_2)$, and the principal strain invariants, I_1 and I_2. For finite equibiaxial stretch, μ, the deformation gradient tensor is $F=\mathrm{diag}\{\mu,\mu,\lambda\}$, where $\lambda=\mu^{-2}$ to satisfy material incompressibility. For incompressible materials Γ and Σ can be written as

$$\Gamma=\frac{\left(q_1\cdot k_1+q_2\right)\cdot\sqrt{k_1}}{1+k_1}-\frac{\left(q_1\cdot k_2+q_2\right)\cdot\sqrt{k_2}}{1+k_2}$$

$$\Sigma=\frac{k_1}{1+k_1}-\frac{k_2}{1+k_2} \qquad \text{(B.2)}$$

where k_1 and k_2 are roots of the following quadratic equation for K[134]

$$m\cdot K^2+(l+m-n-o)\cdot K+l=0 \qquad \text{(B.3)}$$

where

$$l=2\cdot\lambda^2\cdot\left(W_1+\mu^2\cdot W_2\right)$$

$$m=2\cdot\mu^2\cdot\left(W_1+\mu^2\cdot W_2\right)$$

$$n=4\cdot\mu^2\left[\left(W_1+\mu^2\cdot W_2\right)+(\mu^2-\lambda^2)\cdot\left[W_{11}+W_{22}\cdot\mu^2\cdot(\lambda^2+\mu^2)+W_{12}\cdot(\lambda^2+2\cdot\mu^2)\right]\right.$$

$$o=4\cdot\lambda^2\cdot\left[\left(W_1+\mu^2\cdot W_2\right)+(\lambda^2-\mu^2)\cdot\left(W_{11}+2\cdot W_{22}\cdot\mu^4+3\cdot W_{12}\cdot\mu^2\right)\right]$$

where W_{ij} (i, j=1, 2) are second derivatives of W with respect to I_i or I_j and

$$q_1=2\cdot\mu^2\cdot\left(W_1+\mu^2\cdot W_2\right) \qquad \text{(B.4a)}$$

$$q_2=2\cdot\lambda^2\cdot\left(W_1+\mu^2\cdot W_2\right) \qquad \text{(B.4b)}$$

Where W1 and W2 are derivatives of W with respect to I_1 and I_2,respectively [123].

The special case of zero in-plane stretch ($\mu=\lambda=1$ and $k_1=k_2=1$), yields $\Gamma=\Sigma=0$, such that Γ/Σ is indeterminate. This limit can be found by first setting $k_1=1$ in (B.2)

$$\left(\frac{\Gamma}{\Sigma}\right)_{k_1=1}=\frac{2\cdot l_1\cdot k_2+\left(l_1-l_2\right)\cdot\sqrt{k_2}+l_1+l_2}{\sqrt{k_2}+1} \qquad \text{(B.5)}$$

with $k_2=1$ and (B.4a), yields

$$\lim_{\mu\to 1}\frac{\Gamma}{\Sigma}=4\cdot\left(W_1+W_2\right)_{\mu=1}=E_g \qquad \text{(B.6)}$$

E_g is a generalized elastic modulus for any isotropic, incompressible, hyperelastic material in its unstretched state. Classical solutions for the infinitesimal indentation are expressed in terms of

$$E_c=\frac{E}{1-\nu^2} \qquad \text{(B.7)}$$

E is Young's modulus and ν is Poisson's ratio. For incompressible materials ν is 0.5 [127]. For the case of linear hyperelastic materials, where $W_1=C_1$ and $W_2=C_2$ are constants, E_g from (B.6) is equal to 2/3 the Young's modulus given by $E=6(C1+C2)$ [123, 155]. Equation (B.1) becomes

$$P=2\cdot\pi\cdot E_g\cdot\phi(d)=\frac{4}{3}\cdot E\cdot\pi\cdot\phi(d) \tag{B.8}$$

Where d is the indentation depth measured from the free surface at the axis of symmetry. Costa's system [123] involves obtaining $\phi(d)$ from existing solutions to express them in the form of (B.8). Expressions for $\phi(d)$ for a rigid spherical and conical punch indenter geometries were developed because many of the axisymmetric punch shapes of principal interest can be described by a quadratic function [133].

$$f(r)=c_0+c_1\cdot r+c_2\cdot r^2 \tag{B.9}$$

Where c_β, $\beta=0,1,2$, are constants determined from the assigned geometry. The radius of the circle of contact is a. The variable r describes the convex punch shape as the radial distance from the axis in the range $0\leq r\leq a$. From [133] we obtain a relation for $\phi(d)$.

$$\phi(r,a)=\left(a^2-r^2\right)^{\frac{1}{2}}\cdot\left[\frac{2\cdot c_o}{\pi}+\frac{1}{2}\cdot c_1\cdot\left[a+r^2\cdot\left(a^2-r^2\right)^{\frac{-1}{2}}\cdot\cosh^{-1}\left(\frac{a}{r}\right)\right]+\frac{4\cdot c_2}{3\cdot\pi}\cdot\left(a^2+2\cdot r^2\right)\right] \tag{B.10}$$

When r =0, this expression reduces to

$$\phi(0,a)=a\cdot\left(\frac{2\cdot c_o}{\pi}+\frac{1}{2}\cdot c_1\cdot a+\frac{4\cdot c_2\cdot a^2}{3\cdot\pi}\right) \tag{B.11}$$

Specific punch shapes can be determined with this relation.

Cone With Tip Angle, 2α [126, 133]

The indentation of a conical punch of apex angle 2α may be described by

$$f(r)=d-r\cdot\cot(\alpha) \tag{B.12}$$

where d denotes the maximum depth of indentation. Therefore,

$c_o=d$, $c_1=-\cot(\alpha)$, and $c_2=0$ in (B.11)

gives

$$\phi(0,a)=a\cdot\left(\frac{2\cdot d}{\pi}-\frac{1}{2}\cdot\cot(\alpha)\cdot a\right) \tag{B.13}$$

The incremental stress should not become infinite at the ultimate circle of contact r=a. To this end,

$$\frac{d}{dr}\phi(r,a)$$

should be finite , therefore

$$2\cdot d=\pi\cdot a\cdot\cot(\alpha) \tag{B.14}$$

Putting (B.14) into (B.13) gives

$$\phi(0,a)=a\cdot\left(\frac{\pi\cdot a\cdot\cot(\alpha)}{\pi}-\frac{1}{2}\cdot\cot(\alpha)\cdot a\right)$$

which simplifies to

$$\phi(d)=\frac{2\cdot\tan(\alpha)}{\pi^2}\cdot d^2 \tag{B.15}$$

This is the conical indenter geometry function.

Sphere With Radius, R [133]

The infinitesimal indentation by a spherical punch of radius R is characterized by

$$f(r)=d-\frac{r^2}{2\cdot R} \tag{B.16}$$

therefore

c_o=d, c_1=0, and c_2=-1/2R in (B.11) gives

$$\phi(0,a)=r_o\cdot\left(\frac{2\cdot d}{\pi}-\frac{2\cdot a^2}{3\cdot\pi\cdot R}\right) \tag{B.17}$$

In order that the incremental stress distribution [133] be finite at r=a, we must have

$$a^2 = R \cdot d \tag{B.18}$$

Inserting (B.18) into (B.17) we get

$$\phi(0,a) = \sqrt{R \cdot d} \cdot \left(\frac{2 \cdot d}{\pi} - \frac{2 \cdot R \cdot d}{3 \cdot \pi \cdot R} \right)$$

which simplifies to

$$\phi(d) = \frac{4}{3 \cdot \pi} \cdot \sqrt{R \cdot d^3} \tag{B.19}$$

This is the rigid spherical indenter geometry function.

Blunt Cone With Tip Angle 2α, Which Transitions At Radius R [152]

$\phi(d)$ for a blunt cone with tip angle 2α, which transitions at radius b into a spherical tip of radius R was examined with Briscoe's method [152].

The reciprocal theorem relates the P(d) function for any axisymmetric indenter, to the pressure distribution produced by a cylindrical punch of the same projected area as

$$P = \int_0^a \sigma(r) \cdot \frac{f(r)}{D} \cdot 2 \cdot \pi \cdot r\,dr \tag{B.20}$$

Where $\sigma(r)$ and D are the pressure distribution and depth of indentation respectively for the cylindrical punch, and f(r) is a function that specifies the indenter profile by its distance from the undeformed surface (d=0) as a function of the radial distance, r, from the axis $0 \le r \le a$. The pressure distribution under a perfect cylindrical punch is given by Sneddon [132]

$$\sigma(r) = \left(\frac{E_c}{\pi}\right) \cdot \frac{D}{\sqrt{a^2 - r^2}} \qquad \text{(B.21)}$$

Substituting (B.21) into (B.20), we get

$$P = 2 \cdot E_c \cdot \int_0^a \frac{f(r) \cdot r}{\sqrt{a^2 - r^2}} \, dr \qquad \text{(B.22)}$$

From Figure B.1 the function for a defective cone is

$$f(r) = d - \frac{r^2}{2 \cdot R} \qquad 0 \le a \le b \qquad \text{(B.23a)}$$

$$f(r) = d - \frac{(r - b)}{\tan(\alpha)} - d_c \qquad d_c = \frac{b^2}{2 \cdot R} \qquad b \le a \qquad \text{(B.23b)}$$

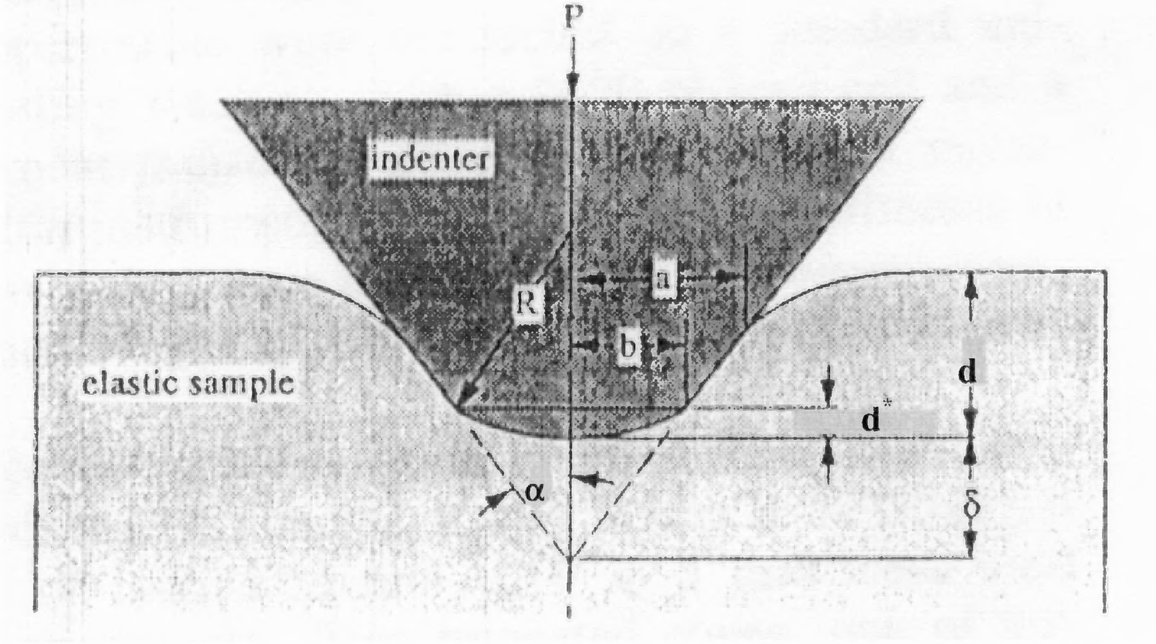

Figure B.1 A geometric model of a rigid cone with a spherical tip indenting an elastic half space[133].

When the spherical tip merges smoothly (tangential) with the body of the cone, the defect geometry is defined by R only and the corresponding value of b is given by b=Rcos(α).

When a≤b inserting (B.23a) into (B.22) gives

$$P=2\cdot E_c\cdot\int_0^a \frac{d-\frac{r^2}{2\cdot R}}{\sqrt{a^2-r^2}}\cdot r\,dr=2\cdot E_c\cdot\left(a\cdot d-\frac{a^3}{3\cdot R}\right) \tag{B.24}$$

The radius of the contact zone is determined by maximizing the value of P with respect to a, that is, ∂P/∂a=0, which results in $a=(Rd)^{1/2}$ and

$$P=\frac{4}{3}\cdot E_{c}\cdot\sqrt{R}\cdot d^{\frac{3}{2}}$$

The compliance equation for a sphere (Hertzian contact) where $\phi(d)$ is

$$\phi(d)=\frac{4}{3\cdot\pi}\cdot\sqrt{R\cdot d^{3}}$$

the rigid spherical indenter geometry function (B.19).

The depth of indentation corresponding to the transition from sphere indentation to (defective) cone indentation, d_s, is given by the boundary condition a=b; for which the value of d is $d_s=b^2/R=2d_c$.

The compliance equation when a≥b

$$P=2\,E_{c}\cdot\left[\int_{0}^{b}\left(d-\frac{r^{2}}{2\cdot R}\right)\cdot\frac{r}{\sqrt{a^{2}-r^{2}}}\,dr+\int_{b}^{a}\left(d-\frac{r-b}{\tan(\alpha)}-d_{c}\right)\cdot\frac{r}{\sqrt{a^{2}-r^{2}}}\,dr\right]$$

$$P=2\cdot E_{c}\cdot\left[d\cdot\left[\int_{0}^{a}\frac{r}{\sqrt{a^{2}-r^{2}}}\,dr\right]-\left[\left(\frac{1}{\tan(\alpha)}\right)\cdot\int_{a}^{b}\frac{r^{2}}{\sqrt{a^{2}-r^{2}}}\,dr\right]-\left(\frac{1}{2\cdot R}\right)\cdot\int_{0}^{b}\frac{r^{3}}{\sqrt{a^{2}-r^{2}}}\,dr+\left(\frac{b}{\tan(\alpha)}-d_{c}\right)\cdot\int_{b}^{a}\frac{r}{\sqrt{a^{2}-r^{2}}}\,dr\right]$$

$$P=2\cdot E_c\cdot\left[a\cdot d-\frac{a^2}{2\cdot\tan(\alpha)}\cdot\left(\frac{\pi}{2}-\operatorname{asin}\left(\frac{b}{a}\right)\right)-\frac{a^3}{3\cdot R}+\sqrt{a^2-b^2}\cdot\left(\frac{b}{2\cdot\tan(\alpha)}+\frac{a^2-b^2}{3\cdot R}\right)\right] \tag{B.25}$$

The condition ∂P/∂a=0 applied to the above equation gives

$$d+\frac{a}{R}\cdot\left(\sqrt{a^2-b^2}-a\right)-\frac{a}{\tan(\alpha)}\cdot\left(\frac{\pi}{2}-\operatorname{asin}\left(\frac{b}{a}\right)\right)=0 \tag{B.26}$$

Which is used to solve for the contact radius a. For $d<b^2/R$, $\phi(d)$ is given by (B.19) for a spherical indenter. When $d\geq b^2/R$, we have

$$\phi(d)=\frac{2}{\pi}\cdot\left[a\cdot d-\frac{a^2}{2\cdot\tan(\alpha)}\cdot\left(\frac{\pi}{2}-\operatorname{asin}\left(\frac{b}{a}\right)\right)-\frac{a^3}{3\cdot R}+\sqrt{a^2-b^2}\cdot\left(\frac{b}{2\cdot\tan(\alpha)}+\frac{a^2-b^2}{3\cdot R}\right)\right] \tag{B.27}$$

REFERENCES

1 D. E. Mohrman and L. J. Heller, *Cardiovascular Physiology*, Fifth ed. New York: McGraw Hill, 2003.

2 A. M. Katz, *Physiology of the Heart*, Third ed. New York: Lippincott Williams & Wilkins, 2001.

3 P. Camelliti, T. K. Borg, and P. Kohl, "Structural and functional characterisation of cardiac fibroblasts," *Cardiovasc Res*, vol. 65, pp. 40-51, 2005.

4 Y. C. Fung, *Biomechanics, Mechanical Properties of Living Tissues*, Second ed. New York: Springer-Verlag, 1993.

5 B. Alberts, D. Bray, K. Hopkin, A. Johnson, J. Lewis, M. Raff, K. Roberts, and P. Walter, *Essential Cell Biology*, Second ed. New York: Garland Science, 2004.

6 A. Fraticelli, R. Josephson, R. Danziger, E. Lakatta, and H. Spurgeon, "Morphological and contractile characteristics of rat cardiac myocytes from maturation to senescence," *Am J Physiol*, vol. 257, pp. H259-65, 1989.

7 S. Hein, S. Kostin, A. Heling, Y. Maeno, and J. Schaper, "The role of the cytoskeleton in heart failure," *Cardiovasc Res*, vol. 45, pp. 273-8, 2000.

8 A. M. Samarel, "Costameres, focal adhesions, and cardiomyocyte mechanotransduction," *Am J Physiol Heart Circ Physiol*, vol. 289, pp. H2291-301, 2005.

9 H. Huang, R. D. Kamm, and R. T. Lee, "Cell mechanics and mechanotransduction: pathways, probes, and physiology," *Am J Physiol Cell Physiol*, vol. 287, pp. C1-11, 2004.

10 M. A. Sussman, A. McCulloch, and T. K. Borg, "Dance band on the Titanic: biomechanical signaling in cardiac hypertrophy," *Circ Res*, vol. 91, pp. 888-98, 2002.

11 H. A. Kostin S, Hein S, Scholz D, Klövekorn WP, Schaper J, "The Protein Composition of the Normal and Diseased Cardiac Myocyte," *Heart Failure Reviews*, vol. 2, pp. 245-260, 1998.

12 S. Kostin, D. Scholz, T. Shimada, Y. Maeno, H. Mollnau, S. Hein, and J. Schaper, "The internal and external protein scaffold of the T-tubular system in cardiomyocytes," *Cell Tissue Res*, vol. 294, pp. 449-60, 1998.

13 M. L. Valencik, R. S. Keller, J. C. Loftus, and J. A. McDonald, "A lethal perinatal cardiac phenotype resulting from altered integrin function in cardiomyocytes," *J Card Fail*, vol. 8, pp. 262-72, 2002.

14 X. Yutao, W. Geru, B. Xiaojun, G. Tao, and M. Aiqun, "Mechanical stretch-induced hypertrophy of neonatal rat ventricular myocytes is mediated by beta(1)-integrin-microtubule signaling pathways," *Eur J Heart Fail*, 2005.

15 R. S. Ross, C. Pham, S. Y. Shai, J. I. Goldhaber, C. Fenczik, C. C. Glembotski, M. H. Ginsberg, and J. C. Loftus, "Beta1 integrins participate in the hypertrophic response of rat ventricular myocytes," *Circ Res*, vol. 82, pp. 1160-72, 1998.

16 E. A. Clark and J. S. Brugge, "Integrins and signal transduction pathways: the road taken," *Science*, vol. 268, pp. 233-9, 1995.

17 L. Terracio, D. G. Simpson, L. Hilenski, W. Carver, R. S. Decker, N. Vinson, and T. K. Borg, "Distribution of vinculin in the Z-disk of striated muscle: analysis by laser scanning confocal microscopy," *J Cell Physiol*, vol. 145, pp. 78-87, 1990.

18 A. R. Menkel, M. Kroemker, P. Bubeck, M. Ronsiek, G. Nikolai, and B. M. Jockusch, "Characterization of an F-actin-binding domain in the cytoskeletal protein vinculin," *J Cell Biol*, vol. 126, pp. 1231-40, 1994.

19 J. M. Sanger, B. Mittal, M. B. Pochapin, and J. W. Sanger, "Myofibrillogenesis in living cells microinjected with fluorescently labeled alpha-actinin," *J Cell Biol*, vol. 102, pp. 2053-66, 1986.

20 J. Lypowy, I. Y. Chen, and M. Abdellatif, "An alliance between Ras GTPase-activating protein, filamin C, and Ras GTPase-activating protein SH3 domain-binding protein regulates myocyte growth," *J Biol Chem*, vol. 280, pp. 25717-28, 2005.

21 D. T. Loo, S. B. Kanner, and A. Aruffo, "Filamin binds to the cytoplasmic domain of the beta1-integrin. Identification of amino acids responsible for this interaction," *J Biol Chem*, vol. 273, pp. 23304-12, 1998.

22 H. Tagawa, M. Koide, H. Sato, M. R. Zile, B. A. Carabello, and G. t. Cooper, "Cytoskeletal role in the transition from compensated to decompensated hypertrophy during adult canine left ventricular pressure overloading," *Circ Res*, vol. 82, pp. 751-61, 1998.

23 N. Hirokawa, "Kinesin and dynein superfamily proteins and the mechanism of organelle transport," *Science*, vol. 279, pp. 519-26, 1998.

24 S. O. Ioshii, K. Imanaka-Yoshida, and T. Yoshida, "Organization of calsequestrin-positive sarcoplasmic reticulum in rat cardiomyocytes in culture," *J Cell Physiol*, vol. 158, pp. 87-96, 1994.

25 H. Keurs, "Microtubules in cardiac hypertrophy: a mechanical role in decompensation?," *Circ Res.*, vol. 82, pp. 828-31, 1998.

26 J. L. Samuel, F. Marotte, C. Delcayre, and L. Rappaport, "Microtubule reorganization is related to rate of heart myocyte hypertrophy in rat," *Am J Physiol*, vol. 251, pp. H1118-25, 1986.

27 D. Paulin and Z. Li, "Desmin: a major intermediate filament protein essential for the structural integrity and function of muscle," *Exp Cell Res*, vol. 301, pp. 1-7, 2004.

28 E. Fuchs and K. Weber, "Intermediate filaments: structure, dynamics, function, and disease," *Annu Rev Biochem*, vol. 63, pp. 345-82, 1994.

29 J. V. Small and M. Gimona, "The cytoskeleton of the vertebrate smooth muscle cell," *Acta Physiol Scand*, vol. 164, pp. 341-8, 1998.

30 G. B. Cheng Zhu, and NingWang, "Cell Mechanics: Mechanical Response, Cell Adhesion, and Molecular Deformation," *Annu. Rev. Biomed. Eng.*, vol. 02, pp. 189–226, 2000.

31 A. W. Amos LA, *Molecules of the Cytoskeleton.* New York: Guilford, 1991.

32 T. Stossel, "On the crawling of animal cells," *Science*, vol. 260, pp. 1086-1094, 1993.

33 D. L. Ingber DE, Hansen L, Karp S, Liley H, et al., "Cellular tensegrity: exploring how mechanical changes in the cytoskeleton regulate cell growth, migration and tissue pattern during morphogenesis," *Int. Rev. Cytol.*, vol. 150, pp. 173-224, 1994.

34 P. D. Ingber DE, Sun Z, Betensky H, Wang N., "Cell shape, cytoskeletal mechanics, and cell cycle control in angiogenesis," *J. Biomech. Eng.*, vol. 28, pp. 1471-84, 1995.

35 B. R. Heidemann SR, "Mechanical tension as a regulator of axional development," *Neuro Toxicology*, vol. 15, pp. 95-108, 1994.

36 J. PA, "The cytoskeleton and cell signaling: component localization and mechanical coupling," *Physiol Rev.*, vol. 78, pp. 763-81, 1998.

37 M. T. Desai A, "Microtubule polymerization dynamics," *Ann Rev Cell & Develop Biol. 1997*, vol. 13, pp. 83-117, 1997.

38 D. Ingber, "Tensegrity: the architectural basis of cellular mechanotransduction," *Ann. Rev. Physiol. 1997*, vol. 59, pp. 575-99, 1997.

39 B. J. Wang N, Ingber DE, "Mechanotransduction across the cell surface and through the cytoskeleton," *Science*, vol. 260, pp. 1124-7, 1993.

40 K. HE., "Microtubules in cardiac hypertrophy: a mechanical role in decompensation?," *Circ Res.*, vol. 82, pp. 828-31, 1998.

41 R. Lewis, *Life, 3rd Edition.* New York: WCB/McGraw-Hill, 1998.

42 E. G. Lakatta, *Vascular Disease in the Older Person.* New York: CRC Press-Parthenon Publishers, 1998.

43 W. F. Ganong, *Review of Medical Physiology*, Twenty Second ed. New York: McGraw-Hill, 2005.

44 Y. C. Fung, *Biomechanics, Circulation*, Second ed. New York: Springer-Verlag, 1997.

45 E. G. Lakatta and D. Levy, "Arterial and cardiac aging: major shareholders in cardiovascular disease enterprises: Part II: the aging heart in health: links to heart disease," *Circulation*, vol. 107, pp. 346-54, 2003.

46 M. Courtois, P. A. Ludbrook, and S. J. Kovacs, "Unsolved problems in diastole," *Cardiol Clin*, vol. 18, pp. 653-67, 2000.

47 D. W. Kitzman, "Heart failure with normal systolic function," *Clin Geriatr Med*, vol. 16, pp. 489-512, 2000.

48 R. R. De Souza, "Aging of myocardial collagen," *Biogerontology*, vol. 3, pp. 325-35, 2002.

49 E. G. Lakatta and F. C. Yin, "Myocardial aging: functional alterations and related cellular mechanisms," *Am J Physiol*, vol. 242, pp. H927-41, 1982.

50 E. G. Lakatta and S. J. Sollott, "Perspectives on mammalian cardiovascular aging: humans to molecules," *Comp Biochem Physiol A Mol Integr Physiol*, vol. 132, pp. 699-721, 2002.

51 G. H. Templeton, M. R. Platt, J. T. Willerson, and M. L. Weisfeldt, "Influence of aging on left ventricular hemodynamics and stiffness in beagles," *Circ Res*, vol. 44, pp. 189-94, 1979.

52 R. L. Kane, T. A. McMahon, R. L. Wagner, and W. H. Abelmann, "Ventricular elastic modulus as a function of age in the Syrian golden hamster," *Circ Res*, vol. 38, pp. 74-80, 1976.

53 D. A. Brenner, C. S. Apstein, and K. W. Saupe, "Exercise training attenuates age-associated diastolic dysfunction in rats," *Circulation*, vol. 104, pp. 221-6, 2001.

54 R. F. Janz, B. R. Kubert, I. Mirsky, B. Korecky, and G. C. Taichman, "Effect of age on passive elastic stiffness of rat heart muscle," *Biophys J*, vol. 16, pp. 281-90, 1976.

55 D. P. Shreiner, M. L. Weisfeldt, and N. W. Shock, "Effects of age, sex, and breeding status on the rat heart," *Am J Physiol*, vol. 217, pp. 176-80, 1969.

56 D. A. Rothbaum, D. J. Shaw, C. S. Angell, and N. W. Shock, "Cardiac performance in the unanesthetized senescent male rat," *J Gerontol*, vol. 28, pp. 287-92, 1973.

57 M. L. Weisfeldt, W. A. Loeven, and N. W. Shock, "Resting and active mechanical properties of trabeculae carneae from aged male rats," *Am J Physiol*, vol. 220, pp. 1921-7, 1971.

58 S. Besse, V. Robert, P. Assayag, C. Delcayre, and B. Swynghedauw, "Nonsynchronous changes in myocardial collagen mRNA and protein during aging: effect of DOCA-salt hypertension," *Am J Physiol*, vol. 267, pp. H2237-44, 1994.

59 P. Anversa, T. Palackal, E. H. Sonnenblick, G. Olivetti, L. G. Meggs, and J. M. Capasso, "Myocyte cell loss and myocyte cellular hyperplasia in the hypertrophied aging rat heart," *Circ Res*, vol. 67, pp. 871-85, 1990.

60 U. Schmidt, F. del Monte, M. I. Miyamoto, T. Matsui, J. K. Gwathmey, A. Rosenzweig, and R. J. Hajjar, "Restoration of diastolic function in senescent rat hearts through adenoviral gene transfer of sarcoplasmic reticulum Ca(2+)-ATPase," *Circulation*, vol. 101, pp. 790-6, 2000.

61 S. J. Zieman, G. Gerstenblith, E. G. Lakatta, G. O. Rosas, K. Vandegaer, K. M. Ricker, and J. M. Hare, "Upregulation of the nitric oxide-cGMP pathway in aged myocardium: physiological response to l-arginine," *Circ Res*, vol. 88, pp. 97-102, 2001.

62 J. Wanagat, M. R. Wolff, and J. M. Aiken, "Age-associated changes in function, structure and mitochondrial genetic and enzymatic abnormalities in the Fischer 344 x Brown Norway F(1) hybrid rat heart," *J Mol Cell Cardiol*, vol. 34, pp. 17-28, 2002.

63 P. Pacher, J. G. Mabley, L. Liaudet, O. V. Evgenov, A. Marton, G. Hasko, M. Kollai, and C. Szabo, "Left ventricular pressure-volume relationship in a rat model of advanced aging-associated heart failure," *Am J Physiol Heart Circ Physiol*, vol. 287, pp. H2132-7, 2004.

64 G. Olivetti, M. Melissari, J. M. Capasso, and P. Anversa, "Cardiomyopathy of the aging human heart. Myocyte loss and reactive cellular hypertrophy," *Circ Res*, vol. 68, pp. 1560-8, 1991.

65 J. Kajstura, W. Cheng, R. Sarangarajan, P. Li, B. Li, J. A. Nitahara, S. Chapnick, K. Reiss, G. Olivetti, and P. Anversa, "Necrotic and apoptotic myocyte cell death in the aging heart of Fischer 344 rats," *Am J Physiol*, vol. 271, pp. H1215-28, 1996.

66 E. G. Lakatta, "Arterial and cardiac aging: major shareholders in cardiovascular disease enterprises: Part III: cellular and molecular clues to heart and arterial aging," *Circulation*, vol. 107, pp. 490-7, 2003.

67 E. G. Lakatta, "Cardiovascular regulatory mechanisms in advanced age," *Physiol Rev*, vol. 73, pp. 413-67, 1993.

68 G. C. F. Q. Binnig, and C. Gerber, "Atomic force microscope," *Phys. Rev. Lett.*, vol. 56, pp. 930-933, 1986.

69 H. J. Butt, E.K. Wolff, S.A.C. Gould, B.D. Northern, C.M. Peterson, and P.K. Hansma, "Imaging cells with the atomic force microscope," *J. Struct. Biol.*, vol. 105, pp. 54-61, 1990.

70 K. T. Chang L, Yorgancioglu M, Keller D, Pfeiffer J., "Cytoskeleton of living, unstained cells imaged by scanning force microscopy," *Biophys. J.*, vol. 64, pp. 1282-6, 1993.

71 P. H. a. D. S. E. Henderson, "Actin filament dynamics in living glial cells imaged by atomic force microscopy," *Science*, vol. 257, pp. 1944-1946, 1992.

72 W. H. G. a. R. M. Ezzell, "Viscoelasticity in Wild-Type and Vinculin-Deficient (5.51) Mouse F9 Embryonic Carcinoma Cells Examined by Atomic Force Microscopy and Rheology," *Exp. Cell Res.*, vol. 226, pp. 234-237, 1996.

73 U. G. Hofmann, Rotsch, C., Parak, W.J., and Radmacher, M., "Investigating the cytoskeleton of chicken cardiocytes with the atomic force microscope," *J. Struct. Biol.*, vol. 119, pp. 84-91, 1997.

74 R. Lal, and Scott A. John, "Biological applications of atomic force microscopy," *Am. J. Physiol.*, vol. 266, pp. C1-C21, 1994.

75 W. J. P. Jan Domke, Michael George, Hermann E. Gaub, and Manfred Radmacher, "Mapping the mechanical pulse of single cardiomyocytes with the atomic force microscope," *Eur. Biophys. J.*, vol. 28, pp. 179-186, 1999.

76 N. E. Dvorak JA, "Kinetic analysis of the mitotic cycle of living vertebrate cells by atomic force microscopy," *Exp Cell Res.*, vol. 242, pp. 69-74, 1998.

77 H. G. a. J. H. H. Hansma, "Biomolecular imaging with the atomic force microscope," *Annu Rev Biophys Biomol Struct 1994*, vol. 23, pp. 115-39, 1994.

78 D. S. a. R. L. SG Shroff, "Dynamic micromechanical properties of cultured rat atrial myocytes measured by atomic force microscopy," *Am. J. Physiol.*, vol. 269, pp. C286-C292, 1995.

79 K. A. Barbee, Davies, P.F. , and Lal, R., "Shear stress-induced reorganization of the surface topography of living endothelial cells imaged by atomic force microscopy," *Circ. Res.*, vol. 74, pp. 163-171, 1994.

80 J. K. H. Horber, W. Haberle, F. Ohnesorge, G. Binnig, H.G. Liebich, C.Z. Czerny, H. Mahnel, and A. Mayr, "Investigation of living cells in the nanometer regime with the scanning force microscope," *Scanning Microsc.*, vol. 6, pp. 919-930, 1992.

81 G. V. Kasas S, Celio MR, "Observation of living cells using the atomic force microscope," *Biophys. J.*, vol. 64, pp. 539-44, 1993.

82 M. T. Barbee KA, Lal R, Davies PF, "Subcellular distribution of shear stress at the surface of flow-aligned and nonaligned endothelial monolayers," *Am. J. Physiol.*, vol. 268, pp. H1765-72, 1995.

83 H. K. Miyazaki H, "Atomic force microscopic measurement of the mechanical properties of intact endothelial cells in fresh arteries," *Med. Biol. Eng. Comput.*, vol. 1999, pp. 530-6, 1999.

84 M. Radmacher, M. Fritz, C. M. Kacher, J. P. Cleveland, and P. K. Hansma, "Measuring the viscoelastic properties of human platelets with the atomic force microscope," *Biophys J*, vol. 70, pp. 556-67, 1996.

85 G. Binnig, C. Gerber, E. Stoll, T.R. Albrecht, and C.F. Quate, "Atomic resolution with atomic force microscope," *Europhys. Lett.*, vol. 3, pp. 1281-1286, 1987.

86 G. D. a. L. S. M. Heuberger, "Mapping the Local Young's Modulus by Analysis of the Elastic Deformations Occurring in Atomic Force Microscopy," *Nanotechnology*, vol. 5, 1994.

87 M. K. AL Weisenhorn, S Kasas, V Gotozos, MR Celio and HJ Butt, "Deformation and height anomaly of soft surfaces studied with the AFM," *Nanotechnology*, vol. 4, pp. 106-113, 1993.

88 M. Heuberger, Dietler, G. and Schlapbach, L., " J. Vac. Sci. Technol.," vol. B 14, pp. 1250-1254, 1996.

89 J. M. J. Yang, J.Y. Yuan and Z. Shao, "The effect of deformation on the lateral resolution of atomic force microscopy," *J. Microsc.*, vol. 182, pp. 106-113, 1996.

90 M. Radmacher, "Measuring the elastic properties of biological samples with the AFM," *IEEE Eng. Med. Biol. Mag.*, vol. 16, pp. 47-57, 1997.

91 B. N. J. Persson, "The atomic force microscope: Can it be used to study biological molecules?," *Chem. Phys. Lett.*, vol. 141, pp. 366-368, 1987.

92 R. Lal, and L. Yu, "Molecular structure of cloned nicotinic acetyl choline receptors expressed in Xenopus oocyte as revealed by atomic force microscopy," *Proc. Natl. Acad. Sci. USA*, vol. 90, pp. 7280-7284, 1993.

93 C. Rotsch, and Radmacher, M., "Drug-Induced Changes of Cytoskeletal Structure and Mechanics in Fibroblasts: An Atomic Force Microscopy Study," *Biophys. J.*, vol. 78, pp. 520-535, 2000.

94 C. P. B. Drake, A.L. Weisenhorn, SAC Gould, TR Albrecht, et al., "Imaging crystals, polymers and biological processes in water with AFM," *Science*, vol. 243, pp. 1586-1589, 1989.

95 J. H. W. Haberle, F Ohnesorge, DPE Smith and G Binnig, "In situ investigations of living cells infected by viruses," *Ultramicroscopy*, vol. 42-44, pp. 1161-1167, 1992.

96 M. R. a. H. G. M Fritz, "Granula motion and membrane spreading during activation of human platelets imaged by atomic force microscopy," *Biophys. J.*, vol. 66, pp. 1328-1334, 1994.

97 J. H. a. C.-A. Schoenenberger, "Surface morphology and mechanical properties of MDCK monolayers by atomic force microscopy," *J. Cell Sci.*, vol. 107, pp. 1105-1114, 1994.

98 B. D. R Lal, D Blumberg, DR Saner, HG Hansma, and SC Feinstein, "Imaging real-time neurite outgrowth and cytoseletal reorganization with an atomic force microscope," *Am. J. Physiol.*, vol. 269, pp. C275-C285, 1995.

99 E. B. H Oberleithner, G Giebisch and J Geibel, "Visualizing life on biomembrane by atomic force microscopy," *Kidney International*, vol. 48, pp. 923-929, 1995.

100 H.-A. K. a. F. L. M Beckmann, "Atomic force microscopy of peritoneal macrophages after particle phagocytosis," *Membrane Biol.*, vol. 140, pp. 197-204, 1994.

101 F. O. a. N. G. Goodman, "Roles of the attractive and repulsive forces in atomic force microscopy," *Physical Rev. B*, vol. 43, pp. 4728-4731, 1991.

102 H. J. Butt, "Measuring electrostatic, van der Waals, and hydration forces in electrolyte solutions with an atomic force microscope," *Biophys. J.*, vol. 60, pp. 1438-1444, 1991.

103 J. H. Hoh, J.P. Cleveland, C.B. Prater, J.P. Revel, and P.K. Hansma., "Quantized adhesion detected with the atomic force microscope," *J. Am. Chem. Soc.*, vol. 114, pp. 4917-4918, 1992.

104 S. H. P.A. Janmey, J. Käs, D. Lerche, A. Maggs, E. Sackmann, M. Schliwa and T.P. Stossel, "The mechanical properties of actin gels. Elastic modulus and filament motions," *J. Biol. Chem.*, vol. 269, pp. 32503-32513, 1994.

105 L. Stryer, *Biochemistry, 3rd Edition.* New York: W.H. Freeman and Company, 1988.

106 J. Hartwig, "Actin-binding proteins," *Curr. Op. Cell. Biol.*, vol. 3, pp. 87-97, 1991.

107 E. Sackmann, "Intra- and extracellular macromoecular networks: physic and biological function," *Macromol. Chem. Phys.*, vol. 195, pp. 7-28, 1994.

108 M. W. Petersen NO, Elson EL, "Dependence of locally measured cellular deformability on position on the cell, temperature, and cytochalasin B," *Proc. Natl. Acad. Sci. USA*, vol. 79, pp. 5327-31, 1982.

109 M. W. Zahalak GI, Elson EL, "Determination of cellular mechanical properties by cell poking, with an application to leukocytes," *J. Biomech. Eng.*, vol. 112, pp. 283-94, 1990.

110 Y. A. Evans E, "Apparent viscosity and cortical tension of blood granulocytes determined by micropipet aspiration," *Biophys. J.*, vol. 56, pp. 151-60, 1989.

111 N. M. a. E. E. DE Discher, "Molecular maps of red cell deformation: hidden elasticity and in situ connection," *Science*, vol. 266, pp. 1032-1035, 1994.

112 H. E. a. E. S. K Zeman, "Bending undulations and elasticity of the erythrocyte membrane organization," *Europ. Biophys. J.*, vol. 18, pp. 203-219, 1990.

113 A. A. a. J. Dziedzic, "Internal cell manipulation using infrared laser traps," *Proc. Natl. Acad. Sci.*, vol. 86, pp. 7914-7918, 1989.

114 C. S. K Svoboda, D Branton and SM Block, "Conformation and elasticity of the isolated red blood cell membrane skeleton," *Biophys. J.*, vol. 63, pp. 784-793, 1992.

115 K. H. H Luers, J Litniewski and J Bereiter-Hahn, "Acoustic microscopy of cultured cells. Distribution of forces and cytoskeletal elements.," *Cell Biophys.*, vol. 18, pp. 279-293, 1991.

116 J. H. a. D. Rugar, "Measurement of cellular elastic properties by acoustic microscopy," *J. Micros.*, vol. 134, pp. 245-260, 1984.

117 J. B. O. Pethica, W.C., "Tip surface interactions in STM and AFM," *Physica Scripta Volume T*, vol. Volume T19A, pp. 61-66, 1987.

118 N. B. a. R. J. Colton, "Measuring the nanomechanical properties and surface forces of materials using an atomic force microscope," *Journal of Vacuum Science & Technology A (Vacuum, Surfaces, and Films)*, vol. 7, pp. 2906-2913, 1989.

119 H.-J. B. P. Maivald, S.A.C. Gould, C.B. Prater, B. Drake, J.A. Gurley, V.B. Elings and P.K. Hansma, "Using force modulation to image surface elasticities with the atomic force microscope," *Nanotechnology*, vol. 2, pp. 103-106, 1991.

120 S. M. L. a. S. L. N.J. Tao, "Measuring the microelastic properties of biological material," *Biophysical Journal*, vol. 63, pp. 1165-1169, 1992.

121 P. K. H. A.L. Weisenhorn, T.R. Albrecht and C.F. Quate, "Forces in atomic force microscopy in air and water," *Appl. Phys. Lett.*, vol. 54, pp. 2651-2653, 1989.

122 P. B. B. Cappella, C. Frediani, P. Miccoli and C. Ascoli, "Force-distance curves by AFM. A powerful technique for studying surface interactions," *IEEE Eng. Med. Biol. Mag.*, vol. 16, pp. 58-65, 1997.

123 K. D. Costa and F. C. Yin, "Analysis of indentation: implications for measuring mechanical properties with atomic force microscopy," *J Biomech Eng*, vol. 121, pp. 462-71, 1999.

124 H. Hertz, "Uber die beruhrung fester elastischer korper (On the contact of elastic solids)," *J. Reine Angew. Mathematik*, vol. 92, pp. 156-157, 1881.

125 M. Radmacher, Fritz, M., and Hansma, P.K., "Imaging soft samples with the atomic force microscope: Gelatin in water and propanol," *Biophys. J.*, vol. 69, pp. 264-270, 1995.

126 A. E. H. Love, "Boussinesq's problem for a rigid cone," *Q.J. Math.*, vol. 10, pp. 161-175, 1939.

127 K. L. Johnson, *Contact Mechanics*. New York: Cambridge University Press, 1985.

128 Y. C. Fung, *Mechanical properties of living tissues*. New York, NY: Springer-Verlag, 1994.

129 S. A. T.R. Albrecht, T.E. Carver and C.F. Quate, "Microfabrication of cantilever styli for the atomic force microscope," *J. Vac. Sci. Technol. A 8*, vol. 8, pp. 3386-3396, 1990.

130 M. Tortonese, "Cantilevers and tips for atomic force microscopy," *IEEE Eng. Med. Biol. Mag.*, vol. 16, pp. 28-33, 1997.

131 A. S. Vinckier, G, "Measuring elasticity of biological materials by atomic force microscopy," *FEBS Letters*, vol. 430, pp. 12-16, 1998.

132 I. N. Sneddon, "The Relation between load and penetration in the axisymmetric Boussinesq problem for a punch of arbitrary profile," *Int. J. Engng. Sci.*, vol. 3, pp. 47-57, 1965.

133 M. F. Beatty, and Usmani, S.A., "On the indentation of a highly elastic half-space," *Quart. J. Mech. Appl. Math.*, vol. 28, pp. 47-62, 1975.

134 J. D. Humphrey, Halperin, H.R., and Yin, F.C.P., "Small Indentation on a finite equibiaxial stretch: Implications for cardiac mechanics," *ASME Journal of Applied Mechanics*, vol. 58, pp. 1108-1111, 1991.

135 W. C. Hayes, Keer, L.M., "A mathematical analysis for indentation tests of articular cartilage," *J. Biomech. Eng.*, vol. 5, pp. 541-551, 1972.

136 A. R. Karduna, Halperin, H.R., and Yin, F.C.P., "Experimental and numerical analyses of indentation in finite-sized isotropic and anisotropic rubber-like materials," *Ann. Biomed. Eng.*, vol. 25, pp. 1009-1016, 1997.

137 M. F. M. Radmacher, CM Kacher, JP Cleveland and PK Hansma, "Measuring the visco-elastic properties of human platelets with the atomic force microscope," *Biophys. J.*, vol. 70, pp. 556-567, 1996.

138 S. M. J.P. Cleveland, D. Bocek and P.K. Hansma, "A nondestructive method for determining the spring constant of cantilevers for scanning force microscopy," *Rev. Sci. Instrum.*, vol. 64, pp. 403-405, 1993.

139 W. F. Stokey, *Shock and Vibration Handbook (Harris, C.M., Ed.), Ch. 7.* New York: McGraw-Hill, 1996.

140 J. A. D. a. J.-P. Revel, "Examination of atomic (scanning) force microscopy probe tips with the transmission electron microscope," *Microsc. Microanal.*, vol. 3, pp. 203-213, 1997.

141 M. N. S. Grafström, T. Hagen, J. Ackermann, R. Neumann, O. Ptobst and M. Wörtge, "The role of topography and friction for the image contrast in lateral force microscopy," *Nanotechnology*, vol. 4, pp. 143-151, 1993.

142 C. S. a. J. Hoh, "Slow cellular dynamics in MDCK and R5 cells monitored by time-lapse atomic force microscopy," *Biophys. J.*, vol. 67, pp. 929-936, 1994.

143 S. Shroff, Saner, DS, and Lal, R, "Dynamic micromechanical properties of cultured rat atrial myocytes measured by atomic force microscopy," *Am. J. Physiol.*, vol. 269, pp. C286-C292, 1995.

144 A. Weisenhorn, Khorshandi, M. , Kasas, S., Gotozos, V., Celio, M.R., and HJ Butt, "Deformation and height anomaly of soft surfaces studied with the AFM," *Nanotechnology*, vol. 4, pp. 106-113, 1993.

145 S. C. Lieber, N. Aubry, J. Pain, G. Diaz, S. J. Kim, and S. F. Vatner, "Aging Increases Stiffness of Cardiac Myocytes Measured by Atomic Force Microscopy Nanoindentation," *Am J Physiol Heart Circ Physiol*, 2004.

146 R. D. Lipman, C. E. Chrisp, D. G. Hazzard, and R. T. Bronson, "Pathologic characterization of brown Norway, brown Norway x Fischer 344, and Fischer 344 x brown Norway rats with relation to age," *J Gerontol A Biol Sci Med Sci*, vol. 51, pp. B54-9, 1996.

147 S. J. Kim, A. Yatani, D. E. Vatner, S. Yamamoto, Y. Ishikawa, T. E. Wagner, R. P. Shannon, Y. K. Kim, G. Takagi, K. Asai, C. J. Homcy, and S. F. Vatner, "Differential regulation of inotropy and lusitropy in overexpressed Gsalpha myocytes through cAMP and Ca2+ channel pathways," *J Clin Invest*, vol. 103, pp. 1089-97, 1999.

148 J. Kajstura, E. Cigola, A. Malhotra, P. Li, W. Cheng, L. G. Meggs, and P. Anversa, "Angiotensin II induces apoptosis of adult ventricular myocytes in vitro," *J Mol Cell Cardiol*, vol. 29, pp. 859-70, 1997.

149 A. M. Collinsworth, S. Zhang, W. E. Kraus, and G. A. Truskey, "Apparent elastic modulus and hysteresis of skeletal muscle cells throughout differentiation," *Am J Physiol Cell Physiol*, vol. 283, pp. C1219-27, 2002.

150 A. B. Mathur, A. M. Collinsworth, W. M. Reichert, W. E. Kraus, and G. A. Truskey, "Endothelial, cardiac muscle and skeletal muscle exhibit different viscous and elastic properties as determined by atomic force microscopy," *J Biomech*, vol. 34, pp. 1545-53, 2001.

151 T. D. Sato M, Wheeler LT, Ohshima N, Nerem RM, "Application of the micropipette technique to the measurement of cultured porcine aortic endothelial cell viscoelastic properties," *J. Biomech. Eng.*, vol. 112, pp. 263-68, 1990.

152 B. J. Briscoe, Sebastian, K.S., and Adams M.J., "The effect of indenter geometry on the elastic response to indentation," *J. Phys. D: Appl. Phys.*, vol. 27, pp. 1156-1162, 1994.

153 C. a. W. Gerald, P., *Applied Numerical Analysis*, 6 ed. New York: Addison Wesley, 1997.

154 A. M. Gomez, B. Schwaller, H. Porzig, G. Vassort, E. Niggli, and M. Egger, "Increased exchange current but normal Ca2+ transport via Na+-Ca2+ exchange during cardiac hypertrophy after myocardial infarction," *Circ Res*, vol. 91, pp. 323-30, 2002.

155 A. E. Green, and Zerna, W., *Theoretical Elasticity*. London: Oxford University Press, 1968.

156 D. A. Kass and W. L. Maughan, "From 'Emax' to pressure-volume relations: a broader view," *Circulation*, vol. 77, pp. 1203-12, 1988.

157 D. Burkhoff, S. Sugiura, D. T. Yue, and K. Sagawa, "Contractility-dependent curvilinearity of end-systolic pressure-volume relations," *Am J Physiol*, vol. 252, pp. H1218-27, 1987.

158 A. Kono, W. L. Maughan, K. Sunagawa, K. Hamilton, K. Sagawa, and M. L. Weisfeldt, "The use of left ventricular end-ejection pressure and peak pressure in the estimation of the end-systolic pressure-volume relationship," *Circulation*, vol. 70, pp. 1057-65, 1984.

159 D. A. Kass, R. Beyar, E. Lankford, M. Heard, W. L. Maughan, and K. Sagawa, "Influence of contractile state on curvilinearity of in situ end-systolic pressure-volume relations," *Circulation*, vol. 79, pp. 167-78, 1989.

160 G. Olivetti, G. Giordano, D. Corradi, M. Melissari, C. Lagrasta, S. R. Gambert, and P. Anversa, "Gender differences and aging: effects on the human heart," *J Am Coll Cardiol*, vol. 26, pp. 1068-79, 1995.

161 F. C. Yin, H. A. Spurgeon, K. Rakusan, M. L. Weisfeldt, and E. G. Lakatta, "Use of tibial length to quantify cardiac hypertrophy: application in the aging rat," *Am J Physiol*, vol. 243, pp. H941-7, 1982.

162 J. M. Capasso, D. Fitzpatrick, and P. Anversa, "Cellular mechanisms of ventricular failure: myocyte kinetics and geometry with age," *Am J Physiol*, vol. 262, pp. H1770-81, 1992.

163 H. L. Granzier and T. C. Irving, "Passive tension in cardiac muscle: contribution of collagen, titin, microtubules, and intermediate filaments," *Biophys J*, vol. 68, pp. 1027-44, 1995.

164 K. Trombitas, J. P. Jin, and H. Granzier, "The mechanically active domain of titin in cardiac muscle," *Circ Res*, vol. 77, pp. 856-61, 1995.

165 A. J. Brady, "Length dependence of passive stiffness in single cardiac myocytes," *Am J Physiol*, vol. 260, pp. H1062-71, 1991.

166 F. C. P. Yin, H. A. Spurgeon, M. L. Weisfeldt, and E. G. Lakatta, "Mechanical properties of myocardium from hypertrophied rat hearts. A comparison between hypertrophy induced by senescence and by aortic banding.," *Circ. Res.*, vol. 1980, pp. 292-300, 1980.

167 J. Lammerding, R. D. Kamm, and R. T. Lee, "Mechanotransduction in cardiac myocytes," *Ann N Y Acad Sci*, vol. 1015, pp. 53-70, 2004.

168 J. Sadoshima and S. Izumo, "The cellular and molecular response of cardiac myocytes to mechanical stress," *Annu Rev Physiol*, vol. 59, pp. 551-71, 1997.

169 R. Knoll, M. Hoshijima, and K. Chien, "Cardiac mechanotransduction and implications for heart disease," *J Mol Med*, vol. 81, pp. 750-6, 2003.

170 P. H. Sugden, "Ras, Akt, and mechanotransduction in the cardiac myocyte," *Circ Res*, vol. 93, pp. 1179-92, 2003.

171 J. M. Lewis and M. A. Schwartz, "Mapping in vivo associations of cytoplasmic proteins with integrin beta 1 cytoplasmic domain mutants," *Mol Biol Cell*, vol. 6, pp. 151-60, 1995.

172 M. L. Burgess, J. C. McCrea, and H. L. Hedrick, "Age-associated changes in cardiac matrix and integrins," *Mech Ageing Dev*, vol. 122, pp. 1739-56, 2001.

173 P. Wang, A. J. Valentijn, A. P. Gilmore, and C. H. Streuli, "Early events in the anoikis program occur in the absence of caspase activation," *J Biol Chem*, vol. 278, pp. 19917-25, 2003.

174 R. S. Keller, S. Y. Shai, C. J. Babbitt, C. G. Pham, R. J. Solaro, M. L. Valencik, J. C. Loftus, and R. S. Ross, "Disruption of integrin function in the murine myocardium leads to perinatal lethality, fibrosis, and abnormal cardiac performance," *Am J Pathol*, vol. 158, pp. 1079-90, 2001.

175 S. Y. Shai, A. E. Harpf, C. J. Babbitt, M. C. Jordan, M. C. Fishbein, J. Chen, M. Omura, T. A. Leil, K. D. Becker, M. Jiang, D. J. Smith, S. R. Cherry, J. C. Loftus, and R. S. Ross, "Cardiac myocyte-specific excision of the beta1 integrin gene results in myocardial fibrosis and cardiac failure," *Circ Res*, vol. 90, pp. 458-64, 2002.

176 H. Chen, D. M. Cohen, D. M. Choudhury, N. Kioka, and S. W. Craig, "Spatial distribution and functional significance of activated vinculin in living cells," *J Cell Biol*, vol. 169, pp. 459-70, 2005.

177 C. Bakolitsa, D. M. Cohen, L. A. Bankston, A. A. Bobkov, G. W. Cadwell, L. Jennings, D. R. Critchley, S. W. Craig, and R. C. Liddington, "Structural basis for vinculin activation at sites of cell adhesion," *Nature*, vol. 430, pp. 583-6, 2004.

178 C. E. Ganote and R. S. Vander Heide, "Cytoskeletal lesions in anoxic myocardial injury. A conventional and high-voltage electron-microscopic and immunofluorescence study," *Am J Pathol*, vol. 129, pp. 327-44, 1987.

179 R. S. Vander Heide and C. E. Ganote, "Increased myocyte fragility following anoxic injury," *J Mol Cell Cardiol*, vol. 19, pp. 1085-103, 1987.

180 A. E. Zemljic-Harpf, S. Ponrartana, R. T. Avalos, M. C. Jordan, K. P. Roos, N. D. Dalton, V. Q. Phan, E. D. Adamson, and R. S. Ross, "Heterozygous inactivation of the vinculin gene predisposes to stress-induced cardiomyopathy," *Am J Pathol*, vol. 165, pp. 1033-44, 2004.

181 J. Schaper, R. Froede, S. Hein, A. Buck, H. Hashizume, B. Speiser, A. Friedl, and N. Bleese, "Impairment of the myocardial ultrastructure and changes of the cytoskeleton in dilated cardiomyopathy," *Circulation*, vol. 83, pp. 504-14, 1991.

182 W. H. Goldmann, R. Galneder, M. Ludwig, W. Xu, E. D. Adamson, N. Wang, and R. M. Ezzell, "Differences in elasticity of vinculin-deficient F9 cells measured by magnetometry and atomic force microscopy," *Exp Cell Res*, vol. 239, pp. 235-42, 1998.

183 W. H. Goldmann, Galneder, R., Ludwig, M. Kromm, A., and Ezzell, R.M., "Differences in F9 and 5.51 cell elasticity determined by cell poking and atomic force microscopy," *FEBS Lett.*, vol. 424, pp. 139-142, 1998.

184 H. Tsutsui, K. Ishihara, and G. T. Cooper, "Cytoskeletal role in the contractile dysfunction of hypertrophied myocardium," *Science*, vol. 260, pp. 682-7., 1993.

185 H. Tsutsui, H. Tagawa, R. L. Kent, P. L. McCollam, K. Ishihara, M. Nagatsu, and G. T. Cooper, "Role of microtubules in contractile dysfunction of hypertrophied cardiocytes," *Circulation*, vol. 90, pp. 533-55., 1994.

186 H. Tagawa, N. Wang, T. Narishige, D. E. Ingber, M. R. Zile, and G. T. Cooper, "Cytoskeletal mechanics in pressure-overload cardiac hypertrophy," *Circ Res*, vol. 80, pp. 281-9., 1997.

187 B. A. Bailey, K. Dipla, S. Li, and S. R. Houser, "Cellular basis of contractile derangements of hypertrophied feline ventricular myocytes," *J Mol Cell Cardiol*, vol. 29, pp. 1823-35, 1997.

188 P. P. de Tombe, "Altered contractile function in heart failure," *Cardiovasc Res*, vol. 37, pp. 367-80., 1998.

189 X. Wang, F. Li, and A. M. Gerdes, "Chronic pressure overload cardiac hypertrophy and failure in guinea pigs: I. Regional hemodynamics and myocyte remodeling," *J Mol Cell Cardiol*, vol. 31, pp. 307-17, 1999.

190 J. F. Collins, C. Pawloski-Dahm, M. G. Davis, N. Ball, G. W. Dorn, 2nd, and R. A. Walsh, "The role of the cytoskeleton in left ventricular pressure overload hypertrophy and failure," *J Mol Cell Cardiol*, vol. 28, pp. 1435-43., 1996.

191 Z. Li, E. Colucci-Guyon, M. Pincon-Raymond, M. Mericskay, S. Pournin, D. Paulin, and C. Babinet, "Cardiovascular lesions and skeletal myopathy in mice lacking desmin," *Dev Biol*, vol. 175, pp. 362-6, 1996.

192 D. J. Milner, G. Weitzer, D. Tran, A. Bradley, and Y. Capetanaki, "Disruption of muscle architecture and myocardial degeneration in mice lacking desmin," *J Cell Biol*, vol. 134, pp. 1255-70, 1996.

193 L. Thornell, L. Carlsson, Z. Li, M. Mericskay, and D. Paulin, "Null mutation in the desmin gene gives rise to a cardiomyopathy," *J Mol Cell Cardiol*, vol. 29, pp. 2107-24, 1997.

194 J. Balogh, M. Merisckay, Z. Li, D. Paulin, and A. Arner, "Hearts from mice lacking desmin have a myopathy with impaired active force generation and unaltered wall compliance," *Cardiovasc Res*, vol. 53, pp. 439-50, 2002.

195 D. J. Milner, M. Mavroidis, N. Weisleder, and Y. Capetanaki, "Desmin cytoskeleton linked to muscle mitochondrial distribution and respiratory function," *J Cell Biol*, vol. 150, pp. 1283-98, 2000.

196 L. Kay, Z. Li, M. Mericskay, J. Olivares, L. Tranqui, E. Fontaine, T. Tiivel, P. Sikk, T. Kaambre, J. L. Samuel, L. Rappaport, Y. Usson, X. Leverve, D. Paulin, and V. A. Saks, "Study of regulation of mitochondrial respiration in vivo. An analysis of influence of ADP diffusion and possible role of cytoskeleton," *Biochim Biophys Acta*, vol. 1322, pp. 41-59, 1997.

197 Y. Cui, Y. T. Shen, B. Kalthof, M. Iwase, N. Sato, M. Uechi, S. F. Vatner, and D. E. Vatner, "Identification and functional role of beta-adrenergic receptor subtypes in primate and rodent: in vivo versus isolated myocytes," *J Mol Cell Cardiol*, vol. 28, pp. 1307-17, 1996.

198 K. Uemura, T. Kawada, M. Sugimachi, C. Zheng, K. Kashihara, T. Sato, and K. Sunagawa, "A self-calibrating telemetry system for measurement of ventricular pressure-volume relations in conscious, freely moving rats," *Am J Physiol Heart Circ Physiol*, vol. 287, pp. H2906-13, 2004.

199 DI, *MultiMode™ SPM Support Note 290-B FluidOperation.* Santa Barbara, CA: Veeco Metrology Group, 1997.